5-2019

A stochastic continuum damage model for dynamic fracture analysis of quasi-brittle materials using asynchronous Spacetime Discontinuous Galerkin (aSDG) method

Bahador Bahmani
University of Tennessee, bbahmani@vols.utk.edu

To the Graduate Council:

I am submitting herewith a thesis written by Bahador Bahmani entitled "A stochastic continuum damage model for dynamic fracture analysis of quasi-brittle materials using asynchronous Spacetime Discontinuous Galerkin (aSDG) method." I have examined the final electronic copy of this thesis for form and content and recommend that it be accepted in partial fulfillment of the requirements for the degree of Master of Science, with a major in Mechanical Engineering.

Reza Abedi, Major Professor

We have read this thesis and recommend its acceptance:

Stephanie TerMaath, Timothy Truster

Accepted for the Council:
Dixie L. Thompson

Vice Provost and Dean of the Graduate School

(Original signatures are on file with official student records.)

A stochastic continuum damage model for dynamic fracture analysis of quasi-brittle materials using asynchronous Spacetime Discontinuous Galerkin (aSDG) method

A Thesis Presented for the

Master of Science

Degree

The University of Tennessee, Knoxville

Bahador Bahmani

May 2019

Dedicated with a great affection to my spouse and family.

Acknowledgments

First, I express sincere thanks to my adviser Dr. Reza Abedi for his support during my study. I would like to thank my MS thesis committee members Drs. Stephanie TerMaath, Timothy Truster, and Katherine Acton. I gratefully acknowledge supports for my research via the U.S. National Science Foundation (NSF), CMMI - Mechanics of Materials and Structures (MoMS) program grant number 1538332.

Abstract

The microstructural design has an essential effect on the fracture response of brittle materials. We present a stochastic bulk damage formulation to model dynamic brittle fracture. This model is compared with a similar interfacial model for homogeneous and heterogeneous materials. The damage models are rate-dependent, and the corresponding damage evolution includes delay effects. The evolution equation specifies the rate at which damage tends to its quasi-static limit. The relaxation time of the model introduces an intrinsic length scale for dynamic fracture and addresses the mesh sensitivity problem of earlier damage models with much less computational efforts. The ordinary differential form of the damage equation makes this remedy quite simple and enables capturing the loading rate sensitivity of strain-stress response. A stochastic field is defined for material cohesion and fracture strength to involve microstructure effects in the proposed formulations. The statistical fields are constructed through the Karhunen-Loeve (KL) method.

An advanced asynchronous Spacetime Discontinuous Galerkin (aSDG) method is used to discretize the final system of coupled equations. Local and asynchronous solution process, linear complexity of the solution versus the number of elements, local recovery of balance properties, and high spatial and temporal orders of accuracy are some of the main advantages of the aSDG method.

Several numerical examples are presented to demonstrate mesh insensitivity of the method and the effect of boundary conditions on dynamic fracture patterns. It is shown that inhomogeneity greatly differentiates fracture patterns from those of a homogeneous rock, including the location of zones with maximum damage. Moreover, as the correlation length of the random field decreases, fracture patterns resemble angled-cracks observed in

compressive rock fracture. The final results show that a stochastic bulk damage model produces more realistic results in comparison with a homogenizes model.

Table of Contents

List of Tables

List of Figures

Chapter 1

Introduction

1.1 Research plan

Brittle materials have a significant role in the various application: glasses, ceramics, concrete, bone, *etc.* These materials are susceptible to sudden rupture by cracking as they have many micro-defects and micro-cracks. One of the challenging problems in understanding the behavior of brittle materials is predicting the crack path and failure response. The fracture response of brittle materials are very sensitive to geometry, brittleness, loading, and microstructure. The lack of resources to address effect of impact loads on brittle materials with consideration of underlying microstructure conducts us to develop a numerical toolbox for investigating these effects on failure patterns. The proposed numerical toolbox can be used in various application from design to analysis of brittle materials in high impact loading conditions, for example in ceramic industry. Finding the relation between microstructure randomness and failure patterns helps the efficient design of many engineered composites. For example in a concrete dam, it is crucial to predict and prevent progressive failures such as cracks initiation and propagation under impact loads, *e.g.,* earthquake vibration. Therefore, the primary concern of the following proposal is formulating a microstructure-based damage model which incorporates all dynamical effects of brittle material fracture response. The proposed research consist of:

- **Formulating a hyperbolic continuum damage model**: The continuum damage models are very appropriate for modeling complex fracture patterns of brittle materials as they reduce difficulties in the numerical representation of moving discontinuous interfaces. In standard damage models, the effect of crack activation with a time delay in dynamic loads is not included. The author utilizes Allix's damage model [19] in a novel Spacetime Discontinuous Galerkin formulation and modifies this damage model for brittle material. The final system of damage-solid equations remains hyperbolic which preserves the nonlocality of softening behavior in brittle materials. This task is already done, and the corresponding results are published in [20].

- **Up-scaling microstructure randomness to a macroscopic continuum model**: Two conventional methods for linking microstructure to macroscale analysis are numerical homogenization (NH) and computational homogenization (CH) methods. CH methods construct backward/forward relations between microscale and macroscale, but in NH methods the information just transfers from micro-level to macro-level. The numerical difficulties and simulation time of CH methods do not permit their application to realistic problems. On the other hand, in NH methods the RVE limit and periodicity conditions restrict the application for modeling random materials. Therefore, we constructs a basis to characterize the randomness through statistical volume element (SVE) instead of RVE for generating realizations of the stochastic partial differential equation. This task is partly done, and a novel homogenization approach for material property characterization is developed by Voronoi tessellation and square SVEs [14, 24]. The ongoing part is linking mesoscale informed properties with the statistical damage model.

1.2 Intellectual merits

Four aspects of the proposed research are: (1) novel use of statistical representative volume elements to systematically propagate material randomness through the entire analysis length scales; (2) use of two distinct grids for FEM solution and material properties to accurately

render random fields (3) formulate and compare continuum and sharp fracture models to track complex fracture patterns using advanced mesh adaptive operations.

1.3 Broader Impacts

Brittle materials are increasingly used in hybrid high-strength, lightweight material designs. Some fracture/contact-related applications are in rock fracture (earthquake, hydraulic fracturing, geothermal energy, and CO2 sequestration), armor design, and in bone fracture. Finally, the statistical concepts (SVE and distinct domain grids) and adaptive FEM formulations can apply to other random media and sharp moving interface problems. For example, in some applications of chemically activated fracture, the chemical reaction equation is similar to the damage evolution equation.

1.4 Background

1.4.1 Effect of microstructure on quasi-brittle fracture

1.4.1.1 The effect of spatial inhomogeneity on fracture response

All materials, even if considered macroscopically homogeneous, are in essence heterogeneous (below certain scales) due to their hierarchical design. One of the most common assumption in numerical or analytical models is the homogeneity of material properties. In linear analysis, the homogenous assumption predicts overall responses well although this assumption is not realistic. In failure analyses, for example fracture of brittle materials, the homogeneous assumption tends to predict unrealistic results. For instance, consider a pressurized ring shown in Fig. 1.1 where the uniform internal pressure is gradually increased to the ultimate load capacity of the ring. There are two scenarios: 1) assuming homogeneous material properties leads to a sudden rupture at every point in the domain which is obviously unrealistic; 2) existing some inhomogeneities in material properties which ensures there are some (not infinite) weaker point that fail first. Therefore, the spatial inhomogeneities have

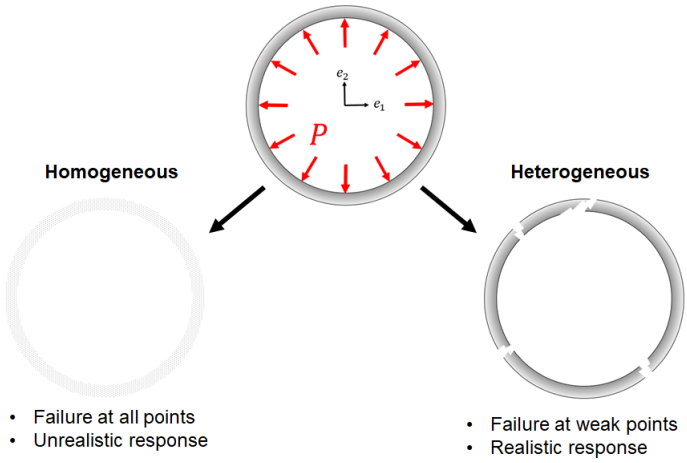

Figure 1.1: Effect of spatial inhomogeneities on failure response

.

significant effects on initiation and propagation of fractures. In addition, considering these effects in numerical analysis is crucial to predict realistic responses.

As shown by many experimental and numerical investigations, in brittle materials fracture path can be varied by changing the material properties. One important contribution is the experimental work done by Al-Ostaz and Jasiuk [15] where they tested several Epoxy sheets with holes where all of them had similar geometry and loading configurations. The only difference between the samples came from random properties of their microstructure. In Fig. 1.2, the remarkable fracture pattern variations between samples are reported. While most cracks follow a critical path, there are some variations due to the randomness at microscale.

Total energy dissipation, as another important macroscopic property of a system, can be affected by microstructural randomness. However, as it is shown in Fig. 1.3, this effect is more significant for brittle materials during the nonlinear post-ultimate (softening regime) of load response. Also, it is vital to indicate that there is no mechanism for brittle materials to dissipate energy by undergoing plastic deformation. Instead, they dissipate energy by instant initiation and propagating fracture surfaces around defects and microcracks where the stress intensities are much higher. Therefore, material randomness has significant influence on crack initiation and propagation zones, which in turn affect the energy dissipation path of brittle materials.

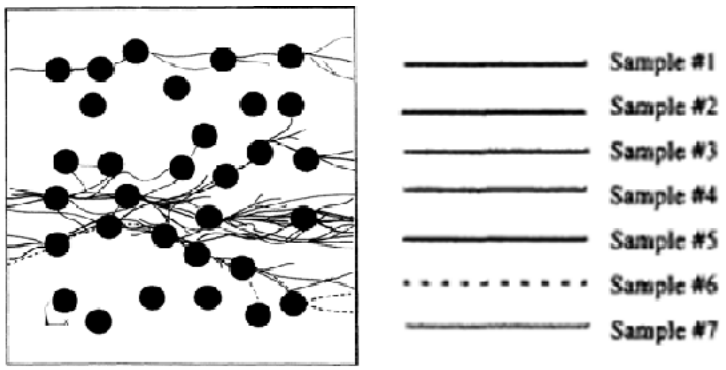

Figure 1.2: Effect of random material properties on crack patterns for different samples of Epoxy sheets with same configuration of holes and loadings [15]

.

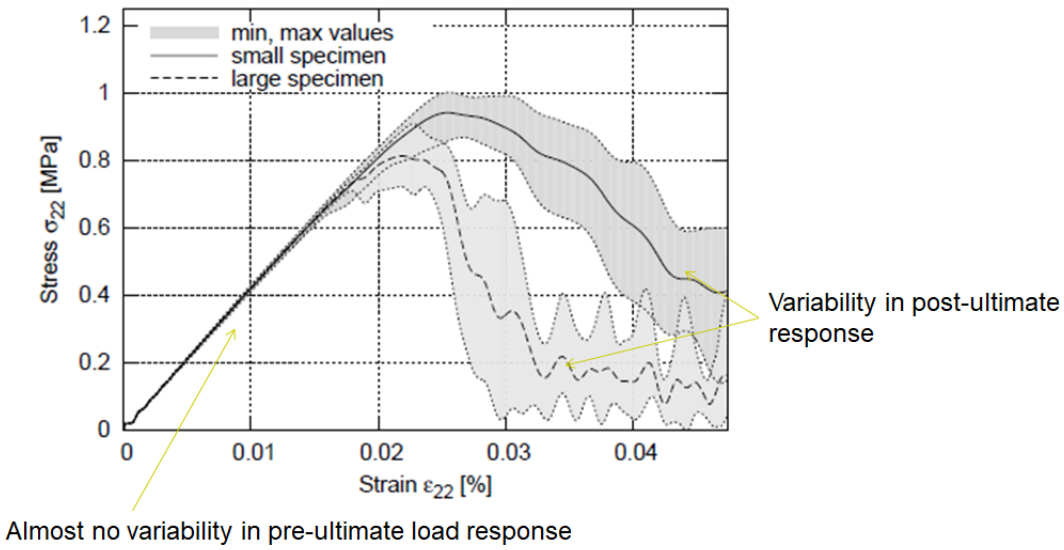

Figure 1.3: Microstructure effect on fracture toughness randomness and post-ultimate load response [72].

1.4.2 Computational and theoretical models for modeling fracture

There are two main categories to model fracture: : *Sharp interface* and *bulk/continuum* fracture models. In sharp interface methods fracturing process is considered as a localized zone where the specific physical changes happen in an area with one dimension lower than the actual domain. On the other hand, in bulk/continuum models the degradation (softening) process is modeled in the bulk domain, rather than on interfaces.

1.4.2.1 Sharp interface fracture models

In this approach the existence of fracture is distinguished by geometrically defined fractures in the domain on localized regions. The fracture geometry is explicitly recovered as a discontinuity in the response field. In addition, special singularities (crack tips) or nonlinearities (crack tip process zones) can be defined on fracture geometry through three well-known models: *Linear elastic fracture mechanics* (LEFM), *traction-separation relation* (TSR), and *interfacial damage*. LEFM introduces special singularities near the crack tip which is often unrealistic. The unrealistic singular stress can be resolved by TSRs. In reality the high values of stress near the crack tip produce a zone near the tip where the material experiences some plastic process to re-balance the proposed stress values with material strength limit. For quasi-brittle materials, where the zone of nonlinear material response around the crack tip is small, the process zone can be mapped to the fracture surface near the tip called *fracture process zone* (FPZ). The TSR with cohesive models limit stress values within the FPZ. In addition, all the nonlinear softening process act on FPZ through TSR models. Therefore, TSR models are more realistic than LEFM. It is noteworthy to indicate that in most TSRs the surface of fracture process zone (FPZ) is known as an input parameter for the model which is not a correct assumption. Also, they have several difficulties to capture transition from bonding to debonding phases of fracturing process in loading-unloading cases. *Interfacial damage* models are good candidates for solving the previous problems. In these models, there is a damage parameter which has a value between zero (fully bonding) to unity (fully debonding or free surface crack) over the whole crack surface.The connection between

damage phase and mechanical phase is established through some interfacial constitutive laws (like TSR) to account for energy part of degradation.

Four commonly-employed crack tracking strategies in finite element methods are illustrated in Fig. 1.4. In the most simple one, mesh is fixed and non-conformal to the fracture surface (Fig. 1.4(a)). In the fixed method the true fracture surface (red line) is roughly approximated by closest element edges (green) to it. Clearly, handling of mixed mode loadings, where the crack path is not predictable, is challenging and the dynamics of the moving cracks predicted are not reliable. Adaptive meshing scheme, as illustrated in Fig. 1.4(b), is another approach for modeling crack patterns. In this approach element boundaries are aligned with predicted crack paths [13]. In fixed and adaptive methods, discontinuous features are defined by splitting the internal domain with explicit boundaries (approximated fracture surfaces). On the other hand, discontinuous features are incorporated into approximation field by enhancing basis functions with some special functions through *eXtended finite element method* (X-FEM). In this method, there are some zones around fractures (surrounded area with blue lines in Fig. 1.4(c)) called enriched zones where element basis functions are enriched.

Simulating crack growth using the classical FEM is quite difficult because the topology of the domain changes continuously. On the other hand, allowing to simulate arbitrary discontinuity with a fixed mesh, the X-FEM method, follows a crack path within the elements. In particular the domain does not have to be re-meshed as crack propagates. Although the X-FEM alleviates the problem of modeling arbitrary cracks and discontinuities of the finite element mesh, the modeling of more complex fracture topologies such as

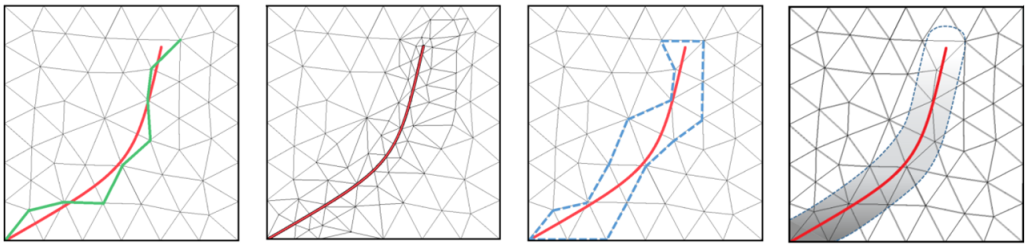

Figure 1.4: Discretization schemes for tracking cracks in the Finite Element Method [13].

microcracking and bifurcation demand the derivation and inclusion of additional enrichment functions [13].

1.4.2.2 Bulk/continuum fracture models

These approaches model fractures using a continuum set-up based on damage mechanics. Bulk models drastically reduce computational cost and programming challenges related to previous models, specifically in the case of mesh adaptive methods and XFEMs. The idea of damage mechanics comes from a simple reduction of defect surfaces from whole area of the *representative volume element* (RVE). As a result, there is a reduction in material load capacity by introducing the softening behavior in material constitute law. For instance, in one dimensional set-up the Young's modulus E is effectively reduced by the factor $(1 - D)$,

$$\sigma = (1 - D)E\epsilon, \tag{1.1}$$

where $0 \leq D < 1$ is a non decreasing function of strain. The computation of damage value itself is very crucial and it classifies the damage theory into two major classes: Local and non-local theories. In the classical (local) theories a nonlinear explicit relation is defined for damage variable which is based on the state variables of the problem (strain, stress, damage itself, temperature and so on). Generally, many of constitutive equations for damage value are empirical and calibrated through experiments. There are some crucial problems with local models, especially in modeling brittle fractures where the width of damage area is extremely narrow. In numerical setting, the results will be mesh-dependent and mathematically the governing equation for a localized form will be ill-posed when the localize band tends to zero (fracture width). This problem can be resolved in different ways through considering a non-local zone for damage effect which leads to another class of damage mechanics called non-local models.

The first idea of using bulk/continuum models for fracture modeling was proposed by Bažant and Lin [30], as the smeared crack approach. In continuum damage models, the fracture cannot be represented explicitly by free traction surfaces. Instead, the fracture is

defined with a narrow band of material degradation in the bulk domain, illustrated in Fig. 1.4(d) with a dark region around the crack.

In the smeared crack method, material nonlinearities from creation of defects and cracks can be modeled through a generalized bulk constitutive model that represents the process of material degradation through the nucleation and growth of microscale cracks. In fact, the smeared crack method is a link between continuum damage mechanics and TSRs. The smeared crack approach is an innovative idea in progressing new methods based on continuum damage mechanics. One of the most important drawbacks of these methods is the overestimation of the localization (fracture) band with wide width instead of representing a sharp interface for fracture. This is the main reason for developing more advanced models, such as the phase field model proposed by Miehe *et al.* [84]. In phase field approaches, although a continuum damage is introduced, but we still can restrict the damage response over a localized zone.

Firstly, numerical investigations demonstrate heavy mesh dependency of results obtained by local damage models. Specifically, the damage evolution is affected by mesh size. For better clarification of this effect, consider a simple tension test of a plane stress plate with a hole at its center; *cf.* Fig. 1.5. It is expected that the results converge to the accurate response by refining the numerical mesh. However, it is shown in Fig. 1.5 that the results do not converge and there is a high sensitivity against the mesh size.

Later, it was proved that the main reason of such mesh dependency is not due to numerical methods but it has a physical and mathematical origin. From a physical perspective, a damage model should incorporate a material *length scale* to define a reasonable zone for the energy dissipation process. In another word, numerically the damage model at failure point should be integrated with surrounding domain with a non-local radius. To resolve these issues, several nonlocal damage models are proposed. There are two categories of non-local theories: *Integration-based* and *gradient-based*. In the integration models the damage used in (1.1) is an averaged value over a region with a specified size. However in the gradient models, the variation of the damage value is defined to be zero over such a region with specific size as well. Phase field models are the most recent models which are very close to gradient-based models. However, they establish a link between non-locality zone and fracture interface

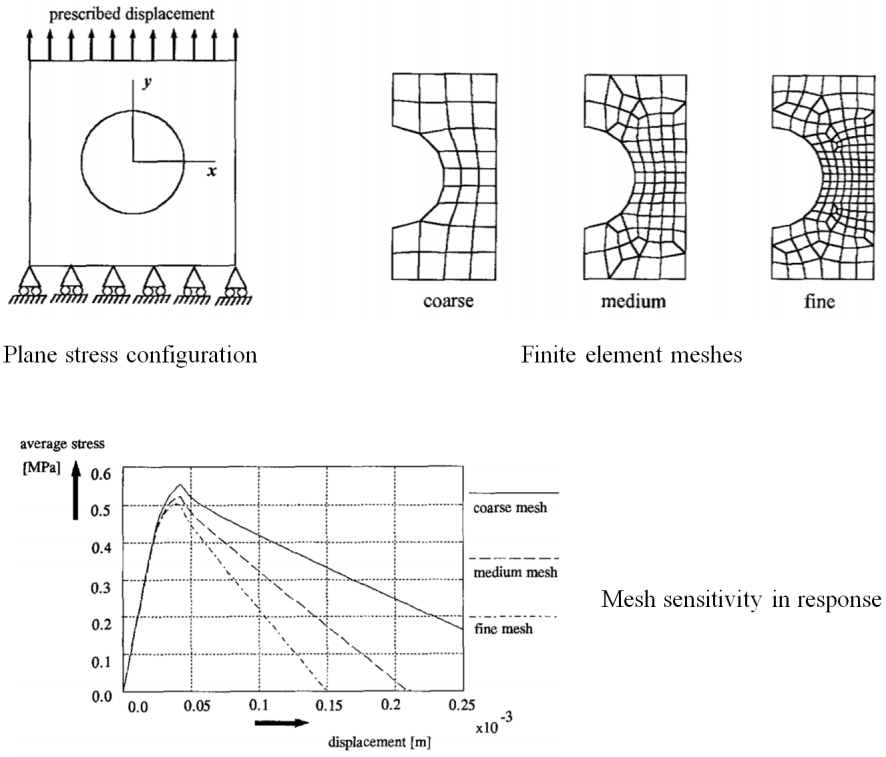

Figure 1.5: Mesh dependency of local damage models [36].

sharpness through a length scale parameter which is more suitable in fracture modeling. The effect of length scale value in phase filed models is shown in Fig. 1.6. It is important to indicate that although decreasing the length scale leads to more realistic representation of fracture interface, in the limit of the length scale tending to zero, the problem becomes ill-posed. Particle methods such as *Peridynamics* [105, 57, 98] are other types of non-local models which have been successfully used to model highly complex fracture patterns that are encountered in dynamic (rock) fracture. They model continua as a collection of interacting particles within a non-local radius.

1.4.2.3 Transient aspect of continuum models

Brittle materials (like concrete) are highly rate-dependent. Experimental investigations show both of the strength and fracture energy increase for higher loading rate. These effects are directly related to changes of the fracture (damage) process with rate, as depicted in Fig. 1.7;

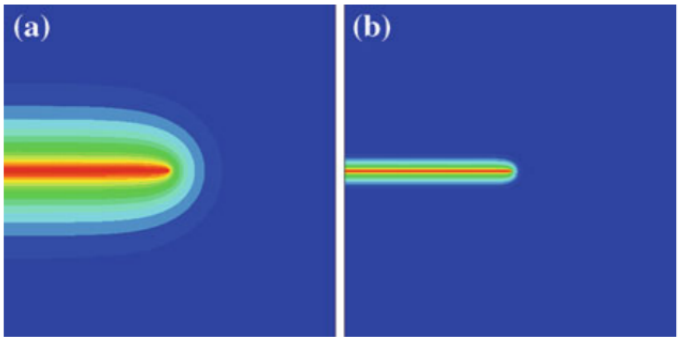

Figure 1.6: Phase field representation of a sharp fracture with different vales of length scales:(a) 0.1; (b) 0.007 [84].

under quasi-static tensile loading conditions the material undergoes three distinctive crack-deformation stages up to complete failure. In quasi-static loading, the material response starts as elastic or visco-elastic deformation with uniform distribution of stresses/strains across the specimen. During this stage (shown as the point a in the static branch of Fig. 1.7) stresses concentrate around multiple micro-cracks and other defects in the material. With increasing deformation, just before and immediately after the peak stress, (b) micro-cracks start to develop and coalesce degrading the material stiffness and strength *i.e.,* damaging the material irreversibly. In a later stage (c), while single macro-cracks start to appear leading to complete material failure, the surrounding material relaxes. Considering the low deformation rates in static loadings, inertial forces can be neglected and the crack opening and material relaxation can be considered as instantaneous processes [95]..

The main difference between the responses of the material under quasi-static and dynamic loading is *time*. In the dynamic situation, the supplied energy crosses through the structure at a certain velocity and damage is no longer instantaneous due to inertia [95]. At high deformation rates crack initiation is retarded (d and e in Fig. 1.7) [95, 103] and stress concentration is reduced at the crack tip due to inertia contribution in the dynamic equilibrium (micro inertia effects)[95, 33]. Inertia also contributes to the observed limited crack propagation velocity. In any case, from a macroscopic point of view, this dynamically induced retarded crack opening process is seen as a resistance to straining and to damage evolution. Additionally, with increasing loading rates, more micro-cracks are activated at the same time and the distribution of micro (and macro) cracks across the fracture process zone

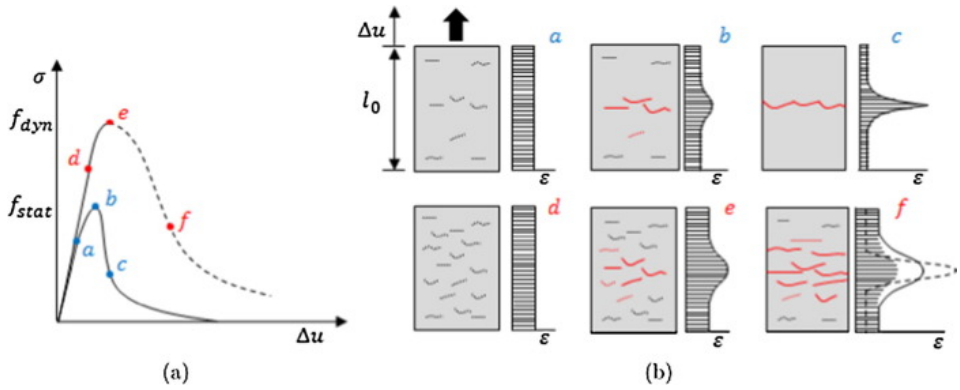

Figure 1.7: Behavior of concrete when loaded under tension at low and high loading rates: (a) Stress-displacement curves ; and (b) crack evolution [95].

(FPZ) changes. Thus, the effective fracture surface and consequently the fracture energy also changes with rate. Therefore, the importance of incorporating the dynamic effects in damage models is obvious, especially, for dynamic brittle fracture modeling.

1.4.2.4 Dynamic continuum damage

In most of the previous studies, the damage formulation for static and dynamic investigations has the same characteristic, and the only difference is the value of strain rates. In these formulations, the strain rate has a contribution in the damage source term. For example, in a strain-based damage formulation the non-local gradient damage equation is [56]

$$\bar{\epsilon} - \frac{l_s^2}{2} \nabla^2 \bar{\epsilon} = \epsilon_{eq}(\epsilon, t), \tag{1.2}$$

where $\bar{\epsilon}$ is a nonlocal strain, l_s is a length scale parameter which introduces a nonlocal radius (damage diffusivity factor) and ϵ_{eq} is an equivalent measurement of local strain which incorporates rate effect. There are various functions to link a nonlocal strain value (as a damage source) to a damage value. Those functions only affect the constitutive laws of damage-deformation mechanism, and cannot change characteristic behaviors of the equation. There is no characteristic wave in the PDE to control the speed of failure propagation. This violation of causality exits even in more sophisticated higher order gradient-based damage

formulation. For instance, in a fourth order nonlocal damage equation [114],

$$\bar{\epsilon} - \frac{l_s^2}{2}\,\nabla^2\bar{\epsilon} + \frac{l_s^4}{8}\,\nabla^4\bar{\epsilon} = \epsilon_{eq}, \tag{1.3}$$

there still is no wave speed implied by the equation. It is common to use similar models for dynamic problems even in phase field methods as the field equation is [86],

$$\frac{g_c}{l_s}\,(d - l_s^2\nabla^2 d) = 2(1-d)H(\epsilon, t), \tag{1.4}$$

Where g_c is the critical energy release rate, d is the damage (crack) phase field variable, and H is a history-dependent function of strain. In these new models, there is a better interpretation of damage phenomenon where they establish a relation between geometry (sharpness of fracture) and damage value through a modified definition of length scale parameter. The effect of length scale value in phase filed models is shown in Fig. 1.6. It is noteworthy to indicate that although decreasing the length scale leads to a more realistic representation of fracture interface, in the limit of the length scale tending to zero, the problem becomes ill-posed.

One of the primary effects on the damage response for dynamic problems is changing fracture energy and failure capacity values with loading rates, as shown in Fig. 1.8. This phenomenon can be considered in previous models by modifying the damage source function. However, the main feature of a dynamic problem, the delay effect of damage propagation, cannot be captured through those models, as the wave speed of information is infinite. The importance of this delay effect is shown by Allix *et al.* [19] through a simple ordinary differential equation (ODE) formulation of damage mechanism for interfacial damage models,

$$\dot{d} = \frac{1}{\tau_c}\,\Big\{1 - H(\epsilon, d)\Big\}, \tag{1.5}$$

where τ_c is a time scale parameter to ensure that the damage evolution is not instantaneous. They also have shown that this time scale has a meaning similar to length scale to recover a non-local response without any mesh dependency problems. A physical justification is performed by Hüssler-Combe and Kühn [59] with introducing a damper effect in damage

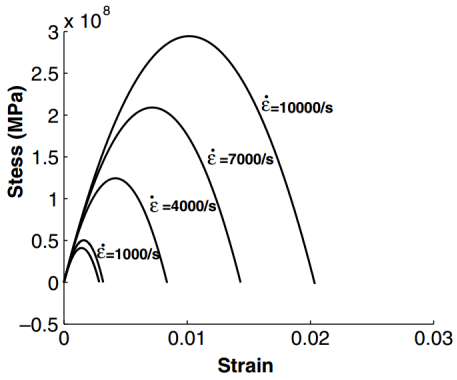

Figure 1.8: The stress-strain curves for loading at various strain rates[19].

mechanism. They modified nonlocal gradient damage models (1.2) by adding the inertia effect,

$$m_\epsilon \ddot{\bar{\epsilon}} + \bar{\epsilon} - \frac{l_s^2}{2} \nabla^2 \bar{\epsilon} = \epsilon_{eq}, \tag{1.6}$$

where m_ϵ is a mass-like parameter. This accommodates for the fact that microcracking and thus damage does not arise arbitrarily fast. A model for this behavior is given in Fig. 1.9 with a simple string-damper model. This model has a row of springs in parallel, whereby each spring has a breaking point with stochastically varying strength. This model basically yields the typical uniaxial stress strain behavior with limited strength and subsequent softening. The basic model is extended with inertial masses in the breaking point which sustain forces over a short time period even in case of breaking. Thus, an overall retardation of damage may arise depending on load distribution and load history [59].

The previous inherently dynamic damage models are more suitable for diffusive fracture response. On the other hand, phase field models have the less diffusive characteristic, so they represent sharpness of fracture interfaces more realistically. Recently, a genuinely dynamic damage model is formulated using the phase-field approach [68].

1.5 Outline and Output

Figure 1.10 shows the outline of the present thesis and general features of our in-house software for the dynamic fragmentation analysis of brittle material. The author's contributions are included in *Macroscopic Fracture Modeling* and *Mesoscale Material*

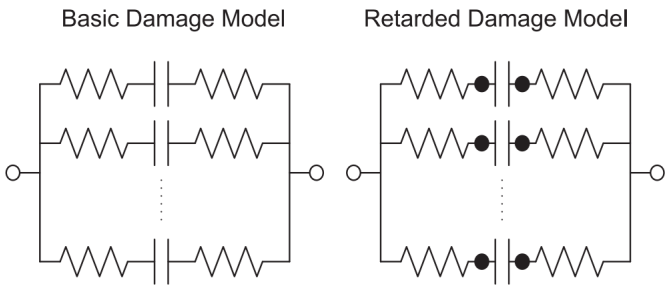

Figure 1.9: Rehelogical models for damage in [59].

Property Characterization modules. The author has formulated the continuum damage model in the context of aSDG method and implemented it into Dr. Abedi's group software written by C++. This formulation and verification aspects are provided in §2 which is completely based on a published paper [20]. In §3, the author will extend the standard formulation to a statistical continuum damage formulation based on the Mohr-Coulomb criterion which incorporates randomness effect into material cohesion. This chapter brings all the materials published in [21]. The author will compare continuum and interfacial damage formulations in §4 where its entire content is borrowed from [22]. The author has been involved in other topics related to *Mesoscale Material Property Characterization* which are not presented in this MS thesis, and interested readers can refer to [14, 24].

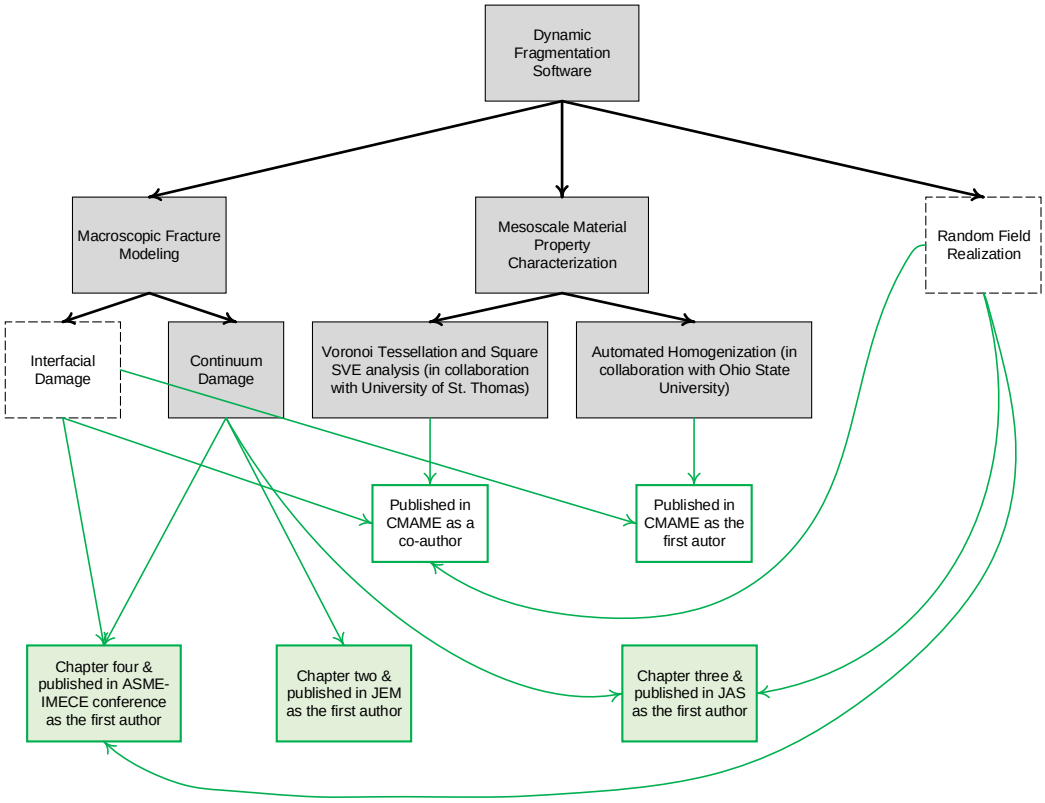

Figure 1.10: Outline of the thesis and major outputs of the author's research.

Chapter 2

Asynchronous Spacetime Discontinuous Galerkin Formulation for a Hyperbolic Time-Delay Bulk Damage Model

This chapter is revised based on the following accepted paper:

B. Bahmani, R. Abedi, "Asynchronous Spacetime Discontinuous Galerkin formulation for a hyperbolic time-delay bulk damage model", Journal of Engineering Mechanics, 2019.

My primary contributions can be listed as (i) formulation of continuum damage model based on the aSDG method, (ii) development of our in-house software by adding damage field and integration of damage phase with elastodynamics phase, (iii) arrangement and interpretation of numerical examples, and (iv) preparation of the first paper draft.

2.1 Abstract

A bulk damage formulation is presented for failure analysis of brittle materials under dynamic loading. A time-delay ordinary differential equation (ODE) is used to model damage evolution. The evolution is driven by the difference between a target static damage value and the instantaneous damage value. A damage length scale is introduced from the model's intrinsic relaxation time and elastic wave speeds. This length scale addresses the mesh sensitivity problem of some existing damage formulations for dynamic fracture, with less computational effort than some other existing remedies. The authors use the asynchronous spacetime discontinuous Galerkin (aSDG) method for the solution of the resulting hyperbolic system of equations. Local and asynchronous solution process, linear complexity of the solution versus the number of elements, local recovery of balance properties, and high spatial and temporal orders of accuracy are some of the main advantages of the aSDG method. Several numerical examples are presented to demonstrate mesh insensitivity of the method and the effect of boundary conditions on dynamic fracture patterns.

2.2 Introduction

Continuum or bulk damage models represent and average the processes of crack nucleation, growth, and coalescence or other types of failure evolution at microscale. This point of

view was introduced by Bažant [30] in the context of smeared crack model for concrete. In contrast, *sharp interface* models directly represent crack surfaces without *averaging* their effect into a bulk damage field. From a computational point of view and in *finite element methods* (FEMs), cracks can be inserted on inter-element boundaries, *e.g.,* [37], or propagate inside elements as in *eXtended* [32, 85] and *generalized* [50, 109] FEMs.

The main advantage of bulk damage models is the implicit representation of cracks. Hence, complex features such as microcracking and crack branching are automatically captured as a part of the solution; in contrast, in all aforementioned sharp interface FEMs, accommodating such complex fracture patterns poses serious challenges either on finite element geometric meshing or on formulating the enriched basis functions; see for example [45]. However, continuum models can suffer from mesh-dependency and diffusive response [106, 83]. The mesh dependency of the original damage models originates from the localization phenomenon and loss of ellipticity / hyperbolicity of the formulated (initial) boundary value problem [73, 79]. There are three approaches to address mesh-dependency: gradient-based, integration-based, and time-relaxed or viscous non-local models [47, 94, 65].

In gradient-based models, higher spatial gradients of the damage field are added to the damage governing equation [92, 42]. The addition of such higher order terms introduces intrinsic length scales to the model. In integration-based models, the damage variable at each point is a weighted average of damage value inside a neighborhood defined by a length scale parameter [94, 95]. The intrinsic length scale of either of these models prevents the width of the localization region to go to zero in the limit of mesh refinement, thus it addresses the mesh sensitivity problem. Time-relaxed or viscous damage models are either nonlocal in time, *i.e.,* involving a temporal convolution, or more simply are represented by an *ordinary differential equation* (ODE) in time [18, 80, 60, 67].

In this manuscript, we present a time-delay damage formulation similar to the model in [19, 111]. Herein, a static damage model is relaxed by the addition of the damage temporal rate multiplied by a relaxation time τ_c. For dynamic problems, the interaction of the relaxation time with the elastodynamic wave speeds indirectly introduces intrinsic length scale(s) that similar to the aforementioned space-based formulations remedies the mesh sensitivity problem.

The majority of damage formulations are implemented by *continuous finite element methods* (CFEMs). Moreover, most are limited to quasi-static analysis. *Discontinuous Galerkin* (DG) methods are excellent alternatives to CFEMs for the solution of hyperbolic PDEs. First, their solution space better approximates a variety of discontinuous solution features encountered in the solution of hyperbolic PDEs. Second, when explicitly integrated in time, the solution is local with linear complexity in terms of the number of elements. To accommodate this with CFEMs, mass lumping is required which can negatively impact the order of accuracy. Finally, DG methods are much more flexible for h and hp adaptive operations and better lend themselves to parallel computing [61].

The literature on DG formulation of damage models is very limited. For interfacial models, [115] uses a DG formulation to model fracture on bi-material interphases. The authors have formulated a sharp interfacial model using Riemann solutions for dynamic fracture [6] and contact/fracture [5] problems. As for the bulk models, [120] has developed a low-order DG method for the application of strain-gradient damage models to quasi-static conditions. In addition, [39] presents a DG formulation for a phase-field model that closely resembles gradient-based damage models. While this formulation is for elastodynamics, the PDE of this phase-field model is parabolic. This implies that damage can propagate with infinite speed, an issue that is discredited by physical grounds in [59]. The authors also presented a damage model for rock fracture in [23] where damage evolution was stress-driven and was restricted to shear-dominant fracture under ambient compressive stress. The strain-based damage evolution model presented herein is more appropriate for tensile and mixed-mode fracture problems.

The DG bulk damage formulation presented herein addresses several of the aforementioned issues for modeling dynamic fracture. First, it is a dynamic formulation by being coupled to the elastodynamic equations. Second, the damage evolution maintains the hyperbolicity of the elastodynamic problem and does not violate causality. This lends itself to the *asynchronous spacetime Discontinuous Galerkin* (aSDG) method [7] used herein, as it exploits the causality constraint to provide a highly efficient solution scheme for elastodynamic problem. Third, the ODE form of the governing equation eliminates the need for additional boundary conditions for the damage field and greatly simplifies the

implementation of the method. Fourth, in our prior interfacial damage formulation [6, 5], highly advanced mesh adaptive operations had to be used to exactly track crack paths and capture complex patterns such as microcracking and crack branching; this bulk damage formulation greatly simplifies the problem in the expense of only implicitly representing the effect of microcracks and other features below a certain length scale. Finally, the aSDG method has several very unique advantages over CFEMs and even other DG methods for the solution of hyperbolic problems; please see [7, 10] for a detailed discussion of these advantages.

2.3 Governing equations

In this section, we present separate governing equations for elastodynamics and damage problems. The authors employ a strain-based damage formulation wherein damage evolution follows a time-delay rate model. This damage model is appropriate for brittle materials such as concrete and rock where failure is often tensile dominated and infinitesimal deformation approximation is acceptable.

2.3.1 Rate-dependent and retarded damage formulation

The authors adopt the time-delay model proposed in [18, 19] for damage evolution. Albeit its simplicity, it can incorporate several essential characteristics such as rate-dependency and the delay in damage evolution. In most materials fracture strength and energy are highly rate-dependent, particularly higher strength and energy are observed at higher loading rates. Many existing nonlocal damage models involve parabolic equations or elliptic constraints that imply an infinite speed of wave. In contrast, the evolution equation in [19] preserves the hyperbolicity of the problem.

The *elastic strain energy density*, $\phi(\boldsymbol{\epsilon})$, is defined as,

$$\phi(\boldsymbol{\epsilon}) = \sqrt{\frac{1}{2}\boldsymbol{\epsilon} : \mathbf{C} : \boldsymbol{\epsilon}}, \tag{2.1}$$

where $\mathbf{C}$ is the forth order elasticity tensor and $\boldsymbol{\epsilon}$ is the infinitesimal strain tensor field defined as the symmetric part of the displacement gradient, $\nabla^{\mathrm{s}}\mathbf{u}$. For the remainder of the manuscript only isotropic materials are considered for which $\mathbf{C}$ is uniquely defined by Lamé parameters or the pair of elastic modulus E and Poisson ratio ν.

The authors assume that the bulk damage parameter $\kappa \in [0\ 1]$ be driven by elastic strain energy density, but only through the positive part of strain tensor, $\langle\boldsymbol{\epsilon}\rangle_+$, to ensure that no damage accumulates under pure compressive stress condition. This assumption is originally proposed by Mazars [82] for quasi-brittle materials as the damage is mainly driven by tension in these materials such as rock [66, 92, 87]. Herein, $\langle.\rangle_+$ is the Macaulay positive operator and its value for a symmetric second order tensor $\mathbf{A}$ is,

$$\langle\mathbf{A}\rangle_+ = \sum_{i=1}^{d}\langle a_i\rangle_+ \boldsymbol{\xi}_i \otimes \boldsymbol{\xi}_i, \tag{2.2}$$

where $\boldsymbol{\xi}_i$ is the i^{th} eigenvector corresponding to the eigenvalue a_i, and d is the spatial dimension. Accordingly, the *damage driving energy density*, defined as the elastic energy density of $\langle\boldsymbol{\epsilon}\rangle_+$ is,

$$\phi_+(\boldsymbol{\epsilon}) := \phi(\langle\boldsymbol{\epsilon}\rangle_+) = \sqrt{\frac{1}{2}\langle\boldsymbol{\epsilon}\rangle_+ : \mathbf{C} : \langle\boldsymbol{\epsilon}\rangle_+}, \tag{2.3}$$

The damage force-type function, $\kappa_f(\boldsymbol{\epsilon})$, is expressed as,

$$\kappa_f(\boldsymbol{\epsilon}) = \frac{\phi_+(\boldsymbol{\epsilon}) - \phi_i}{\phi_c - \phi_i}, \tag{2.4}$$

where ϕ_i and ϕ_c are the minimum and maximum damage driving energy density limits. They correspond to fracture initiation and rupture under quasi-static loading condition, respectively. These values can be related to minimum and maximum damage driving strain limits ϵ_i and ϵ_c through Eq. (2.3). For example, in a 1D tensile experiment, ϵ_i and ϵ_c are strains at the start of softening region and full failure, respectively, for a quasi-static loading condition. For quasi-static monotonically increasing $\phi_+(\boldsymbol{\epsilon})$, the damage force is equal to the damage value, $\kappa = \kappa_f$. However, as mentioned earlier, the damage progress is not instantaneous in dynamic conditions. The model from [19] expresses damage evolution by

the following ordinary differential equation,

$$\frac{\mathrm{d}\kappa}{\mathrm{d}t} = \kappa_{\mathrm{src}}(\kappa, \epsilon) = \frac{1}{\tau_c}(1 - e^{-a\langle \kappa_f - \kappa \rangle_+}), \tag{2.5}$$

where $\kappa_{\mathrm{src}}(\kappa, \epsilon)$ is the general form of an evolution law. In this study, we assume that it takes the particular form on the right hand side, where τ_c and a are called the *relaxation time* and *brittleness parameter*, respectively. For a larger timescale parameter the damage evolution process takes longer time to be fully activated, and a higher value of brittleness parameter corresponds to a more brittle response. The positive operator in $\langle \kappa_f - \kappa \rangle_+$ ensures that damage is a nondecreasing function of time, and the form of equation implies that $\mathrm{d}\kappa/\mathrm{d}t \to 0^+$ as $\kappa \to \kappa_f$. The latter condition clarifies the interpretation of κ_f as the quasi-static damage limit.

Damage model parameters can be obtained through 1D tensile tests. As mentioned before, ϵ_i and ϵ_c correspond to the start of softening region and full failure, respectively. Experimentally, strain versus stress responses for different loading rates can be obtained. It is expected that higher rates result in higher maximum attainable stress and dissipated energy. Having the history of stress versus strain, one can calibrate the damage parameter as a function of strain for different loading rates. The process for calibrating a damage model can for example be found in [101]. Once the damage evolution for different strain rates is calibrated, the specific form of κ_{src} is determined in Eq. (2.5). The evolution function may not necessarily match the particular form provided with the relaxation time τ_c. However, in [19, 111] it is claimed that this evolution law accurately represents damage evolution for materials considered therein. If this time-delay form of κ_{src} is chosen, the value of τ_c can be obtained by a best fit of damage evolution history for one or multiple strain rate 1D experiments.

In conjunction with dynamics analysis, the delay model introduces a *damage length scale*, $l_c = c_{\mathrm{d}}\tau_c$, which is proportional to longitudinal elastic wave speed c_{d} [19, 111]; for mode *II* fracture problems, it is more appropriate to use the shear wave speed to determine l_c. Therefore, it is crucial for the present formulation to be employed in genuine dynamic conditions where elastic wave speeds are relevant and can provide the length scale l_c.

Otherwise, as noted in [78] for very low loading rates, *i.e.,* for quasi-static conditions, this model may exhibit mesh sensitivity—an issue not relevant to the present study dealing with elastodynamic problem. Under dynamic conditions, l_c provides a scaling for damage process zone size, *i.e.,* the width of the region where damage localization occurs and $\kappa \to 1$.

This damage equation only needs the initial condition $\kappa(\mathbf{x}, t = 0) = \underline{\kappa}(\mathbf{x})$ without any boundary condition, since Eq. (2.5) is a first order ODE. This feature is contrasted with other non-local methods such as gradient-enhanced and phase-field approaches in that they require some extra boundary conditions. The initial state is often considered damage-free, that is $\underline{\kappa}(\mathbf{x}) = 0$, an assumption taken for the remainder of the manuscript.

2.3.2 Elastodynamics equations

The conservation of linear momentum reads as,

$$\nabla \cdot \boldsymbol{\sigma} + \rho \mathbf{b} = \dot{\mathbf{p}}, \tag{2.6}$$

where $\boldsymbol{\sigma}$, $\mathbf{b}$, and $\mathbf{p}$ are the second order Cauchy stress tensor, body force, and linear momentum density, respectively. The linear momentum density is defined as $\mathbf{p} = \rho \dot{\mathbf{u}}$, where ρ is the mass density. Moreover, the compatibility conditions $\mathrm{d}\boldsymbol{\epsilon}/\mathrm{d}t = \nabla^{\mathrm{s}}\mathbf{v}$ and $\mathrm{d}\mathbf{u}/\mathrm{d}t = \mathbf{v}$ are added to Eq. (2.6) to form a system of first order differential equations. In the context of continuum damage mechanics [88], the effect of material degradation is considered by a modification of the linear elastic constitutive law. There exist many modified constitutive laws for different applications, and the authors adopt a simple isotropic model advocated by [92],

$$\boldsymbol{\sigma} = (1 - \kappa)\, \mathbf{C} : \boldsymbol{\epsilon}. \tag{2.7}$$

The governing equations (Eqs. 2.5 and 2.6) set a nonlinear hyperbolic system which are coupled through the constitute laws relations (Eqs. 2.3 and 2.7) and compatibility conditions.

2.4 Implementation by the aSDG method

In this section, the authors briefly review main ideas and features of the aSDG method that will be used as the computational framework for the damage-elastodynamics equations. Further details are discussed in [7, 9] for elastodynamics and fracture applications.

2.4.1 Causality-based spacetime meshing and solution scheme

In the aSDG method, basis functions are selected as piecewise polynomial functions that are discontinuous across all element boundaries. Unlike continuous finite element methods where displacement continuity is satisfied *a priori*, this continuity is satisfied weakly through the boundaries of the elements in spacetime. The governing equations are discretized in spacetime using unstructured elements with a particular causality constraint as described below. Similar to other discontinuous Galerkin (DG) methods, the aSDG method is very appropriate for the solution of hyperbolic PDEs due to its better performance in dealing with high gradient and nonsmooth solution features, more flexible adaptive operations, and linear solution complexity versus the number of elements.

As shown in Fig. 2.1, a simple unstructured causal spacetime mesh is chosen to describe basic features of the aSDG framework. The fastest characteristic directions are depicted by inclined arrows, assuming uniform wave speeds across the domain. The causality constraint means each facet must be faster (closer to horizontal) than the fastest characteristic direction traversing the facet. This *causality constraint* provides a dependency map between the solution of adjacent elements.

In a causal mesh, the solution on any element depends only on initial and boundary information and the solutions on its prior immediate neighbors. For example, the solution on element A depends only on the solutions on the elements B and C as its earlier neighbors. In Fig. 2.1 the *causal inflow* and *causal outflow* boundaries are highlighted by red and green lines, respectively. Using the *causality constraint*, the global solution can be computed locally, one element at a time. For instance in Fig. 2.1, the solutions on elements labeled by 1 depend only on initial conditions (and boundary conditions for elements E and F). Therefore,

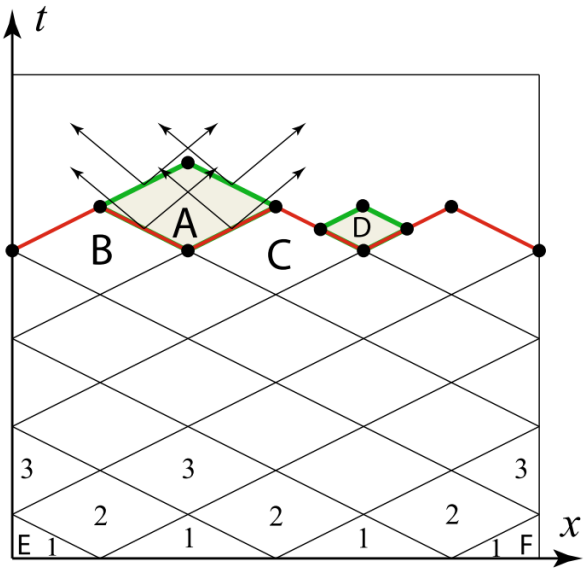

Figure 2.1: SDG Solution scheme on a causal spacetime mesh in $1d\times$time. Reproduced from [6].

solutions of the elements on the level-1 can be locally calculated, simultaneously in parallel or any order. For solving a level-2 element, there is no need to have the entire solution for all level-1 elements; a level-2 element only needs solutions of its earlier neighbors. Thus, the element-by-element solution of the aSDG method enables the asynchronous feature, linear computational complexity with respect to the number of spacetime elements [6]. In 2D and 3D problems, the *Tent Pitcher* algorithm [1] is used to erect *patches* of simplicial elements that fill the spacetime domain by a few element at a time until the final time of the simulation is reached. Further details about the aSDG method for the solution of elastodynamics can be found in [1, 7, 8, 6].

2.4.2 aSDG formulation for the damage evolution

For the following discussion, we consider a general form for damage evolution source term $\kappa_{\text{src}}(\kappa, \epsilon)$ in Eq. (2.5). We consider the problem on the spacetime domain $\mathcal{D} = \mathcal{D}_x \times [0,\ \bar{T}]$, where $\mathcal{D}_x$ is the spatial domain and $\bar{T}$ is the final time. From continuum mechanics perspective, the satisfaction of a balance law over arbitrary domains is equivalent to a *diffuse equation* and a *jump condition*. The diffuse equation is the differential equation

corresponding to the balance law. The jump condition holds across any arbitrarily-oriented manifold in spacetime, particularly across the jump manifold Γ_J where the field κ suffers a nontrivial jump. For Eq. (2.5) these equations are,

$$(\dot{\kappa} - \kappa_{\text{src}})|_{\mathcal{D}\setminus\Gamma_J} = 0 \tag{2.8a}$$

$$(\kappa^+ - \kappa^-)\star \mathrm{d}t|_{\Gamma_J} = 0 \tag{2.8b}$$

where Eq. (2.8a) is the ODE satisfied everywhere except the jump set $(\mathcal{D} \setminus \Gamma_J)$. The jump condition for balance laws states that the difference between the traces of the spatial (spacetime) flux density, denoted by superscripts $+$ and $-$ in Fig. 2.2, times spatial (spacetime) normal vector is zero for static (dynamic) problems. Since the dynamic problem considered herein is an ODE, the spatial flux density is zero and the corresponding spacetime flux density (space followed by time) is $\mathbf{F} = [\mathbf{0}, \kappa]$. Assuming that a spacetime normal can be defined on Γ_J as shown in Fig. 2.2, the spacetime normal is $\mathbf{N} = [\mathbf{n}_\mathbf{x}, n_t]$ and the jump condition reads as $(\mathbf{F}^+ - \mathbf{F}^-).\mathbf{N} = (\kappa^+ - \kappa^-).n_t = 0$. The problem with aforementioned argument is the inability to objectively define the normal vectors in spacetime. The effect of the restriction of the differential form $\star \mathrm{d}t$ on Γ_J in Eq. (2.8b) is similar to taking the spatial projection of surface differential $n_t \, \mathrm{d}S$ as shown in the figure. Thus, it effectively enforces the equation $(\kappa^+ - \kappa^-).n_t = 0$ on Γ_J without the need to define a normal vector.

For discrete formulation of this problem, the spacetime domain $\mathcal{D}$ is discretized by simplicial elements, *e.g.,* triangular elements for $d = 1$ in Fig. 2.2. Given that the solution is smooth inside a finite element $\mathcal{Q}$ and can suffer jump on its boundary $\partial\mathcal{Q}$, Eq. (2.8a) and Eq. (2.8b) are used to define interior and boundary residuals of the element in the context of a weighted residual method. Moreover, instead of expressing the jump condition Eq. (2.8b) between the traces of κ from the two sides of $\partial\mathcal{Q}$, we specify the jump between the so-called *target flux* κ^* and interior trace of the element κ. The introduction of target flux is needed for flux-based discontinuous Galerkin formulations. Thus, the interior and boundary residuals are $\dot{\kappa} - \kappa_{\text{src}}$ and $\kappa^* - \kappa$, respectively. The integration of the product of

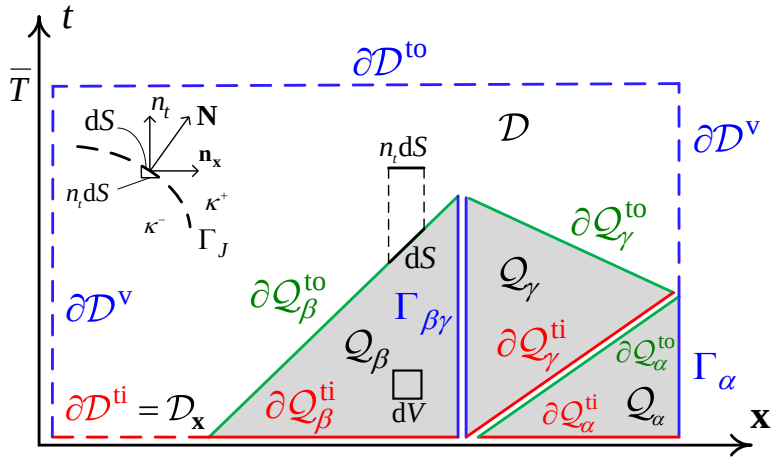

Figure 2.2: A discrete spacetime domain for a problem in $\mathbb{E}^1 \times \mathbb{R}$.

residuals by weight function $\hat{\kappa}$ in $\mathcal{Q}$ and $\partial\mathcal{Q}$ yields the weighted residual formulation,

$$\int_{\mathcal{Q}} \hat{\kappa}\ (\dot{\kappa} - \kappa_{\text{src}})\ \mathbf{\Omega} + \int_{\partial\mathcal{Q}} \hat{\kappa}\ (\kappa^* - \kappa)\ \star \mathrm{d}t = 0, \tag{2.9}$$

where $\mathbf{\Omega}$ is the $(d+1)$-volumetric differential form. The expressions of the differential forms in Eq. (2.9) for $d = 2$ are $\star \mathrm{d}t = \mathrm{d}x_1 \wedge \mathrm{d}x_2$ and $\mathbf{\Omega} = \mathrm{d}x_1 \wedge \mathrm{d}x_2 \wedge \mathrm{d}t$, where "$\wedge$" is the exterior product operator on forms [107, 52]. $\mathbf{\Omega}$ resembles volumetric differential $\mathrm{d}V$ and as mentioned $\star \mathrm{d}t$ resembles spatial projection of the surface differential $n_t\, \mathrm{d}S$; *cf.* Fig. 2.2. We refer the reader to [7, 10] for the expression of balance laws, PDEs, and jump conditions using differential forms for more general problems and the discussion on the advantage of differential forms to tensorial notation for spacetime problems.

For each point on $\partial\mathcal{Q}$, the numerical fluxes are solved by the solution to a local Riemann problem. For a simple ODE such as Eq. (2.5) the target value is simply the temporal upstream, *i.e.,* earlier, value across an interface. The use of $\star \mathrm{d}t$ on $\partial\mathcal{Q}$ is a result of the characteristics of this ODE being in the vertical time direction. The second integration can

be divided into three types of integrations over the element boundary as,

$$\int_{\partial\mathcal{Q}} \hat{\kappa}\ (\kappa^* - \kappa_{\text{src}})\ \star \mathrm{d}t = \int_{\partial\mathcal{Q}^{\text{ti}}} \hat{\kappa}\ (\kappa^* - \kappa_{\text{src}})\ \star \mathrm{d}t + \int_{\partial Q^{\text{to}}} \hat{\kappa}\ (\kappa^* - \kappa_{\text{src}})\ \star \mathrm{d}t + \int_{\Gamma} \hat{\kappa}\ (\kappa^* - \kappa_{\text{src}})\ \star \mathrm{d}t, \tag{2.10}$$

where ∂Q^{ti}, ∂Q^{to}, and Γ are temporal inflow, temporal outflow, and vertical boundaries of $\mathcal{Q}$, respectively. A schematic representation of these boundaries for three elements labeled by α, β, and γ is depicted in Fig. 2.2. The *temporal inflow* and *temporal outflow* boundaries, shown by red and green lines respectively, correspond to parts of $\partial\mathcal{Q}$ where the time direction is entering or exiting $\partial\mathcal{Q}$. The remaining boundaries which are not temporal inflow and temporal outflow are vertical boundaries and are highlighted by blue color. For the elastodynamic problem, the two elements $\mathcal{Q}_\beta$ and $\mathcal{Q}_\gamma$ are coupled as the elastic waves traverse $\Gamma_{\beta\gamma}$ from both sides. Thus, these two elements should be solved simultaneously in a *patch* comprised of them. In the non-adaptive aSDG implementation, which is employed herein, all faces that are interior to a patch, *i.e.,* $\Gamma_{\beta\gamma}$, are vertical. Thus, given that the boundary integrals are carried over the vertical projection of boundary, the third term in Eq. (2.10) is identically zero for all elements.

Following the same argument, since the damage equation is an ODE, there is no boundary condition to be imposed. That is no κ^* is specified on Γ_α for element $\mathcal{Q}_\alpha$ and similar to elements $\mathcal{Q}_\beta$ and $\mathcal{Q}_\gamma$, the third integral in Eq. (2.10), corresponding to Γ_α, vanishes. The star value for temporal outflow boundaries is equal to the interior trace of the element, *i.e.,* $\kappa^* = \kappa$, and so the second term in Eq. (2.10) similarly vanishes. The only remaining term is the temporal inflow contribution. Since characteristics are along the time direction for ODEs, the target values are determined by earlier value in time. If there is no adjacent element on the temporal inflow faces of an element, as for $\partial\mathcal{Q}^{\text{ti}}_\alpha$ and $\partial\mathcal{Q}^{\text{ti}}_\beta$ for elements $\mathcal{Q}_\alpha$ and $\mathcal{Q}_\beta$ respectively, κ^* is set equal to the initial condition $\underline{\kappa}$. As mentioned before, the analysis is often starts for an initially intact domain for which $\underline{\kappa} = 0$ for all points on the initial boundary $\partial\mathcal{D}^{\text{ti}}$. On the other hand, for elements with adjacent neighbors to their temporal inflow faces, κ^* is the trace of κ from the temporal inflow neighbor. For example, κ^* for a point on $\partial\mathcal{Q}^{ti}_\gamma$ is set to κ on the corresponding neighbor point on $\partial\mathcal{Q}^{to}_\alpha$, the temporal outflow

boundary of element $\mathcal{Q}_\alpha$. The weak form and numerical treatments for elastodynamics equation are more complex than the damage ODE and are discussed in detail in [7, 9].

2.4.3 Numerical solution of discrete equations

The authors solve the elastodynamics-damage discrete equations as a nonlinear coupled system using the Newton-Raphson (NR) method. One of the numerical challenges in damage mechanics that affects convergence rate of the NR method is the zero stiffness issue when damage is equal to unity. There are several methods to address this; for example, it is common to multiply the damage term in Eq. (2.7) by a positive reduction factor less than unity. Although it seems that this loss of stiffness is a numerical issue, experimental observations show that brittle materials do not completely lose their stiffness at failure. This means that there is maximum threshold less than unity for damage value [122, 58, 117]. This specific level depends on many factors such as material property, geometry, and loading condition. Herein, the maximum admissible damage of $\kappa_{\max} = 0.95$ is assumed. This constraint is controlled by limiting the value of damage force in Eq. (2.5); that is, κ_f is replaced with $\min(\kappa_f, \kappa_{\max})$.

2.5 Numerical examples

To demonstrate the accuracy and robustness of the proposed formulation, the authors present three problems in this section. First, a 1D benchmark problem is used to demonstrate that the relaxation time indirectly introduces a length scale and damage localization size is independent of element size. Second, the bending problem examines different responses of the model under tensile and compressive stress conditions. Finally, the authors demonstrate the effect of loading rate in damage evolution of a 2D domain with two circular holes. Plain strain condition is assumed for the problems considered. Displacement vector and damage fields are interpolated by third order polynomial functions in spacetime.

Table 2.1: Material properties for problem 1.

Properties	Units	Values
E	GPa	57
ρ	gr/cm^3	2.28
τ_c	µs	2
t_{ramp}	µs	1
$\bar{\sigma}_{\max}$	GPa	0.057
ν	-	0
ϵ_i	-	0.0013
ϵ_c	-	0.0028
a	-	10

2.5.1 Damage localization in a 1D bar

The authors verify the mesh insensitivity of the proposed formulation through a well-known benchmark problem for dynamic damage localization [28, 31, 106, 18, 94, 111, 116]. In this problem, two stress waves travel towards each other, and damage instantaneously initiates at the collision point in the center of the bar. Experimental observations show that the strain-softening behavior is distributed over a region with a finite length. Therefore, in numerical methods, it is vital to recover the finite localization area, regardless of the mesh size.

The geometry of the problem is depicted in Fig. 2.3, and the material properties are listed in Table 2.1. Although this problem is truly one dimensional, the authors solve it as a two-dimensional problem with a zero Poisson's ratio, $\nu = 0$, and a large aspect ratio, $H/W = 100$. The mesh-dependency is studied by three structured triangular initial meshes consisting of 1×100, 2×200, and 4×400 divisions along W and H. Normal stresses are gradually applied at end boundaries and remain constant after the ramp time reported in Table 2.1. The ramp load is a third-order function with zero slopes at initial and peak points as shown in Fig. 2.4.

Figure 2.5 shows damage solutions in the bar at time 13.5 µs for all meshes. Due to the large aspect ratio in this problem and for a better representation of responses, results are presented for a symmetrical section at the middle of the bar with total length of 43 mm. As observed, the numerical method is mesh-insensitive, and a fixed finite localization zone

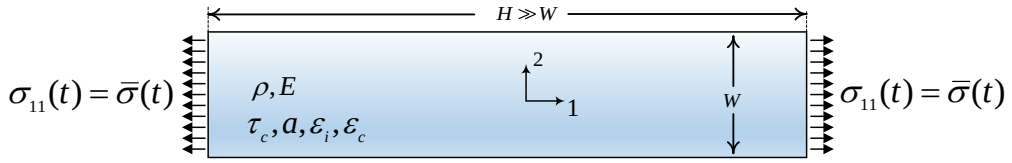

Figure 2.3: A one-dimensional rod with symmetric tensile loading.

is realized. If a region with full damage defined as the fracture zone, then the fracture zone length is approximately 4 mm which is in agreement with the results in [18].

Figure 2.6 depicts the elastic strain energy density $\phi(\boldsymbol{\epsilon})$ for each of the meshes used. It is evident that the field for the coarsest mesh is not symmetric with respect to the center of the bar and does not have adequate number of initial elements to properly capture the solution. Given the large errors of these results, the solution obtained by the coarsest mesh is deemed unsatisfactory. The time sequence of the damage and elastic strain energy density for the finest mesh is shown in Fig. 2.7 and Fig. 2.8, respectively.

Several points should be clarified regarding mesh insensitivity. First, mesh insensitivity refers to the convergence of the width of fracture zone (region with full damage) to a finite value as the element size tends to zero. Clearly, the results in Fig. 2.5 demonstrate such convergence and do not exhibit the problem of early damage formulations in which fracture zone converged to zero width in the limit of refinement. Second, given that the wave speed is $c = \sqrt{E/\rho} = 5\text{km/s}$ and $\tau_c = 2\ \mu\text{s}$, the intrinsic length scale implied for this choice of parameters is $l_c = c\tau_c = 10$ mm. The observed fracture zone width of 4 mm is related to the length scale l_c implied by the model and its specific value also depends on particular form of loading and geometry. Third, if the ramp time was very long, the loading would have been in quasi-static regime and l_c would not have been relevant under such loading condition.

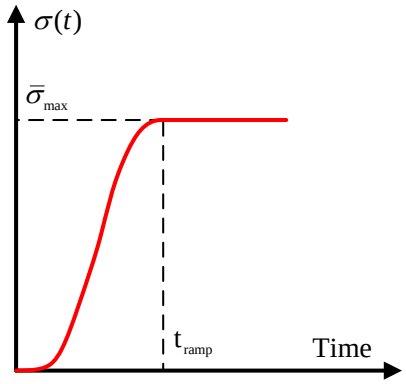

Figure 2.4: A third-order ramp function with zero slopes at initial and peak points.

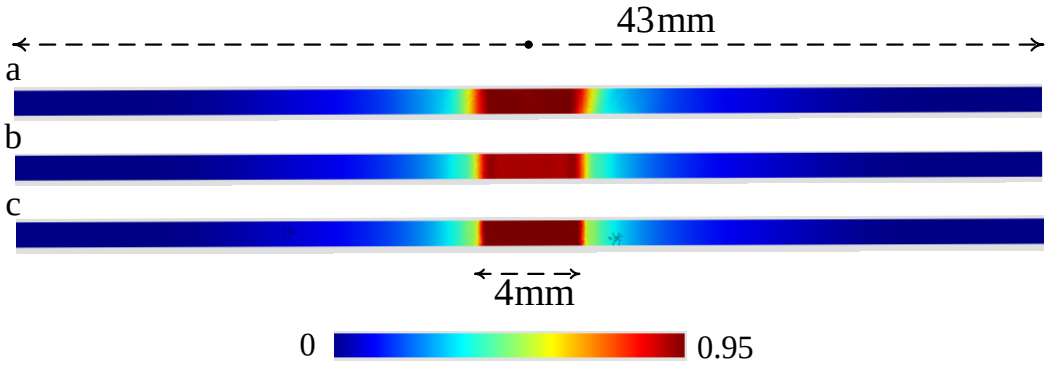

Figure 2.5: Damage profiles at time 13.5 μs for different initial meshes;(a) to (c) from coarsest to finest.

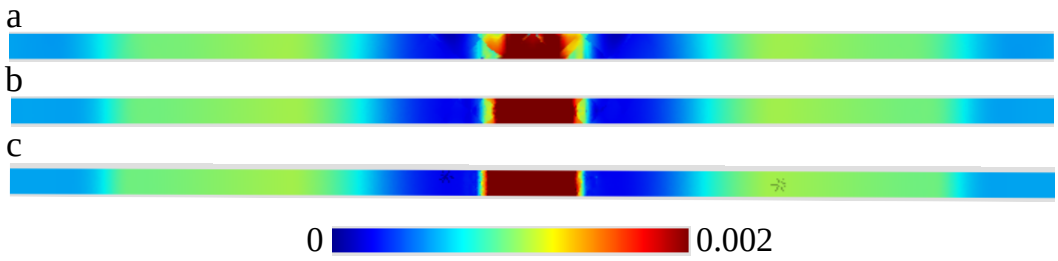

Figure 2.6: Elastic strain energy density profiles at time 13.5 μs for different initial meshes;(a) to (c) from coarsest to finest.

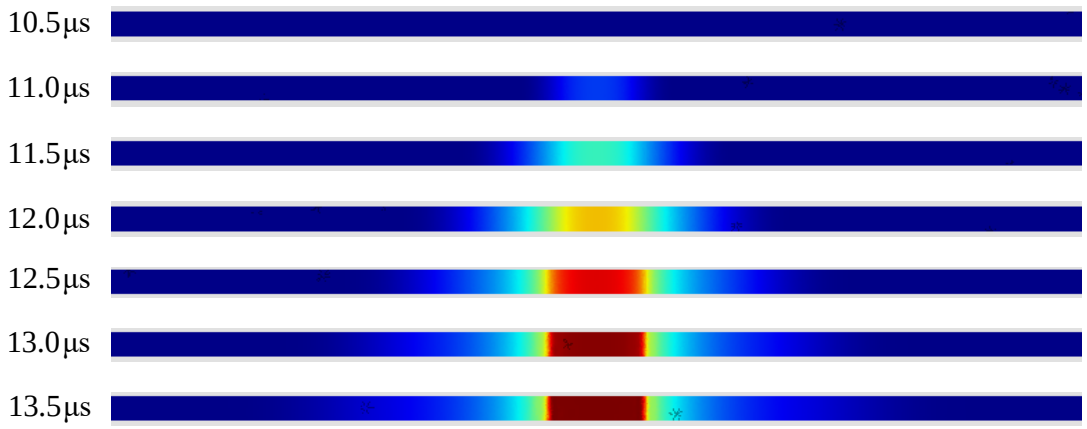

Figure 2.7: Damage profiles for the finest mesh at different times after the collision of two stress waves until full damage.

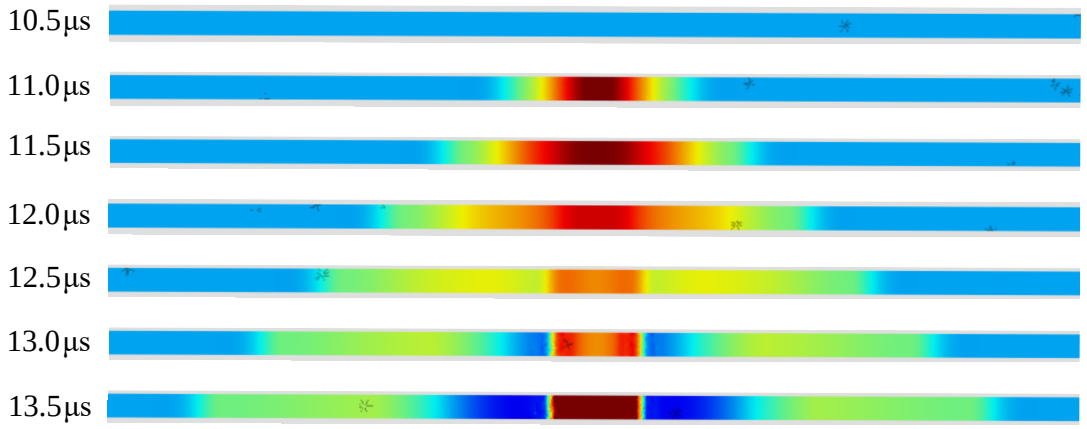

Figure 2.8: Elastic strain energy density profiles for the finest mesh at different times after the collision of two stress waves until full damage.

To conclude this section, we run the problem shown in Fig. 2.3 with non-zero Poisson ratio of $\nu = 0.15$ under plane strain condition for two different side boundary conditions. Referring to Fig. 2.4, the length of region at which load ramps from zero to $\bar{\sigma}_{\max}$ in direction 1 is $l_{\text{ramp}} = t_{\text{ramp}} c_{\text{d}}$, where c_{d} is the longitudinal wave speed for 3D and plane strain condition. For these problems, t_{ramp} is chosen such that $l' = l_{\text{ramp}}/W = 20.55$. For the *extension* problem, the long (top and bottom) sides are set to be traction free. The relatively large value of l' implies that σ_{12} and σ_{22} are close to zero compared to $\bar{\sigma}_{\max}$ and σ_{11} for the duration of simulation. This corresponds to $\epsilon_{11} > 0$ and $\epsilon_{22} \approx -\epsilon_{11}\nu/(1-\nu) < 0$. For the *tension* problem, symmetric boundary condition is employed for the two sides (zero normal velocity and shear stress). This problem possesses an ϵ_{11} field very close to the extension problem, but ϵ_{22} is identically zero. Since $\phi_+(\boldsymbol{\epsilon})$ in Eq. (2.3) is only a function of positive part of the strain tensor—which is almost identical between the two runs—we expect rather a similar damage pattern. The comparison of the solutions of these two problems in Fig. 2.9 verifies that the employed damage model predicts very close responses for extension and tension problems.

2.5.2 Bending of a rectangular plate

The stress field corresponding to this bending problem examines the performance of the damage formulation under mixed tensile and compressive loading condition. As shown in Fig. 2.10, the plate is fixed at the bottom side, and shear stresses are applied over the top boundary. The domain dimensions are $H = 100$ mm and $W = 40$ mm. The same ramp

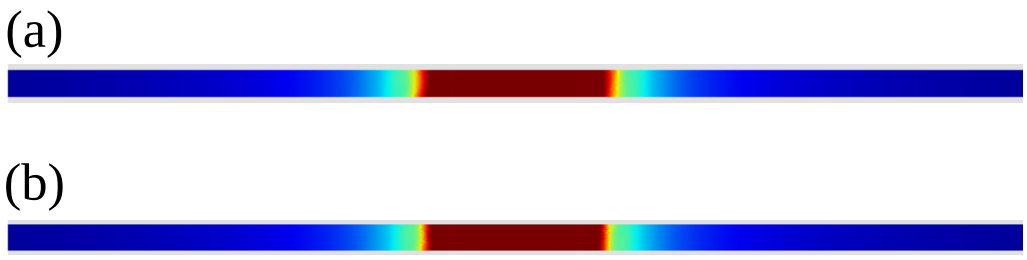

Figure 2.9: Damage response at time 17.5 μs for (a) extension and (b) tension conditions.

Table 2.2: Material properties for problem 2.

Properties	Units	Values
τ_c	μs	10
t_{ramp}	μs	10
$\bar{\sigma}_{\max}$	GPa	0.015
ν	-	0.3
ϵ_i	-	0.0011
ϵ_c	-	0.0034
a	-	1

loading profile shown in Fig. 2.4 is employed for this problem with the sustained load and ramp time shown in Table 2.2. The material properties not listed in this table are similar to those from the previous problem. Three structured triangular initial meshes consisting of 8×20, 16×40, and 32×80 side divisions are depicted in Fig. 2.11. Figure 2.12 presents damage maps corresponding to each of the initial meshes. The convergence between results is acceptable. Besides, the damage zone is not shrunk into the smallest element as the mesh size is decreased.

Figure 2.13 and Fig. 2.14 show damage and elastic strain energy density evolutions at different times. In Fig. 2.13(a), before the stress wave reaches to the support, damage initiates from the point at the middle right side of the plate where the instantaneous maximum tensile stress is experienced. Subsequently, in Fig. 2.13(b) damage propagates toward the support, where the maximum static moment and high stress concentrations are expected due to the use of fixed boundary condition. There is a region with maximum elastic strain energy density along with the left side of the plate where the damage value is zero. The reason why no damage is accumulated in this region of high compressive stress is the inclusion of only the positive part of strain tensor in the definition of damage driving energy density; *cf.* Eq. (2.3). However, the presence of damage at the left corner is due to its complex two dimensional stress field. The observed damage pattern matches what is expected for brittle materials, as their tensile strength is lower than the compressive strength.

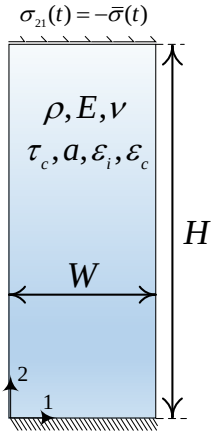

Figure 2.10: A bending plate with shear loading.

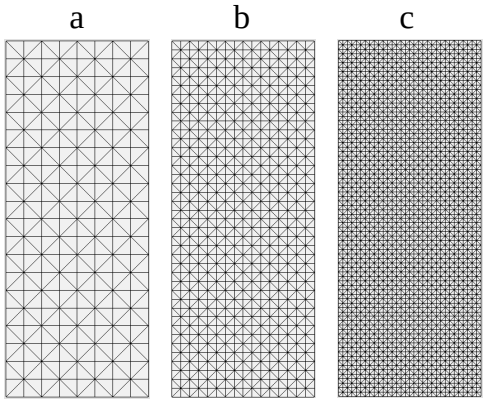

Figure 2.11: Different initial meshes used for the bending problem.

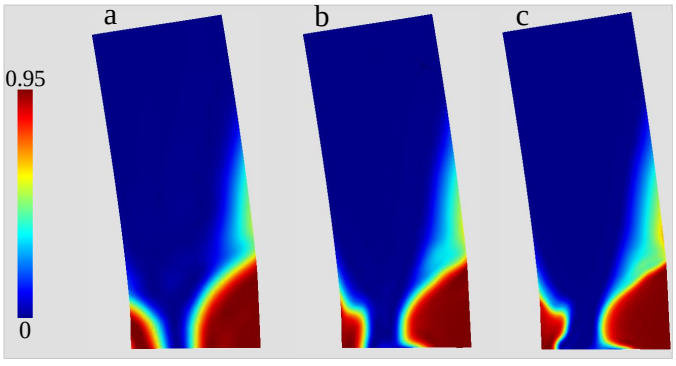

Figure 2.12: Damage profile at time 130 μs for different meshes used for the bending problem; (a) coarsest to (c) finest.

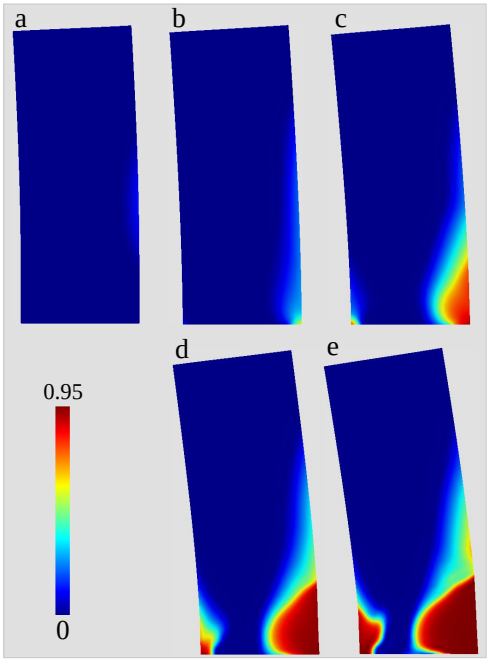

Figure 2.13: Damage evolution for the bending problem at different times [μs]; (a) 50; (b) 70; (c) 90; (d) 110; (e)130.

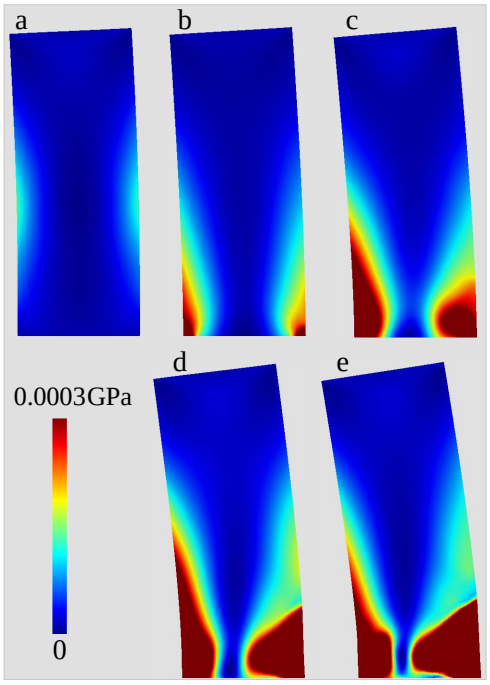

Figure 2.14: Elastic strain energy density evolution for the bending problem at different times [μs]; (a) 50; (b) 70; (c) 90; (d) 110; (e)130.

Table 2.3: Material properties for problem 3.

Properties	Units	Values
E	GPa	65
ρ	kg/m^3	2600
τ_c	µs	30
t_{ramp}	µs	10
ν	-	0.27
ϵ_i	-	0.000082
ϵ_c	-	0.0003
a	-	10

2.5.3 A plate with two holes under tension loading

The last problem studies the robustness of the formulation in complex geometries with initial holes and different loading conditions. As shown in Fig. 2.15(a), the domain is a 80×160 mm^2 rectangle with two circles with centers $\mathbf{c}$ and radii r: $\mathbf{c}_L = (20 \text{ mm}, 50 \text{ mm})$, $\mathbf{c}_R = (60 \text{ mm}, 110 \text{ mm})$, $r_L = 15$ mm, $r_R = 10$ mm, where L and R subscripts correspond to left and right circles, respectively. The authors use the unstructured mesh shown in Fig. 2.15(b). The material properties for a rock taken from [23] are listed in Table. 2.3. Uniform tensile stress is applied over the top boundary while the opposite boundary is kept fixed. While the ramp time for this problem is fixed, shown in the table, different maximum stress loads of $\bar{\sigma}_{\max} = 6.75$ MPa and $\bar{\sigma}_{\max} = 3.375$ MPa are studied for the ramp profile shown in Fig. 2.4.

Figure 2.16 shows the damage evolution at different times for $\bar{\sigma}_{\max} = 6.75$ MPa. As shown, damage initiates from early stages from the two ends of the plate. Then, dominant failure zones initiate from the stress concentration regions. At each stress concentration point in the middle of the plate, damage propagates toward the other stress concentration zone and also toward the corners of the plate. The final failure is an inclined shear-band that shows a mixed-mode failure pattern.

There are also two other damaged zones between the circles and free vertical boundaries. The left circle is bigger than the right one, and there is less material between this circle and the free surface boundary. This implies that it has a higher static stress concentration factor than the right circle. However, the failure zone close to the right circle is larger. This is due

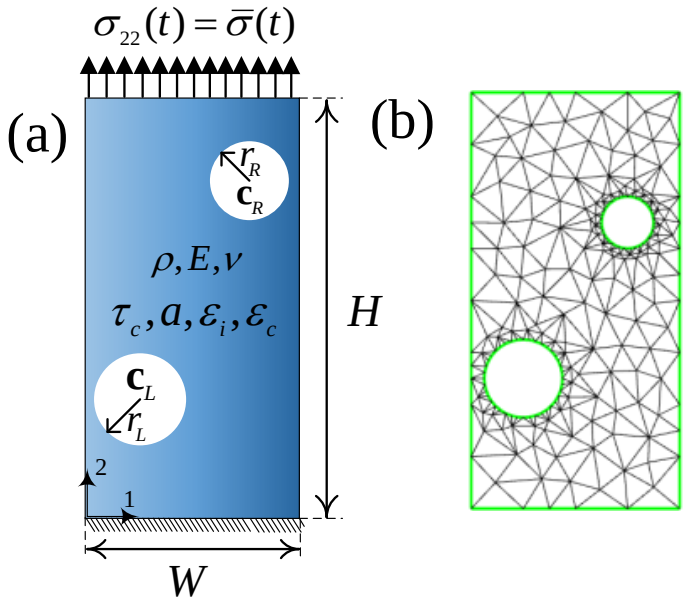

Figure 2.15: Geometry, boundary conditions, and the initial mesh for the last problem.

to further closeness of the right circle to the top loaded edge, hence the longer duration that the region between this circle and the side vertical boundary experiences high stresses before the full development of the shear-band. In contrast, under quasi-static loading condition, a more spread damaged zone to the side of the left circle would have been expected.

Figure 2.17 shows the damage evolution at different times for $\bar{\sigma}_{\max} = 3.375$ MPa. The damage pattern is entirely different for this low amplitude loading case. Unlike the former condition, the primary damage is generated in the region close to the left circle. This observation confirms the expectation for a more quasi-static loading condition as the larger hole introduces greater maximum stresses for a rectangle plate with constant width. The dominant failure zones initiate from stress concentration points and propagate in the direction normal to the boundary loads. Similar drastic changes in damage patterns, due to relatively small changes in the boundary condition, have been reported in literature, see for example [27].

As discussed before, the aSDG method advances the solution by an asynchronous patch-by-patch solution procedure. The time increment of a pitched vertex is calculated based on

the wave speed, spatial geometry, and sizes of elements around it. Thus, vertices surrounded by smaller elements typically have smaller local time advances. Another main difference from a conventional time marching scheme is that the direct discretization of spacetime eliminates the need for a separate time marching. To clarify these points and study the sensitivity of damage response to elements' local time advance size, we artificially decrease the time increment limit by factors of two and four for the problem presented in Fig. 2.16. The corresponding spacetime meshes for the three solutions are shown in Fig. 2.18. As can be seen, all spacetime meshes are unstructured and the instantaneous fronts are asynchronous.

The damage solutions for these meshes are compared in Fig. 2.19. The damage contours are very close for the three time advance set-ups considered. While all meshes have the same spatial resolution, the local time advances of the last solution are one fourth of those from the first solution; thus, the very minor differences observed are attributed to increased accuracy of solution from Fig. 2.19(a) to Fig. 2.19(c). Overall, the results suggest a mild dependency to local element (stable) time advances. It is noted that if the damage formulation did not imply an intrinsic length scale, we would expect damage patterns to be time advance-dependent similar to mesh-dependency implied by spatial mesh refinement.

2.6 Conclusion

The authors presented a time-delay damage formulation for elastodynamics. The weak statement and spacetime discontinuous Galerkin formulation of the damage evolution were presented. Consequently, the corresponding ODEs of the damage equation were coupled with elastodynamic equations for the solution of some sample problems by the aSDG method.

Some advantages of this damage formulation are: simplicity of the formulation without requiring any boundary conditions owing to the ODE form of its corresponding evolution equation; hyperbolicity of the coupled elastodynamic-damage equations; indirect introduction of a damage length scale from the multiplication of the model's relaxation time and the longitudinal or shear wave speed implied by the elastodynamic problem; mesh insensitivity without the use of high order spatial derivatives or nonlocal spatial averaging operators

owing to the existence of the damage length scale. However, it is noted that this model is mainly applicable to dynamic fracture where wave speeds are relevant.

The authors presented several numerical examples to demonstrate the robustness of the proposed method. Specifically, the mesh insensitivity of the formulation is shown using a 1D benchmark and a 2D bending problem. The bending problem also demonstrates different responses of the model under tensile and compressive stress conditions. One interesting observation from the last problem was the great impact load amplitude had on damage pattern.

There are several extensions to this work. First, the authors plan to use the h-adaptive formulation of the aSDG method [8] for more efficient solution of the continuum damage problem. Second, as demonstrated through the last problem, material defects greatly affect dynamic fracture response. The authors have used *statistical volume elements* (SVEs) to homogenize fracture strength of different materials [14, 24]. The random fields generated based on the statistics of the SVEs can be used to characterize macroscopic fracture response of composites without explicit resolution of their microstructure; see for example [41]. The authors believe that bulk damage models have several advantages over the interfacial ones used in their prior work and plan to formulate a microstructure-informed stochastic bulk damage model. Finally, the authors plan to implement more advanced and realistic hyperbolic damage models [110, 59, 60] and recently proposed phase field formulation [68] for the aSDG method given its numerous advantages for the solution of such PDEs.

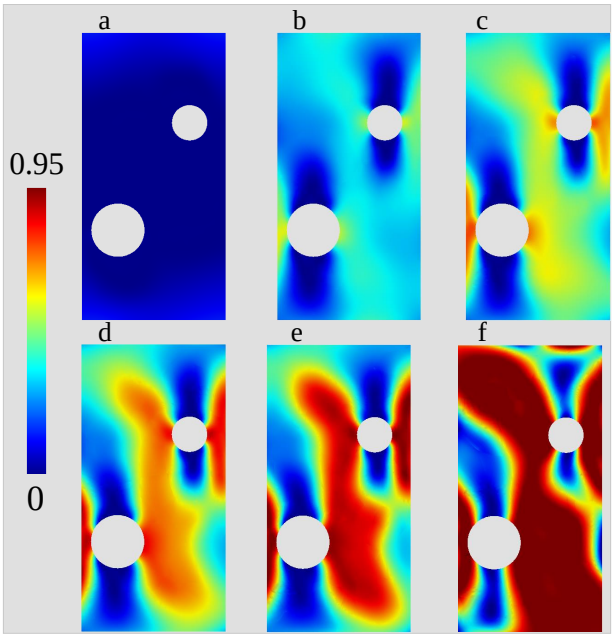

Figure 2.16: Damage evolution for the high amplitude loading case of the problem in Fig. 2.15 at different times [μs]; (a) 15; (b) 32; (c) 38; (d) 43; (e) 49; (f) 100.

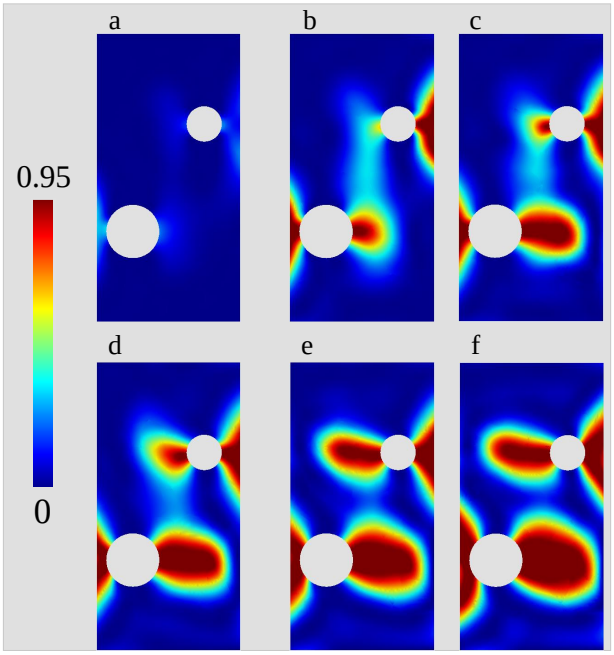

Figure 2.17: Damage evolution for the low amplitude loading case of the problem in Fig. 2.15 at different times [μs]; (a) 30; (b) 72; (c) 114; (d) 156; (e) 198; (f) 240.

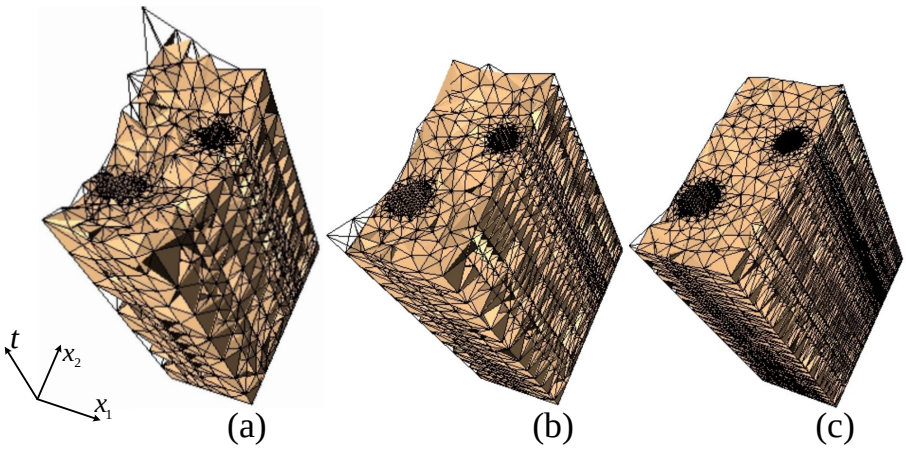

Figure 2.18: Spacetime mesh for the low amplitude loading case at time 10μs. Time increment limits in (b) and (c) are chosen half and quarter of (a), respectively.

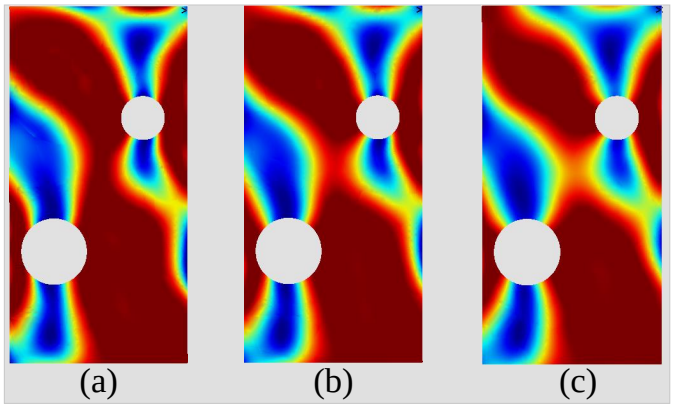

Figure 2.19: Damage contour for the low amplitude loading case at time 100μs. Time increment limits in (b) and (c) are chosen half and quarter of (a), respectively.

Chapter 3

A stochastic bulk damage model based on Mohr-Coulomb failure criterion for dynamic rock fracture

This chapter is revised based on the following published paper:

B. Bahmani, R. Abedi, P.L. Clarke, "A stochastic bulk damage model based on Mohr-Coulomb failure criterion for dynamic rock fracture", Applied Sciences, 9(5):830, 2019.

Following the previous chapter, my additional contributions in this paper can be listed as (i) extension of Allix's damage model for pressure sensitive materials based on Mohr-Coulomb failure criterion, (ii) development of stochastic damage model based the random field realization module built up by P.L. Clarke (iii) arrangement and interpretation of numerical examples, and (iv) preparation of the first draft.

3.1 Abstract

We present a stochastic bulk damage model for rock fracture. The decomposition of strain or stress tensor to its negative and positive parts is often used to drive damage and evaluate the effective stress tensor. However, they typically fail to correctly model rock fracture in compression. We propose a damage force model based on the Mohr-Coulomb failure criterion and an effective stress relation that remedy this problem. An evolution equation specifies the rate at which damage tends to its quasi-static limit. The relaxation time of the model introduces an intrinsic length scale for dynamic fracture and addresses the mesh sensitivity problem of earlier damage models. The ordinary differential form of the damage equation makes this remedy quite simple and enables capturing the loading rate sensitivity of strain-stress response. The asynchronous Spacetime Discontinuous Galerkin (aSDG) method is used for macroscopic simulations. To study the effect of rock inhomogeneity, the Karhunen-Loeve method is used to realize random fields for rock cohesion. It is shown that inhomogeneity greatly differentiates fracture patterns from those of a homogeneous rock, including the location of zones with maximum damage. Moreover, as the correlation length of the random field decreases, fracture patterns resemble angled-cracks observed in compressive rock fracture.

3.2 Introduction

Interfacial, *particle*, and *bulk* or *continuum* models form the majority of approaches used for failure analysis of quasi-brittle materials at continuum level. Interfacial models directly represent sharp fractures in the computational domain. Some examples are *Linear Elastic Fracture Mechanics* (LFEM), cohesive models [51, 25], and interfacial damage models [19, 16, 90, 89, 5]. Since cracks are explicitly represented, interfacial methods are deemed accurate when crack propagation is the main mechanism of material failure. However, external criteria are needed for crack nucleation and propagation (direction and extension). Moreover, accurate representation of arbitrary crack directions can be cumbersome in computational settings. Mesh adaptive schemes [108, 99, 13], *eXtended Finite Element Methods* (XFEMs) [32, 85, 70], and *Generalized Finite Element Methods* (GFEMs) [50, 109] address this problem to some extend. However, for highly dynamic fracture simulations and fragmentation studies, even these methods have challenges in accurate modeling of the fracture pattern. Particle methods such as *Peridynamics* [105, 57, 98] have been successfully used to model highly complex fracture patterns that are encountered in dynamic (rock) fracture. They model continua as a collection of interacting particles.

Bulk or *continuum* damage models approximate the effect of material microstructural defects and their evolution, *e.g.,* microcrack nucleation, propagation, and coalescence, through the evolution of a damage parameter. Due to the implicit representation of microcracks and other defects, bulk damage models are more efficient than interfacial and especially particle methods. In addition, damage pattern is obtained as a part of the solution and no external criteria are needed for crack nucleation and propagation. Finally, since damage is a smooth field interpolated within finite elements, complex fracture patterns can be easily modeled by damage models, wherein the thickness of cracks is effectively regularized by the damage field.

Earlier bulk damage models, however, suffered from mesh sensitivity problem where the width of the localization and damaged region was proportional to element size; as a result, finer meshes resulted in a more brittle fracture response. This problem is related to the loss of ellipticity/hyperbolicity of the (initial) boundary value problem for the earlier formulations

[73, 79], and can be resolved by the introduction of an intrinsic length scale to the damage evolution formulation. In gradient-based models, this is achieved by adding higher order derivatives of the damage or strain fields to the damage evolution equation [92, 42]. In nonlocal approaches, strain or damage field employed in a local damage formulation, is in turn computed over a neighborhood of finite size [94, 95]. Finally, time-relaxed damage formulations possess an internal time parameter which through its interaction with elastic wave speeds introduce a finite length scale for the damage model in transient settings [18, 80, 60, 67]. Related to these remedies is the *phase field* method which closely resembles a gradient-based damage model [46]. The sharper approximation of crack width is one of the main advantages of the phase field methods to gradient-based damage models [81].

We have presented a time-delay damage model for dynamic brittle fracture in [20]. The coupled elastodynamic-damage problem is solved by the *asynchronous spacetime Discontinuous Galerkin* (aSDG) method [7, 8]. This damage model addresses the mesh sensitivity problem of the earlier damage models by the third approach discussed above, in that, damage evolution is governed by a time-delay model. In addition, the existence of a maximum damage evolution rate results in an increase in both the maximum attainable stress and toughness as the loading rate increases. This loading rate dependency of strength and toughness is experimentally verified; see for example [95, 33]. Finally, the damage evolution law is an *Ordinary Differential Equation* in time. This greatly simplifies the damage model formulation and lends itself to the aSDG method; the aSDG method directly discretizes spacetime by elements that satisfy the causality constraint of the underlying hyperbolic problem being solved. The nonlocal damage models violate this causality constraint, whereas the majority of gradient-based damage models are not hyperbolic. In contrast, the time-delay damage model maintains the hyperbolicity of the elastodynamic problem. Besides, the ODE form of the governing equation greatly simplifies the application of initial and boundary conditions for the coupled problem.

The distribution of material defects at microstructure can have a great effect on macroscopic fracture response, particularly for quasi-brittle materials. Some examples are high variability in fracture pattern for samples with the same loading and geometry [15], high sensitivity of macroscopic strength and fracture toughness to microstructural variations [72],

and the so-called size effect [26, 102, 29], *i.e.,* the decrease of the mean and variations of fracture strength for larger samples. Weibull model [118, 119] is one of the popular approaches for modeling the effect of defects in quasi-brittle fracture, particularly the size effect. We have used the Weibull model in the context of an interfacial damage model to capture statistical fracture response of rock, in hydraulic fracturing [11], fracture under dynamic compressive loading [3], and in fragmentation studies [6, 41]. However, these models are computationally expensive due to the use of a sharp interfacial damage model.

In this manuscript, we propose a stochastic bulk damage model for rock fracture. There are two main differences to the damage model presented in [20]. First, in damage mechanics often only the spectral positive part of either strain or elastic stress tensor is used to drive damage accumulation. Moreover, upon full damage, only the negative part of the stress tensor is maintained in forming the effective stress. While these choices are appropriate for tensile-dominant fracture, they have some shortcomings for rock fracture under compressive loading. Specifically, using these models damage does not accumulate under compressive loading; even if it could, it would not have modeled the failure process as the effective stress remains the same as the elastic stress of the intact rock. Herein, we propose a new damage model based on the Mohr-Coulomb failure criterion and an effective stress that correctly represents rock failure in compression. Second, we employ a stochastic damage model wherein rock cohesion is treated as a random field. This aspect is important for the uniaxial compression examples considered, as due to the lack of macroscopic stress concentration points highly unrealistic fracture patterns will be obtained by using a homogeneous rock mass model. We note that the use of a bulk damage model makes the proposed approach significantly more efficient than the stochastic fracture problems [11, 3, 6, 41] studies by the authors using an interfacial damage model.

The outline of the manuscript is as follows. The formulation of the stochastic damage model, its coupling to elastodynamic problem, and the aSDG method are discussed in §3.3. We use a dynamic uniaxial compressive example to demonstrate the effect of material inhomogeneity on fracture response in §3.4. Final conclusions are drawn in §4.5.

3.3 Formulation

The first three subsections are pertained to the formulation of damage model. In §3.3.1 the formulation of the damage force parameter based on the Mohr-Coulomb (MC) failure criterion and the damage evolution equation are provided. In §3.3.2 the coupling of elasticity and damage problems through the effective stress is described. Certain properties of the damage model are discussed in §3.3.3. A brief description of the aSDG method and the implementation of the damage model is provided in §3.3.4. Finally, the stochastic aspects of the damage model are explained in §3.3.5.

3.3.1 Bulk damage problem description

3.3.1.1 Damage driving force

As will be discussed in §3.3.2, the damage parameter $D \in [0,\ 1]$ gradually reduces the elasticity stiffness in the process of material degradation. Damage evolution if generally driven by the strain field $\boldsymbol{\epsilon}$. For the remainder of the manuscript, we assume that the spatial dimension is two. The symmetric *elastic stress tensor* $\boldsymbol{\sigma}$ is defined as,

$$\boldsymbol{\sigma} = \mathbf{C}\boldsymbol{\epsilon}, \qquad \text{where} \quad \boldsymbol{\sigma} = \begin{bmatrix} \sigma_{xx} & \sigma_{xy} \\ \sigma_{yx} & \sigma_{yy} \end{bmatrix} \quad \text{and} \quad \boldsymbol{\epsilon} = \begin{bmatrix} \epsilon_{xx} & \epsilon_{xy} \\ \epsilon_{yx} & \epsilon_{yy} \end{bmatrix} \tag{3.1}$$

are the expressions of stress and strain tensors in global coordinate system (x, y) and $\mathbf{C}$ is the elasticity tensor. Instead of $\boldsymbol{\epsilon}$, damage evolution can be expressed in terms of $\boldsymbol{\sigma}$. This is more suitable for rock fracture given that many known *failure criteria* such as *Mohr-Coulomb* (MC) or Hoek-Brown [64] are expressed in terms of the stress tensor. Figure 3.1 shows the Mohr-Coulomb failure criterion in terms of normal σ and shear τ traction components on a fracture surface. We employ the tensile positive convention for σ. The failure criterion is determined by the *cohesion* $\underline{c}$ and *friction angle* $\phi = \tan^{-1}(k)$, where k is the friction coefficient. In the figure, the Mohr circle for a stress tensor A (red semi-circle) corresponding to principal stresses $\sigma_2 < \sigma_1$ is shown. Since only isotropic rocks are considered herein, $\underline{c}$ and ϕ are assumed to be constant with respect to the orientation of principal stresses (with

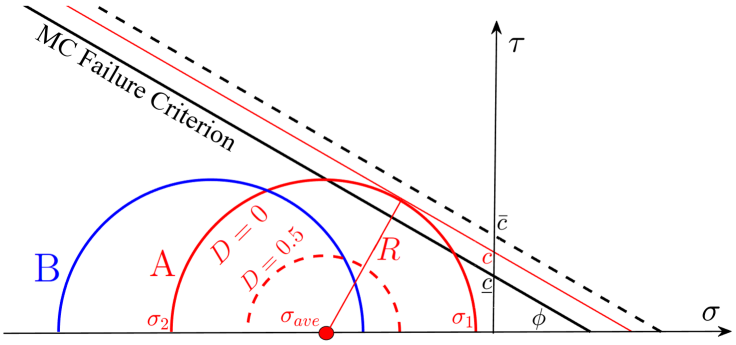

Figure 3.1: Mohr-Coulomb failure criterion and scalar stress c for a given stress state.

respect to the global coordinate system axes). We define the *scalar stress* as,

$$c(\boldsymbol{\sigma}, \phi) := \frac{R}{\cos\phi} + \sigma_{ave} \tan\phi \tag{3.2}$$

where as shown in Fig. 3.1, c is the ordinate of the tangent line on the Mohr-circle with angle ϕ, and the radius R and average normal stress σ_{ave} are given by,

$$R := \frac{\sigma_1 - \sigma_2}{2} = \sqrt{\frac{(\sigma_{xx} - \sigma_{yy})^2}{4} + {\sigma_{xy}}^2}, \tag{3.3a}$$

$$\sigma_{ave} := \frac{\sigma_1 + \sigma_2}{2} = \frac{\sigma_{xx} + \sigma_{yy}}{2}, \tag{3.3b}$$

Figure 3.1 shows two stress states. For the stress state B, the entire Mohr circle is below the failure criterion curve, thus no degradation is expected. For the stress state A, the Mohr circle expands beyond the failure criterion curve; in a binary intact and failed classification, this stress state would be considered failed. These stages correspond to $c(\boldsymbol{\sigma}, \phi) < \underline{c}$ and $c(\boldsymbol{\sigma}, \phi) \geq \underline{c}$, respectively. Some specific strengths corresponding to the

MC criterion $c(\boldsymbol{\sigma}, \phi) = \underline{c}$ are shown in Fig. 3.2 and are given by,

$$\underline{s}_{\text{ht}} = \frac{\underline{c}}{\tan\phi} \qquad \text{Hydrostatic tensile strength} \tag{3.4a}$$

$$\underline{s}_{\text{at}} = \frac{2\underline{c}\cos\phi}{1+\sin\phi} \qquad \text{Uniaxial tensile strength} \tag{3.4b}$$

$$\underline{s}_{\text{s}} = \underline{c}\cos\phi \qquad \text{Shear strength} \tag{3.4c}$$

$$\underline{s}_{\text{ac}} = \frac{2\underline{c}\cos\phi}{1-\sin\phi} \qquad \text{Uniaxial compressive strength} \tag{3.4d}$$

As will become clear later, the damage model, regularizes the process of failure. Otherwise, failure for a stress state occurs instantaneously once MC criterion $c(\boldsymbol{\sigma}, \phi) = \underline{c}$ is satisfied; for example, when $\sigma_{xx} = \sigma_{yy} > 0$ reaches $\underline{s}_{\text{ht}}$ ($\sigma_{xy} = 0$). To facilitate this, the *damage force* is defined as,

$$D_f(c, \underline{c}, \bar{c}) := \begin{cases} 0 & c \leq \underline{c} \\ \frac{c-\underline{c}}{\bar{c}-\underline{c}} & \underline{c} < c < \bar{c} \\ 1 & \bar{c} \leq c \end{cases} \tag{3.5}$$

where $\bar{c}$ corresponds to the ordinate of the upper MC line shown in dashed line in Fig. 3.1. The *brittleness* factor β defines a relation between the two MC lines through $\underline{c} = \beta\bar{c}$. In the absence of the damage model, complete failure occurs for any positive value of D_f as the Mohr circle expands over the failure criterion. However, in the context of the damage model, D_f corresponds to the quasi-static damage value for a given strain $\boldsymbol{\epsilon}$, which through (3.1) and (3.2) defines c. For example, for the strain (elastic stress) state A in Fig. 3.1, $D_f = 0.5$.

3.3.1.2 Damage evolution law

The damage value can be taken to be equal to the damage force. However, this local definition of D has several shortcomings, as will be discussed below and in §3.3.3.2. We employ the time-delay model in [18, 19] for damage evolution. The rate of damage evolution, $\dot{D}$, is given

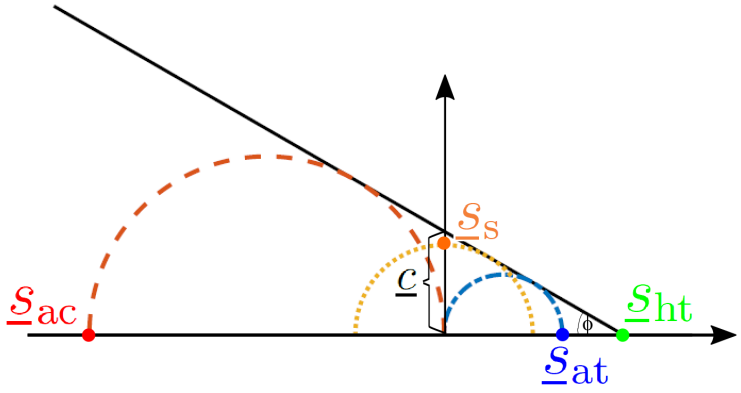

Figure 3.2: Relation of different fracture strengths.

by,

$$\dot{D} = \begin{cases} D_{\text{src}}(D, D_f) = \frac{1}{\tau_c}(1 - e^{-a\langle D_f - D\rangle}) & D < 1 \\ 0 & D = 1 \end{cases} \tag{3.6}$$

where $D_{\text{src}}(D, D_f)$ is a general source term for the evolution equation $\dot{D} = D_{\text{src}}(D, D_f)$. This function can be calibrated from experimental strain-stress results, for example, for uniaxial tensile/compressive loading. The specific form of $D_{\text{src}}(D, D_f)$ is taken from [19, 111] as it is claimed to accurately model materials' rate effect; *cf.* §3.3.3.2. In addition, τ_c is the *relaxation time*, a is the *brittleness exponent*, and $\langle . \rangle$ is the Macaulay positive operator.

Albeit its simplicity, this evolution model incorporates several essential characteristics of real materials. First, we observe that the damage evolution is governed by the difference of damage D and damage force D_f. The higher the difference, the higher the damage rate. Moreover, when $D = D_f$, damage evolution terminates. That is, D_f is the *target damage* value; if D is smaller than the target value, it evolves until it reaches D_f. Second, damage cannot instantaneously reach D_f given that $\dot{D}$ is bound by the maximum damage rate $1/\tau_c$. As will be discussed in §3.3.3.2, this results in the rate-sensitivity of strain-stress response. Third, the positive operator ensures that damage is a nondecreasing function in time (no material healing processes). Finally, Fig. 3.3 shows the effect of a; for higher values of a, even small differences between D_f and D, quickly jumps up the damage rate close to its maximum value of $1/\tau_c$; implying a more brittle response.

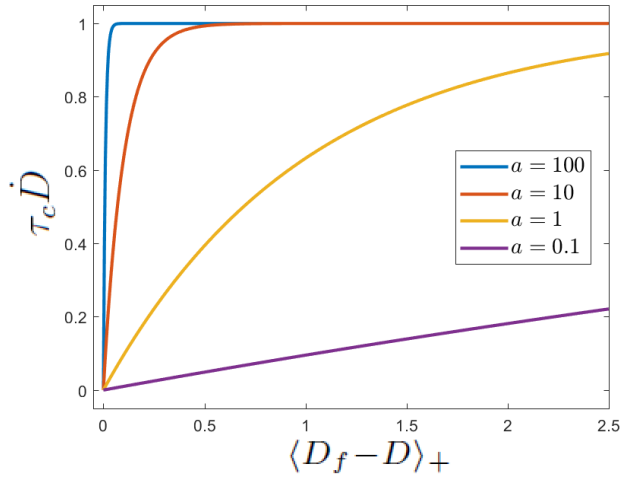

Figure 3.3: The effect of brittleness exponent a on the rate of damage evolution.

3.3.2 Coupling of damage and elastodynamic problems

The equation of motion, corresponding to strong satisfaction of the balance of linear momentum for elastodynamic problem, reads as,

$$\nabla \cdot \boldsymbol{\sigma}_{\text{eff}} + \rho \mathbf{b} = \dot{\mathbf{p}}, \tag{3.7}$$

where $\boldsymbol{\sigma}_{\text{eff}}$, $\mathbf{b}$, and $\mathbf{p}$ are the effective stress tensor, body force, and linear momentum density, respectively. The linear momentum density is defined as $\mathbf{p} = \rho \dot{\mathbf{u}}$, where ρ is the mass density. This equation is augmented by the compatibility equations between displacement, velocity, and strain, and initial/boundary conditions to form the elastodynamic initial boundary value problem.

The coupling between damage and elastodynamic problems is through the effective stress tensor $\boldsymbol{\sigma}_{\text{eff}}$. In the simplest form, the scalar damage parameter D linearly degrades the elasticity stiffness tensor, that is $\boldsymbol{\sigma}_{\text{eff}} = (1 - D)\boldsymbol{\sigma} = (1 - D)\mathbf{C}\boldsymbol{\epsilon}$ [92]. However, in more advanced damage-elasticity constitutive equations, only certain parts of the elastic stress (or elastic strain) are degraded by D [88]. By inspecting Fig. 3.1 and Fig. 3.2, it is observed that damage is induced by high tensile and shear stresses and no damage is induced by a hydrostatic compressive stress state ($\sigma_1 = \sigma_2 < 0$). Accordingly, we define a consistent damage-elasticity constitutive equation in which the entire elastic stress, except

its hydrostatic compressive part, are degraded by D. That is,

$$\boldsymbol{\sigma}_{\text{eff}} = (1-D)\boldsymbol{\sigma}_d + (1-D)\langle\boldsymbol{\sigma}_h\rangle + \langle\boldsymbol{\sigma}_h\rangle_- \tag{3.8}$$

where σ_h and σ_d are hydrostatic and deviatoric parts of $\boldsymbol{\sigma}$. The positive and negative ($\langle\boldsymbol{\sigma}_h\rangle_- = \boldsymbol{\sigma}_h - \langle\boldsymbol{\sigma}_h\rangle$) parts of $\boldsymbol{\sigma}_h$ correspond to the hydrostatic tensile and compressive stresses of $\boldsymbol{\sigma}$. For example, if $\sigma_2 \leq \sigma_1$ are the principal values of $\boldsymbol{\sigma}$, $\boldsymbol{\sigma}_d$, $\langle\boldsymbol{\sigma}_h\rangle$, and $\langle\boldsymbol{\sigma}_h\rangle_-$ have the principal values of $[(\sigma_2-\sigma_1)/2, (\sigma_1-\sigma_2)/2]$, $[\langle(\sigma_2+\sigma_1)/2\rangle, \langle(\sigma_2+\sigma_1)/2\rangle]$, and $[\langle(\sigma_2+\sigma_1)/2\rangle_-, \langle(\sigma_2+\sigma_1)/2\rangle_-]$, respectively, all with the same principal directions. Clearly, they correspond to the pure shear, tensile, and compressive parts of $\boldsymbol{\sigma}$.

3.3.3 Properties of the damage model

We first discuss the properties of the damage force and effective stress models, concerning the mechanisms that drive damage and lead to the stress state at full damage. Next, we discuss how the damage evolution law captures material's stress rate effect and alleviates the mesh sensitivity problem of local damage models.

3.3.3.1 Damage force and effective stress

Equations (3.5) and (3.8) determine under what strain (elastic stress) conditions damage initiates and how the effective stress evolves as D tends to unity. A common approach in continuum damage mechanics is to break the elastic stress tensor into its spectral positive and negative parts, and to express D_f and $\boldsymbol{\sigma}_{\text{eff}}$ as,

$$D_f(\boldsymbol{\sigma}) = D_f(\boldsymbol{\sigma}_+) \tag{3.9a}$$

$$\boldsymbol{\sigma}_{\text{eff}} = (1-D)\boldsymbol{\sigma}_+ + \boldsymbol{\sigma}_- \tag{3.9b}$$

We note that alternative expressions exist where instead of σ, the spectral decomposition of strain is considered [82, 66, 92, 87]; however, due to the use of $\boldsymbol{\sigma}$ in (3.5) and (3.8), the form (3.9) is preferred for the discussion in this section.

Rock fracture is often under compressive stress state. The shortcomings of (3.9) can be illustrated by referring to Fig. 3.1. First, as can be seen a large difference between the principal stresses σ_1 and σ_2 corresponds to a large enough shear stress τ that can initiate damage evolution; see for example the stress state A. However, if (3.9a) is used, D_f (and damage) remain zero, since $\boldsymbol{\sigma}_+ = \mathbf{0}$. Second, even if damage could evolve by an equation other than (3.9a), the stress would not degrade using (3.9b); that is, $\boldsymbol{\sigma}_{\text{eff}} = \boldsymbol{\sigma}_- = \boldsymbol{\sigma}$ at $D = 1$. In contrast, stress state A induces a $D_f = 0.5$; *cf.* (3.5). Moreover, D_f is sensitive to the hydrostatic stress. For example, for the same maximum shear τ and higher compressive σ_{ave}, no damage occurs for the stress state B. Finally, through damage evolution, $\boldsymbol{\sigma}_{\text{eff}}$ tends to the hydrostatic compressive stress $\langle \boldsymbol{\sigma}_h \rangle_-$ as $D \to 1$. This can be seen for stress state A and $D = 0.5$. In damage reaches unity, the effective stress state will correspond to the point σ_{ave} in the figure.

The two sets of equations for D_f and $\boldsymbol{\sigma}_{\text{eff}}$ predict a similar response for tensile dominant loading, *i.e.,* when $\sigma_{ave} > 0$; while there are some differences in the details of damage evolution, in both cases $\boldsymbol{\sigma}_{\text{eff}} \to \mathbf{0}$ as strain (proportionally) increases. There are, however, some differences in the failure damage state, $\boldsymbol{\sigma}_{\text{eff}}(D = 1)$, for pure shear and compressive dominant mixed loading ($\sigma_2 < 0 < \sigma_1$ and $|\sigma_2| > \sigma_1$). In short, the proposed damage model based on the Mohr-Coulomb failure criterion is more appropriate for rock fracture, especially when compressive mode failure is concerned.

3.3.3.2 Damage evolution: Rate effects and mesh sensitivity

Figure 3.4 compares strain stress responses for three different model and loading scenarios. The loading considered can correspond to any of the strengths in (3.4). The nondimensional scalar elastic stress, strain, and effective stress are defined as $\sigma' = \sigma/\underline{\sigma}$, $\epsilon' = \sigma' = C\epsilon/\underline{\sigma}$, and $\sigma'_{\text{eff}} = \sigma_{\text{eff}}/\underline{\sigma}$, respectively, where σ, ϵ, and σ_{eff} are the scalar elastic stress, strain, and effective stress. [1] These scalar values, $\underline{\sigma}$, and stiffness C correspond to a particular loading condition; for example for uniaxial tensile loading $\sigma = \sigma_{xx}$, $\epsilon = \epsilon_{xx}$, $\underline{\sigma} = \underline{s}_{\text{at}}$, (*cf.* (3.4b)). The

[1] Note that the scalar elastic stress measure σ in this section is different from the normal stress component in the Mohr-Coulomb criterion; *cf.* Fig. 3.1.

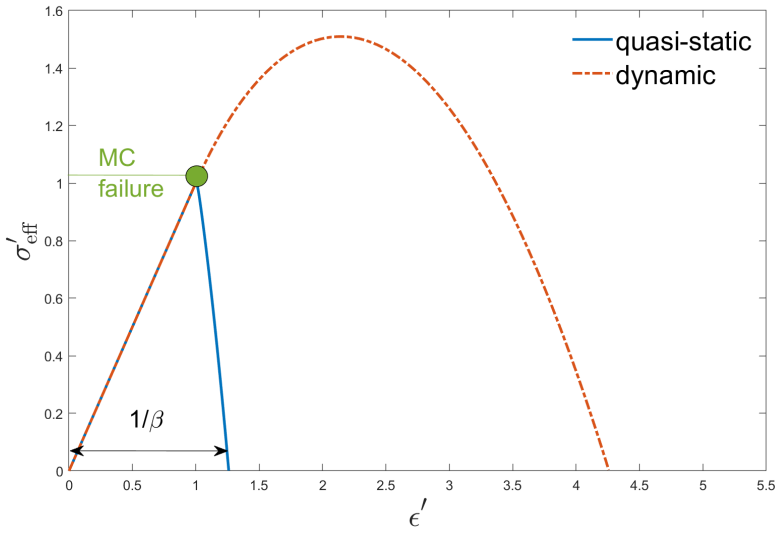

Figure 3.4: Sample quasi-static and dynamic strain versus stress responses.

corresponding stiffness is $C = E$ and $E/(1-\nu^2)$, for plane stress and plane strain conditions, respectively, where E and ν are the elastic modulus and Poisson ratio.

As loading (ϵ') increases, the scalar stress c increases until $c = \underline{c}$ in Fig. 3.2 for the given loading condition. This corresponds to $\epsilon' = 1$. For the MC model, material is deemed to fail instantaneously, for $\sigma'_{\text{eff}} = \sigma' = 1$. This sudden failure is shown by the green circle in the figure. The damage model regularizes the MC failure criterion. For the quasi-static loading $\dot{D} \approx 0$, thus $D \approx D_f$ throughout the loading. Given the linear dependence of D_f on c in (3.5), σ_{eff} linearly decreases from unity to zero as ϵ' increases from unity to $\bar{c}/\underline{c} = 1/\beta$. As, $\beta \to 1$ the response of the damage model tends to that of the un-regularized MC model, clarifying why β is called the brittleness factor. Regardless of the rate of loading for ϵ', $\dot{D}$ remains bounded by $1/\tau_c$; *cf.* (3.6). This results in a delayed damage response where D falls far behind its quasi-static limit D_f for higher rates of loading for ϵ'. This, in turn, increases the maximum effective stress, $\max(\sigma_{\text{eff}'})$, failure strain, $\epsilon'(D = 1)$, and toughness, *i.e.,* the area under the strain-stress curve. That is, the time-delay evolution law (3.6) can qualitatively model material's well-known stress rate effect. The dynamic solution in Fig. 3.4 corresponds to a nondimensional strain rate of 3. For lower and higher nondimensional

loading rates, the stress response gets closer to the quasi-static response and further expands, respectively.

If the quasi-static damage model $D = D_f$ where to be used, it would suffer the mesh-sensitivity problem of the early damage models. The introduction of an intrinsic length scale addresses this issue. The length scale l_d is either used in conjunction of added higher spatial order derivative terms in a local damage model [92, 42] or by nonlocal integration of certain fields, *e.g.,* strain, over neighborhoods of size l_d. However, both approaches are computationally expensive. The proposed damage model is much easier to implement, since it is simply an ODE in time. It also maintains the hyperbolicity of the elastodynamic problem which is critical for the solution of the coupled problem by the aSDG problem. Finally, the interaction of elastic wave speeds with the intrinsic time scale τ_c indirectly introduces a length scale l_d for the damage problem. While this length scale is not relevant for very low rate loading problems [78], at moderate to high loading rates it is expected to resolve the mesh sensitivity problem of local damage models.

3.3.4 aSDG method

The *asynchronous Spacetime Discontinuous Galerkin* (aSDG) method, formulated for elastodynamic problem in [7], is use for dynamic fracture analysis. The *Tent Pitching* algorithm [1] is used to advance the solution in time by continuous erection of *patches* of elements whose exterior patch boundaries satisfy a special causality constraint. This results in a local and asynchronous solution process. In addition, since spacetime is directly discretized by finite elements, the order of accuracy can be arbitrarily high both in space and time directions. This is in contrast to conventional finite element plus time marching algorithms where increasing the order of accuracy in time is not straightforward.

In addition to the displacement field for the elastodynamic problem, the damage field D is discretized in spacetime. The finite elements solve the weak form of elastodynamic balance laws, *cf.* §3.3.2, and the damage evolution equation (3.6), $\dot{D} - D_{\text{src}}(D, D_f) = 0$. Since the damage evolution is simply an ODE and maintains the hyperbolicity of the problem, the solution of the coupled elastodynamic-damage problem lends itself to the aSDG method. In addition, the satisfaction of balance laws per element for discontinuous Galerkin methods

results in a very accurate discrete solution of the damage evolution equation. We refer the reader to [20] for more details on the aSDG implementation of the problem, including the specification of jump conditions, and initial/boundary conditions for the damage evolution equation.

3.3.5 Realization of stochastic damage model parameters

As discussed in §2.2, incorporating material inhomogeneity is quite important to capture realistic failure response of quasi-brittle materials. The inhomogeneity is both in elastic and fracture properties. If an isotropic material model is assumed at the mesoscale, often only the elastic modulus is deemed to be a random field as in [48]. However, in general the entire elasticity tensor should be considered as a tensorial random field. However, often due to the higher effect that fracture properties have on macroscopic failure response, only they are considered to be random and inhomogeneous.

For a general fracture model, strength, energy, and initial damage state are the main model parameters. For the MC model, the friction angle ϕ (or friction coefficient k) and cohesion $\underline{c}$ are the model parameters used to determine c and D_f from (3.2) and (3.5), respectively. Cohesion is the parameter that is associated with fracture strength. The relaxation time τ_c in (3.6) and brittleness factor β determine the area under the strain-stress curve for different loading rates in Fig. 3.4. That is, they determine the fracture energy of the damage model. Finally, the initial condition for damage parameter, $D(\mathbf{x}, t = 0)$, corresponds to the initial state of material. In the present work, among strength, energy, and initial damage parameters, we consider inhomogeneity only in the strength property. This is in accord with a majority of similar studies in the literature such as [38, 123, 104, 75, 44, 14].

Accordingly, the only random field in the present study is cohesion $\underline{c}$. For a macroscopically homogeneous material, the point-wise and two-point statistics of the random field are spatially uniform. For the point-wise statistics, the mean and standard deviation of the random field are the main parameters. For the two-point statistics the form of the correlation function and the correlation length, *i.e.,* the length scale at which the field spatially varies are the main parameters. In [48], where the elastic modulus is considered to a random field, standard deviation and correlation length of the random field are considered

as the main parameters that impact fracture response. The realization of random fields for fracture strength and the subsequent fracture analysis becomes more expensive as the correlation length tends to zero. In [48] it is shown that certain macroscopic fracture statistics converge as the correlation length tends to zero. That is, by maintaining sufficient level of material inhomogeneity through using a small enough correlation length, accurate representation of macroscopic fracture response can be obtained.

We treat cohesion as a stationary random field with certain standard deviation ς_c and correlation length l_c. The statistics of this random field can be systematically obtained by using *Statistical Volume Elements* (SVEs), as shown in [14, 24]. However, for simplicity and better control on the effect of these parameters, we artificially manufacture random fields with certain ς_c and l_c. The distribution of $\underline{c}$ is assumed to follow a Lognormal(μ_c, ς_c) probability structure where μ_c and ς_c are the mean and standard deviation of the normal field. The corresponding mean and standard deviation of the log normal field for $\underline{c}$ are $M_c = \exp\left(\mu_c + \varsigma_c^2/2\right)$ and $\Sigma_c = \exp(\mu_c + \varsigma_c^2/2)\sqrt{\exp(\varsigma_c^2) - 1}$.

Once the underlying correlation function form and length, and point-wise *Probability Distribution Function* (PDF) are specified, there are a number of statistical methods to realize consistent random fields. We use the Karhunen-Loéve (KL) method [69, 77] to realize a random field $\xi = \xi(\mathbf{x}, \omega)$ by an expansion of its covariance kernel; the field is described by the series,

$$\xi(\mathbf{x}, \omega) = \mu_\xi(\mathbf{x}) + \sum_{i=1}^{\infty} \sqrt{\lambda_i} b_i(\mathbf{x}) Y_i(\omega), \tag{3.10}$$

where the denumerable set of eigenvalues λ_i and eigenfunctions $b_i(\mathbf{x})$ are obtained as solutions of the Fredholm equation, *i.e.,* the generalized eigenvalue problem (EVP), as detailed [55]. Since the eigenvalues monotonically decrease, the truncated series with an appropriate value of the upper limit n instead of ∞ in (3.10), can precisely represent the statics of the underlying random field. For practical use of the KL method, random variables Y_i should be statistically unrelated. This condition is automatically satisfied for Gaussian fields. Thus, we sample Gaussian random fields with the mean μ_c and standard deviation ς_c. To obtain the final random field for $\underline{c}$, we need to take the exponent of the realized Gaussian random field. There are some technical challenges for using two distinct grids for the aSDG finite

Table 3.1: Material properties for rock sample.

Properties	Units	Values
E	GPa	65
ρ	kg/m^3	2650
τ_c	µs	30
t_{ramp}	µs	10
ν	-	0.27
c	MPa	4.7
ϕ	$^\circ$	17
a	-	10

element solution in spacetime and the realized random field for $\underline{c}$ in a material grid. For more discussion on the use of KL method for fracture analysis and aSDG analysis of domains with random properties, we refer the reader to [40].

3.4 Numerical Results

We consider rock failure under dynamic compressive loading, and study the effect of mesh size, load amplitude, and material inhomogeneity on damage pattern. The geometry and loading description are shown in Fig. 3.5, where a rectangular domain of width $w = 0.08$ mm and height $l = 2w = 0.16$ mm is subject to compressive loading $P(t)$ on top and bottom faces. The traction $P(t)$ ramps up from zero to the sustained value of P_{peak} in ramp time t_{ramp}. Zero tangential traction is applied on these faces to model a frictionless loading interface. A traction free boundary condition is applied on the vertical sides of the domain. We assume a 2D plain-strain condition with material properties reported in table 3.1.

For this 2D problem, the spacetime mesh corresponds to a 2D $\times$ time grid of tetrahedron elements. The solution is advanced to the final time by an asynchronous patch-by-patch solution algorithm. The time increment of a pitched vertex is calculated based on the wave speed, spatial geometry, and sizes of elements around; *cf.* §3.3.4 and [1, 7] for more details. We use third order polynomial basis functions for damage and displacement fields in space and time.

As shown in Fig. 3.6, we use three different structured grids of 8×16, 16×32, and 32×64 squares, where each square is divided into two triangles. These are labeled as coarse,

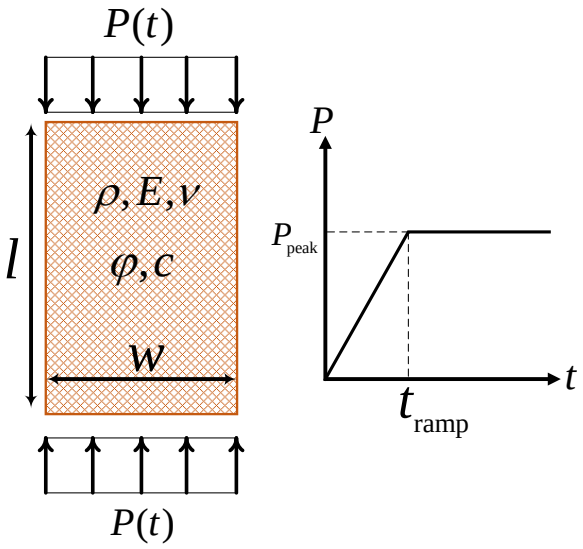

Figure 3.5: Problem description for a rectangle subject to a vertical compressive loading.

medium, and fine meshes, respectively. One of the numerical challenges in damage mechanics that affects the convergence of the *Newton-Raphson* method is the zero stiffness issue when damage is equal to unity. One way to avoid this problem is multiplying the damage value used in (3.8) by a positive reduction factor less than unity. Herein, we select a reduction factor of 93%.

3.4.1 Homogeneous material

3.4.1.1 Mesh sensitivity

The dependence of damage response on the resolution of the underlying discrete grid is a well-known problem for non-regularized continuum damage models. As described in §3.3.3.2, the proposed time-delay damage model introduces an inherent length scale proportional to the relaxation time and longitudinal elastic wave speed, *i.e.*, $l_d \propto c_\mathrm{d}\tau_c$. To show mesh-objectivity of the results, we compare the damage evolution for coarse and medium meshes in Fig. 3.7. For this numerical example, material properties are homogeneous and listed in table 3.1, and the loading magnitude is $P_\mathrm{peak} = 13.5$ MPa.

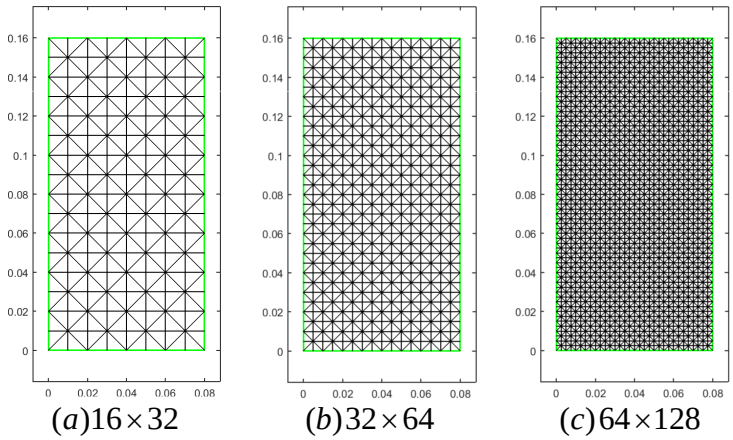

Figure 3.6: Initial meshes used for the simulations: (a) Coarse; (b) Medium; (c) Fine.

Figure 3.7 shows an excellent agreement between the solutions of the two meshes at early and evolved stages of damage evolution. We also refer the reader to [20] for a more detailed study of mesh objectivity for a tensile fracture problem where damage localization zone converges to a region of finite width. We reiterate that the time-delay formulation addresses the mesh-objectivity problem with much less computational difficulty than the non-local integration-based and gradient-based damage models. Moreover, it does not violate the hyperbolicity of the problem. This facilitates the use of the aSDG method and is consistent with the physical observation that damage propagates with a finite speed [59].

3.4.1.2 The effect of load amplitude

In the previous example, the stress level was sufficiently high to initiate damage near the loading edges, from the early stages of the solution. The stress state in the middle of top and bottom faces is approximately similar to bi-axial compressive condition; material tends to expand in the horizontal direction because of the Poisson effect while the surrounding material prevents its deformation. However, the stress state around the corners is close to an unconfined uni-axial compressive condition because of the stress-free conditions at left and right boundaries. The higher differences between compressive stresses in the Mohr circle results in a higher value for c; *cf.* (3.2). Thus according to the MC failure criterion, the corner zones are more susceptible to an earlier time for damage initiation and higher damage values.

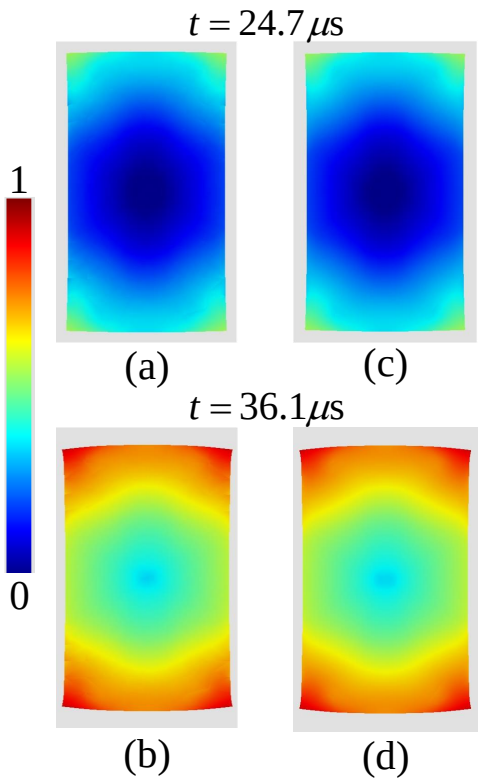

Figure 3.7: Damage responses at different times for two different meshes. Figures (a) and (b) correspond to the coarse mesh and figures (c) and (d) correspond to the medium mesh. The results are shown on the deformed mesh with a magnification factor of 300.

This is verified by the higher damage values around the corners in Fig. 3.7(a-b). After the initiation of damage at corners, damage diffuses towards the middle of the domain.

To study the effect of load amplitude, we reduce the peak stress such that damage initiates in the middle of the domain. The vertical normal stress magnitude roughly doubles across the entire width when the stress waves collide in the middle of the domain. The load for this problem is chosen such that it is not large enough to initiate damage when the stress wave enters from the top and bottom edges, but is sufficient to cause damage in the middle of domain due to the doubling effect. We call this condition the low amplitude case, corresponding to $P_{\text{peak}} = 6$ MPa, and refer to the previous peak stress problem as the high amplitude case. As shown in Fig. 3.8(a), the initial damage occurs when the peak stress reaches the middle of the domain; *i.e.,* at $t_{\text{collision}} \approx t_{\text{ramp}} + \frac{l}{2c_d} \approx 24\mu$s which is well predicted by the numerical result. After the collision, the magnified reflected waves are sufficiently high

to overcome the cohesion of rock. Thereafter, damage diffuses toward boundaries where the waves are propagating to; see Fig. 3.8 (b-d). This failure mechanism is completely different from that of the high amplitude case where the damage initiates in a shear dominated regime at the corners. Therefore, load amplitude has a significant impact on damage pattern and failure mechanism. For a better comparison, we provide the damage response at various times for the high amplitude case in Fig. 3.9.

3.4.2 Heterogeneous material

As detailed in §3.3.5, for the analysis of inhomogeneous rock masses, we assume that cohesion is a random field. This analysis expands our preliminary comparison of the response of homogeneous and heterogeneous rock in [22]. We construct four random fields using the *KL* method with the mean cohesion value of $M_c = 4.7$ MPa, similar to the spatially uniform $\underline{c}$ used in the preceding examples for homogeneous rock. The standard deviation is set to $\Sigma_c = 2.35$ MPa. The correlation lengths of $l_c = 5$ mm, 10 mm, 20 mm, and 40 mm are used, where for each correlation length one random field realization is generated by the KL method. These random fields are shown in Fig. 3.10. A smaller correlation length indicates faster variations in cohesion from one spatial point to another, so it corresponds to a more locally heterogeneous field. These random fields are constructed with the first 2000 terms of the KL series. For the following results, we use the fine mesh to have an adequate resolution for capturing the underlying inhomogeneity.

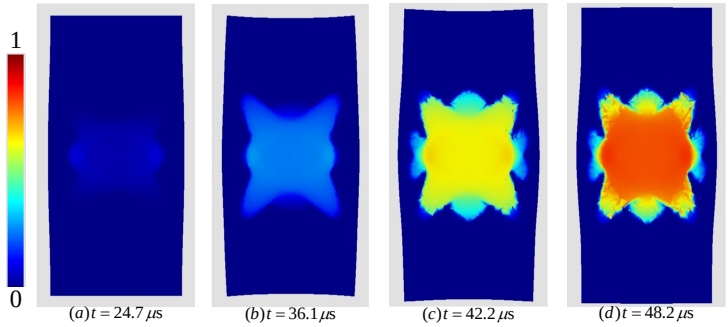

Figure 3.8: Damage evolution at various times for the medium mesh and low amplitude load. The results are shown on the deformed meshes with a magnification factor of 1000.

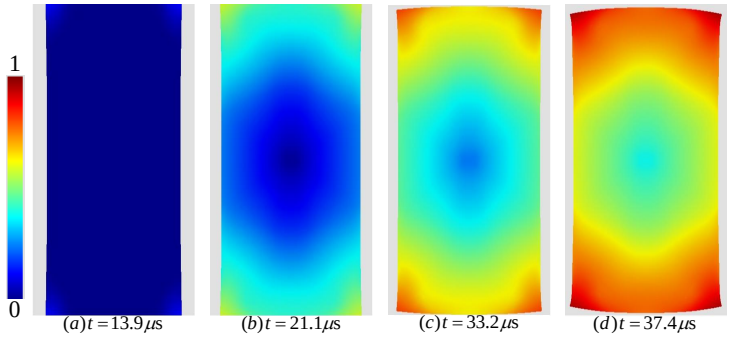

Figure 3.9: Damage evolution at various times for the medium mesh and high amplitude load. The results are shown on the deformed meshes with a magnification factor of 300.

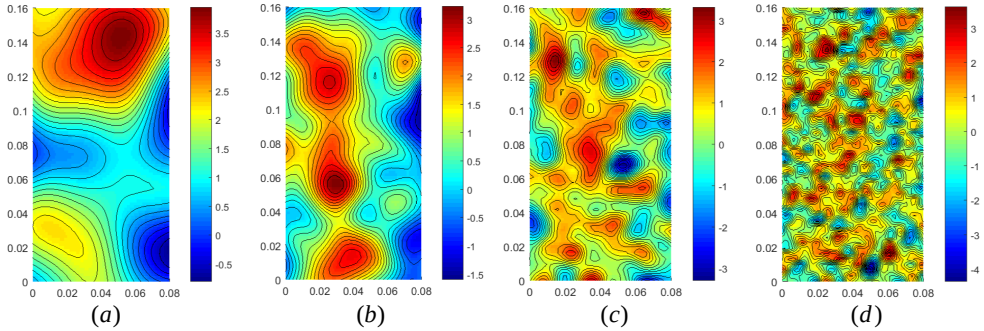

Figure 3.10: Random field realizations for cohesion with different correlation lengths, l_c, equal to: (a) 5 mm, (b) 10 mm, (c) 20 mm, and (d) 40 mm.

3.4.2.1 Low amplitude load

In this section, we study the effect of heterogeneity on damage response for the low amplitude condition. Figure 3.11 shows the damage response for $l_c = 40$ mm at various times. From the cohesion map in Fig. 3.10(a), we observe that $\underline{c}$ varies very slowly in space. It takes the highest values near the top boundary and the lowest ones at three spots close to the left and right boundaries; weak zones are colored by blue. In Fig. 3.8(a), the initial damage zone begins when the stress waves collide in the middle of the domain. The particular form of this realization for $\underline{c}$ actually favors damage accumulation in the center, given that a higher strength zone is near the top boundary in Fig. 3.10(a). As shown in 3.11, damage initiates and accumulates both in this center location and in the three aforementioned weak sites close to the boundaries. Thus, the form of the failure pattern follows both the weak points

in the material and locations with higher stress values in general. By comparison of Fig. 3.8 and Fig. 3.11, we also observe that the earlier initiation of damage in weaker sites results in a response with more concentrated damage zones. Finally, the damage initiation time is almost the same as that for the homogeneous rock, and in both cases it is right after the collision of the waves at $t_{\text{collision}} \approx 24$.

Figures 3.12-3.14 show the damage evolution for heterogeneous cohesion fields with correlation lengths equal to 20 mm, 10 mm, and 5 mm, respectively. According to 3.12(a)-3.14(a), the time for damage initiation decreases as the correlation length gets smaller, *i.e.,* when the heterogeneity is increasing.

It is well accepted in the literature that one of the main reasons for localization and softening behavior in brittle materials is their heterogeneous structure at microscale [28, 27, 121]; the weaker points in material begin to fail earlier. This results in an increased stress concentration in the damaging zones and the shielding of the surrounding areas. That is, the inhomogeneity in material properties promotes inhomogeneity and localization in the stress field. Unlike ductile materials, there are not much energy dissipative reserves, for example from plasticity, to balance the stress field. Figures 3.11(d)-3.14(d) reveal a crucial impact of the correlation length on failure mechanism; this is a transition from diffusive damage propagation to a more localized response as the correlation length gets smaller. This agrees with the preceding discussion on the promotion of damage localization by material inhomogeneity. In fact, for the solutions with the lowest correlation length, even the mode and propagation of failure is significantly different than that of a homogenous material; in Fig. 3.8(d) and Fig. 3.14(d), the effect of the weakest point of the material is high to an extent that damage initiates and accumulates in a more distributed sense, as opposed to the damage accumulation in the central zone in Fig. 3.8.

3.4.2.2 High amplitude load

Figures 3.15-3.18 show the evolution of the damage field for correlation lengths $l_c = 40$ mm to $l_c = 5$ mm. We observe a very good match between damage localization sites and the locations of material weak points in Fig. 3.10(b-d). Moreover, as we decrease the correlation length, the time of damage initiation decreases; *cf.* figs. 3.15(a)-3.18(a)).

From the final damage pattern in Fig. 3.9(d) for the homogeneous domain, one observes that for high amplitude loading extensive damage is experienced almost everywhere, especially close to the top and bottom boundaries. There is little resemblance between this solution and those for high correlation random fields in Fig. 3.15(d) and Fig. 3.16(d). Similarly for the low amplitude load, high differences are observed between the solutions of homogeneous, Fig. 3.8(d), and inhomogeneous domains with high correlation lengths, Fig. 3.11(d) and Fig. 3.12(d). This is due to the fact that for such large correlation lengths, the large islands of low strength greatly impact the response.

In contrast, as the correlation length decreases, the overall material properties are almost the same in all areas, except the inhomogeneities that are observed at smaller length scales. Consequently, in comparison of damage patterns for the homogeneous rock in Fig. 3.9(d) and rocks with small correlation length for $\underline{c}$ in Fig. 3.17(d) and Fig. 3.18(d), a very similar overall response is observed; in all cases, damage is widespread in the domain, with the top and bottom sides experiencing the highest damage. In contrast, there is no resemblance between the damage patterns of homogeneous domain in Fig. 3.8(d) and those for low correlation length fields in Fig. 3.13(d) and Fig. 3.14(d). The reason is that for this low amplitude of load, damage can only accumulate in the center of the homogeneous domain, whereas for inhomogeneous domains damage can accumulate from weak points outside of this zone; this greatly affect the final damage pattern.

The statistical continuum damage model enhances the accuracy of conventional continuum damage models, and its solutions are more consistent with sharp interface fracture models. The reason are as follows. First, damage initiation zones from material weak points are more concentrated and better resemble crack nucleation events. Second, damaged zones tend to propagate in crack-like features with specific inclined directions rather than the diffuse response around the initiation points. For example, in Fig. 3.18(d), many localized zones resemble cracks at 45 degree and steeper relative to the vertical direction. This features qualitatively match other numerical and experimental observations [112, 113, 76, 49, 100]. Specifically, based on the MC failure criterion, cracks are formed at angles $\pm(45^\circ + \phi/2)$ with respect to the compressive loading direction. This example demonstrates that a damage model based on uniform material properties not only misses crack-like damage localization

features, but can also incorrectly predict the location of zones with the maximum overall damage accumulation (low load example).

3.4.2.3 Mesh sensitivity

The mesh sensitivity of diffusive damage response for the sample with homogeneous properties was presented in §3.4.1.1. Here, we study the effect of mesh size for domains with heterogeneous cohesion that result in a localized damage response. Figure 3.19 compares damage responses for the domain with $l_c = 40$ mm at $t = 43$ μs. The results are presented for different load amplitudes and mesh sizes. The same results are presented in Fig. 3.20 for the smallest correlation length $l_c = 5$ mm at $t = 36$ μs. While, there is a good agreement between the results obtained by medium and coarse meshes for both load conditions, the solutions for the largest correlation length in Fig. 3.19 show a better agreement. This is due to the fact that the details of the solution are at the scale of the correlation length; thus, as smaller correlation lengths are used for material properties, finer finite elements should be used to accurately capture the details of the solution.

3.5 Conclusions

We presented a dynamic bulk damage model, based on the time-delay evolution law in [19]. The relaxation time τ_c indirectly introduces an intrinsic length scale for dynamic fracture problems. This resolves the mesh sensitivity problem of early local damage models. Moreover, by limiting the maximum damage rate, the model qualitatively captures stress rate effect, in that, both strength and toughness increase when the loading rate increases. The ODE form of the evolution model greatly simplifies the implementation of the damage model and maintains the hyperbolicity of the elastodynamic problem.

The coupled elastodynamic-damage problem was implemented by the aSDG method to solve a uniaxial compressive fracture problem for rock. The MC model is used to formulate a damage force model. In the process of damage accumulation, the effective stress tends from the initial elastic limit at $D = 0$ to its hydrostatic compressive value at $D = 1$. The MC model also captures rock strengthening effect as hydrostatic pressure increases. In contrast,

damage models that are based on spectral positive and negative decomposition of strain (or stress) tensor, fail to model failure under compressive response.

To model the effect of material inhomogeneity, cohesion was assumed to be a random field. Two different macroscopic compressive load amplitudes were used for this study. For a homogeneous material, the higher load amplitude initiates damage as the compressive wave enters the domain, whereas for the lower load damage initiates only in the center of the domain where stress doubling effect occurs upon the intersection of compressive waves. Four lognormal fields with different correlation lengths l_c were generated for $\underline{c}$. It was shown that inhomogeneity could significantly alter the failure response of an otherwise homogeneous rock. For example, for the higher load amplitude, unlike the homogeneous case, damage initiates in the center of the domain. This is due to the particular form of the realized random field where a large zone of low $\underline{c}$ is sampled in the center of the domain. Moreover, for the lower load amplitude damage can initiate everywhere in the domain as the waves travel toward the center of the domain. This is due to the weaker sampled $\underline{c}$ at these locations, which does not require the stress wave doubling effect to initiate damage. Moreover, even the zones that eventually accumulate the highest damage can be significantly different between models with homogeneous and inhomogeneous properties, even as the correlation length tends to zero (low load amplitude example).

Another problem of using a homogeneous material model is the inability or difficulty of bulk damage models to capture sharp localization zones. In contrast, as lower correlation lengths were used for inhomogeneous domains, the fracture pattern became more realistic and resembled the results that are obtained by more accurate sharp interface models [3]. In particular, the MC model predicts fractures at $\pm(45 + \phi/2)$ degree angles with respect to the compressive load direction. For the lowest correlation lengths, localized damage zones with angles roughly in the range ± 45 to $\pm(45 + \phi/2)$ are observed. These features are better resolved with the higher resolution finite element mesh, confirming that finer meshes are required for the solution of problems with more rapid variation of material properties.

There are several extensions to the present work. First, the form of effective stress (3.8) implies that friction coefficient is zero at complete damage ($D = 1$), whereas jointed (damaged) rock may still possess some residual friction coefficient. This will enhance the

angle of localized regions in Fig. 3.18(d). Second, MC criterion is not appropriate for rock tensile fracture analysis and the damage force can be formulated by Hoek-Brown [62] and other more accurate models. Third, as shown in [2], rock anisotropy, for example induced by the existence of bedding planes, can affect fracture angle under compressive loading. Anisotropic failure criteria such as those in [96, 74] can be used to formulate the damage force. Finally, mesh adaptive operations in spacetime [8] can drastically reduce the computational cost of the formulated aSDG method for this bulk damage model.

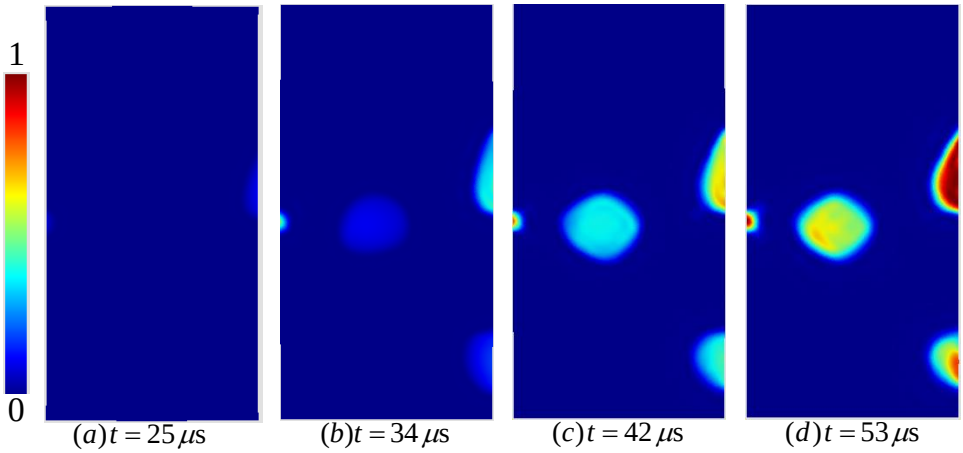

Figure 3.11: The evolution of damage field for the low amplitude load and cohesion realization with $l_c = 40$ mm.

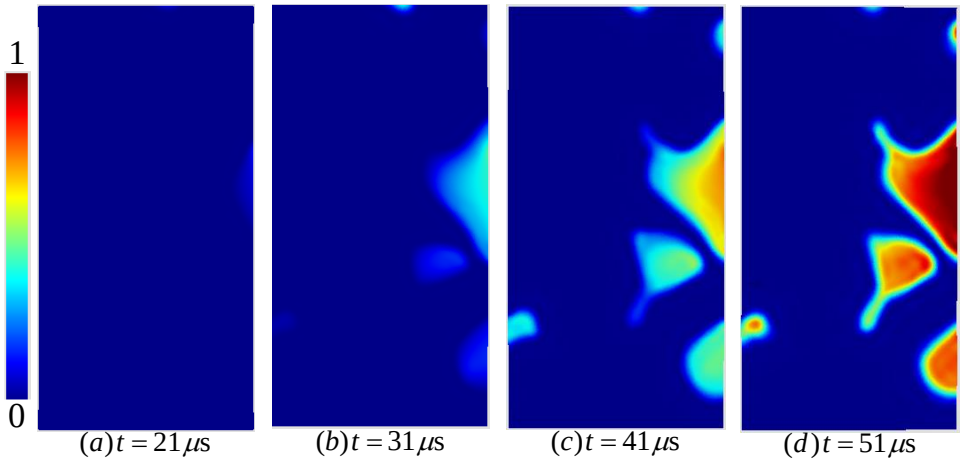

Figure 3.12: The evolution of damage field for the low amplitude load and cohesion realization with $l_c = 20$ mm.

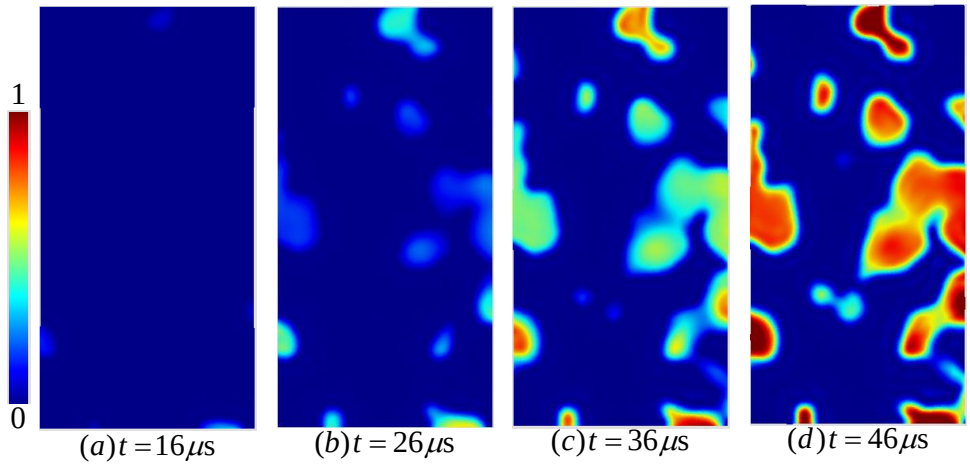

Figure 3.13: The evolution of damage field for the low amplitude load and cohesion realization with $l_c = 10$ mm.

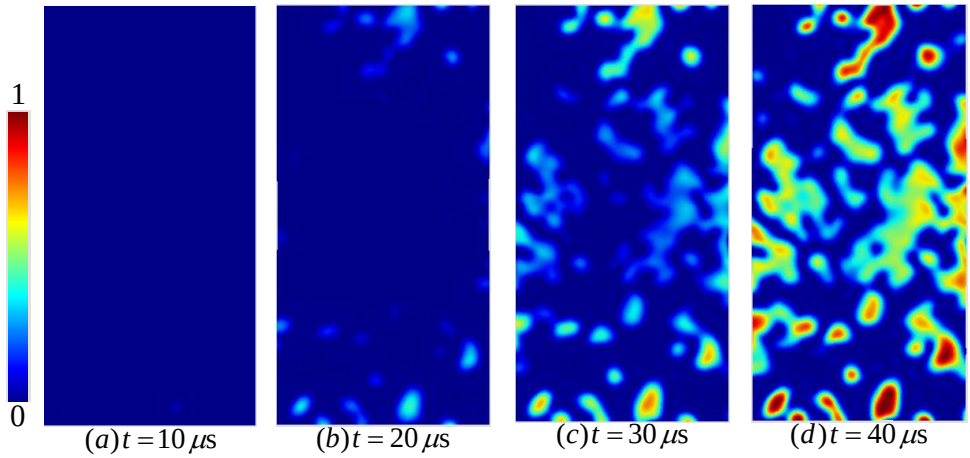

Figure 3.14: The evolution of damage field for the low amplitude load and cohesion realization with $l_c = 5$ mm.

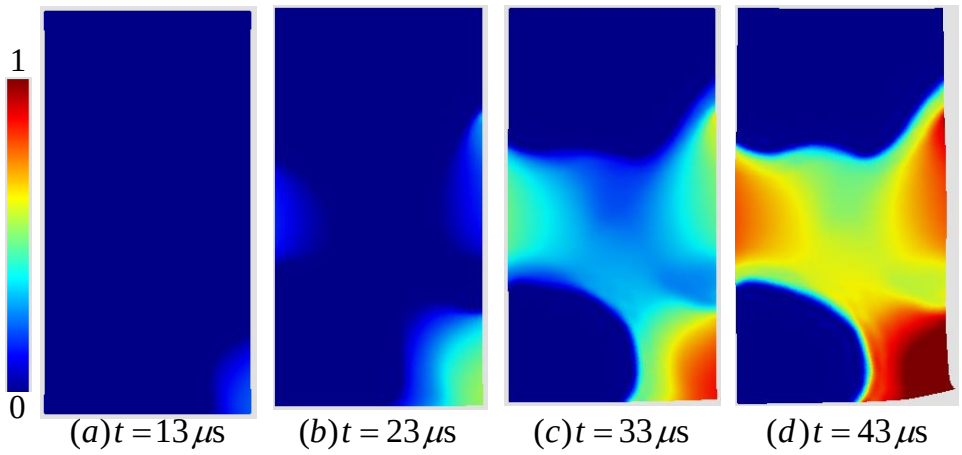

Figure 3.15: The evolution of damage field for the high amplitude load and cohesion realization with $l_c = 40$ mm. The results are shown on the deformed mesh with a magnification factor of 100.

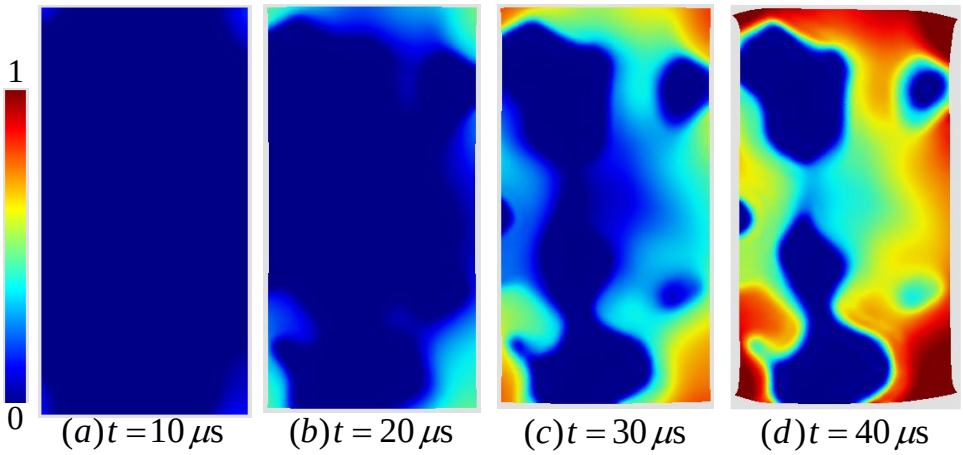

Figure 3.16: The evolution of damage field for the high amplitude load and cohesion realization with $l_c = 20$ mm. The results are shown on the deformed mesh with a magnification factor of 100.

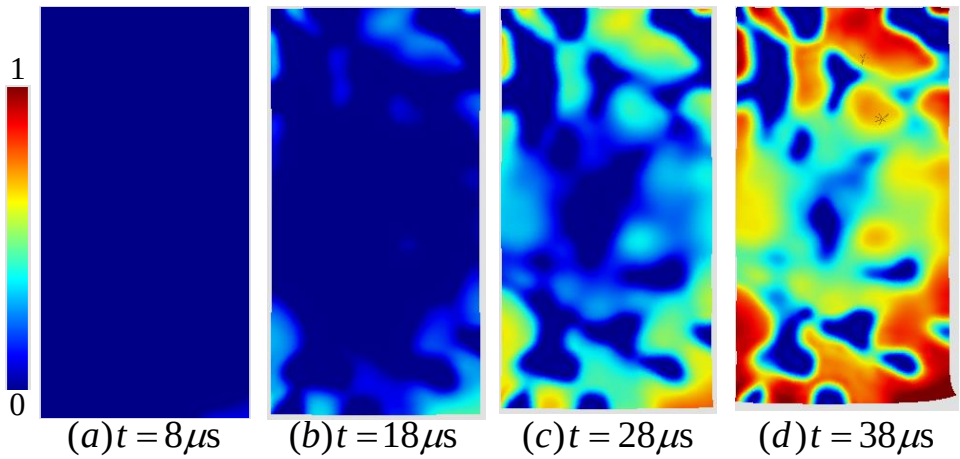

Figure 3.17: The evolution of damage field for the high amplitude load and cohesion realization with $l_c = 10$ mm. The results are shown on the deformed mesh with a magnification factor of 100.

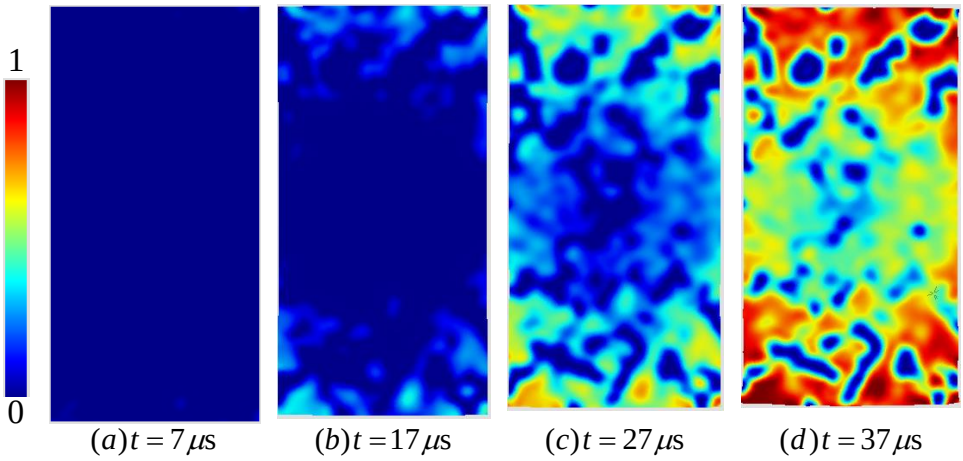

Figure 3.18: The evolution of damage field for the high amplitude load and cohesion realization with $l_c = 5$ mm. The results are shown on the deformed mesh with a magnification factor of 100.

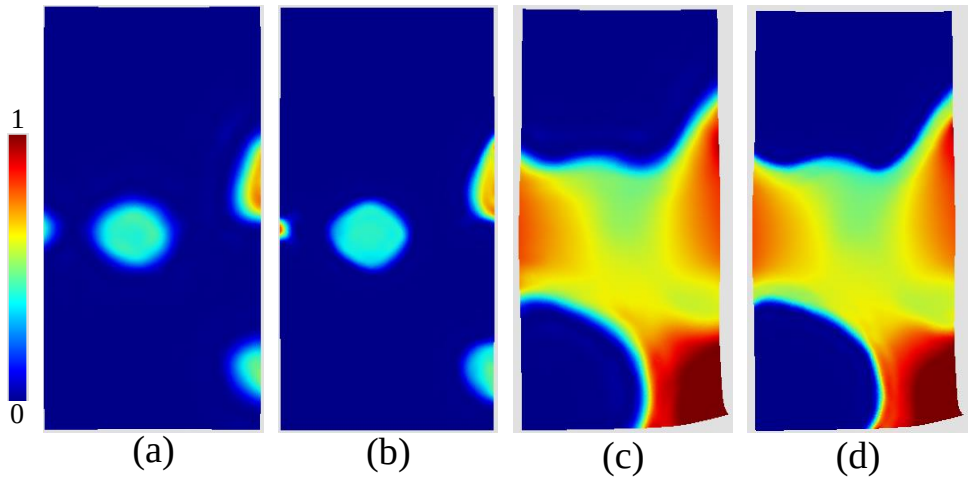

Figure 3.19: Damage responses at $t = 43$ μs for the domain with $l_c = 40$ mm with different meshes and load amplitudes: (a) low amplitude-medium mesh, (b) low amplitude-fine mesh, (c) high amplitude-medium mesh, and (c) high amplitude-fine mesh.

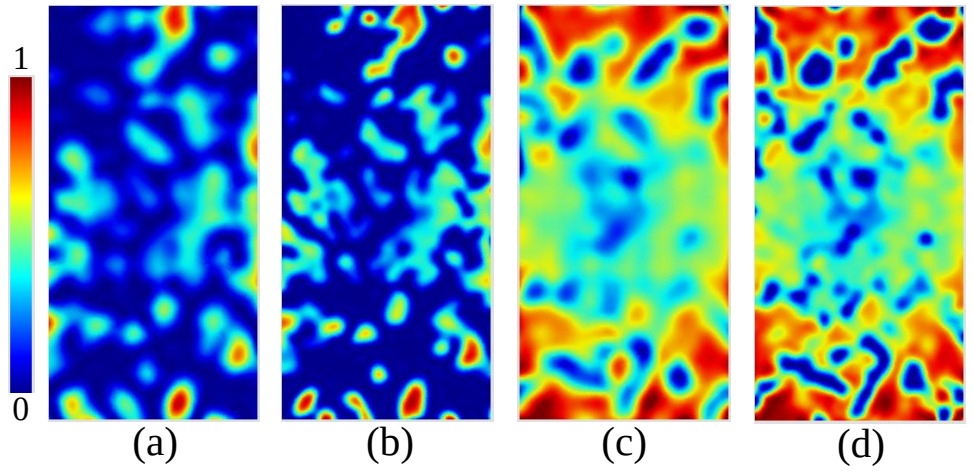

Figure 3.20: Damage responses at $t = 36$ μs for the domain with $l_c = 5$ mm with different meshes and load amplitudes: (a) low amplitude-medium mesh, (b) low amplitude-fine mesh, (c) high amplitude-medium mesh, and (c) high amplitude-fine mesh.

Chapter 4

Comparison of interfacial and continuum models for dynamic fragmentation analysis

This chapter is revised based on the following published papers:

B. Bahmani, R. Abedi, P.L. Clarke, "Comparison of interfacial and continuum models for dynamic fragmentation analysis", ASME 2018 International Mechanical Engineering Congress and Exposition (IMECE), Pittsburgh, PA (2018).

B. Bahmani, R. Abedi, P.L. Clarke, "A bulk damage model for modeling dynamic fracture in rock", Proceeding 52th U.S. Rock Mechanics/Geomechanics Symposium (ARMA), Seattle, WA (2018).

Following the previous chapters, my primary contributions in this chapter can be listed as (i) comparison of a previously developed interfacial damage model with my continuum damage model for dynamic fragmentation problems, (ii) arrangement and interpretation of numerical examples, and (iii) preparation of the first draft.

4.1 Abstract

The microstructural design has an essential effect on the fracture response of brittle materials. We present a stochastic bulk damage formulation to model dynamic brittle fracture. This model is compared with a similar interfacial model for homogeneous and heterogeneous materials. The damage models are rate-dependent, and the corresponding damage evolution includes delay effects. The delay effect provides mesh objectivity with much less computational efforts. A stochastic field is defined for material cohesion and fracture strength to involve microstructure effects in the proposed formulations. The statistical fields are constructed through the Karhunen-Loeve (KL) method. An advanced asynchronous Spacetime Discontinuous Galerkin (aSDG) method is used to discretize the final system of coupled equations. Application of the presented formulation is shown through dynamic fracture simulation of rock under a uniaxial compressive load. The final results show that a stochastic bulk damage model produces more realistic results in comparison with a homogenizes model.

4.2 Introduction

Brittle materials have a wide range of applications in various areas–from the geological application, such as rock, to biological applications, such as bone. The failure response of this kind of material is susceptible to a sudden rupture by initiation, propagation, and fragmentation of many cracks. The main reason of such a brittle rupture derives from the complex microstructure of these materials which consist of many microdefects and microcracks. The most challenging task in the numerical analysis of brittle materials is the modeling of fracture behavior. In the context of conventional continuum mechanics, there exist two frameworks for fracture modeling; *Interfacial* and *Bulk* models.

Interfacial models represent explicit sharp fractures in the computational domain. Three main models in this context are: the *linear elastic fracture mechanics* (LEFM) model, cohesive models [51, 25], and interfacial damage models [19, 16, 90, 89, 6]. Interfacial models explicitly track the real pattern of fractures, but their implementation is cumbersome and their computational cost is high. In applications such as multiscale methods, it is hard to track explicit discontinuities in all scales of interest. If it is even possible, the computation cost will be extremely high. However, the most important issue of these models is the need for additional criteria to predict the initiation and propagation direction of fractures.

Bulk models apply continuum damage mechanics to approximate the presence of explicit fractures with an implicit damage variable indicated the level of failure in an equivalent continuum domain. One of the earliest studies in this area refers to *Smeared Crack* approach in [30] where a continuum model is presented to simulate fractures in concrete. *Phase Field* approaches are the enhanced alternatives for bulk models[53, 35, 84, 34, 71]. Bulk models remedy the issues above in regard to fracture initiation, additional criteria for propagation direction, and challenges in fragmentation in interfacial models. Also, they provide several benefits from numerical aspects: Simple integration with other numerical methods, fast implementation, and straightforward utilization in multiscale analysis. The main drawback of bulk models is the overestimation of fracture sharpness which is much better handled by phase field approaches.

The effect of the microstructure is one of the important aspects of fracture response in quasi-brittle material. Al-Ostaz and Jasiuk [15] observed different fracture patterns in different samples with the same set-ups. The reason for this stochastic behavior is the high sensitivity of quasi-brittle materials to their microstructure defects. Similar observations are reported in [72], especially for responses after ultimate load capacity of the material when fractures are initiated and propagated. Another consequence of the high sensitivity of responses to microstructure is the *size effect* [102, 54]. One of the widely accepted models for studying the size effect is the Weibull's weakest link model. The efficiency of the Weibull method in capturing the size effect and statistical variation of fracture strength in interfacial models is shown in [118, 119]. We have used the Weibull model in the context of an interfacial damage model to capture statistical fracture response of rock, in hydraulic fracturing [11], fracture under dynamic compressive loading [3], and in fragmentation studies [6, 41]. However, these models are computationally expensive due to the use of a sharp interfacial model. In this study, we first use a random field approach, rather than the Weibull model, to represent material randomness. Second, in addition to a sharp damage model, we formulate a bulk damage model, where material cohesion is treated as a random field.

We will incorporate microstructural randomness in dynamic failure of brittle material through a stochastic approach. In the proposed stochastic approach, model parameters are constructed based on statistical fields. In the current study, we generate a realization of the statistical field for the fracture strength and material cohesion based on the well-known *Karhunen-Loève* (KL) method [69, 77]. In this regard, a recent study in [12] demonstrates the motivation of statistical models in high rates of loading in that the entire spatial domain fails in a short time period for problems that lack macroscopic stress concentration points.

The statistical damage formulation is coupled with elastodynamic equations for both the bulk and interfacial models. To solve these nonlinear systems of hyperbolic equations, we employ the *asynchronous Spacetime Discontinuous Galerkin* (aSDG) method; this method uses the Tent-Pitcher algorithm [1] to advance the solution by solving one patch (a small collection of elements) at a time until the computational spacetime domain is completely

solved. This method results in a highly advanced numerical method with local and linear solution properties for the elastodynamic problem [7].

In the following sections, we will describe the proposed damage models, interfacial and bulk, and KL method in §4.3. We will show the effect of randomness and accuracy of the stochastic bulk model in §4.4 for a compressive sample to indicate the essential role of randomness in dynamics fracture analysis. Finally, we will discuss the novel contributions of this study in §4.5.

4.3 Formulation

In this section, we describe two different approaches for the modeling of brittle material failure. These approaches have the same origin from mathematical and physical aspects, but one represents the material failure as a localized/sharp phenomenon, and the other considers the failure mechanism as a bulk process in the material. After the description of the models, we will discuss a general method based on the KL method to involve stochastic effects into the introduced damage models.

Interfacial model

The interfacial damage parameter D interpolated between the fully bonded ($D = 0$) to fully-debonded ($D = 1$) state on a contact/fracture interface. The macroscopic traction vector, $\mathbf{s}^*$, is given by,

$$\mathbf{s}^* = (1 - D)\breve{\mathbf{s}}_B + D\breve{\mathbf{s}}_D \tag{4.1}$$

where $\breve{\mathbf{s}}_B$ and $\breve{\mathbf{s}}_D$ are dynamic Riemann solutions for bonded and debonded (separation, contact–stick, or contact–slip) modes. The formulas for these four states of Riemann solution are provided in [4]. The damage value is obtained by the evolution law,

$$\tau_c \dot{D} = D_{\text{src}}, \tag{4.2a}$$

$$D_{\text{src}} = 1 - e^{-a\langle D_{\text{frc}} - D\rangle_+}, \tag{4.2b}$$

$$D_{\text{frc}} = g(\breve{s}, \breve{\delta}), \tag{4.2c}$$

where $\dot{D}$ is the time derivative of D, τ_c is the time-scale or delay parameter, a is the brittleness factor, and $\langle . \rangle$ is the Macaulay positive operator. Similar to [12] we assume the damage evolution be driven by an effective stress $\breve{s}$ and an effective separation $\breve{\delta}$. In earlier works, *e.g.,* [6], damage is only driven by the effective traction, but as described in [12] the inclusion of $\breve{\delta}$ is not only physically motivated but also improves the response of the model. Their definitions are motivated by the definition of effective scalar values in [37] and are given by,

$$\breve{s} := \sqrt{\langle \breve{s}^1_{\mathrm{B}} \rangle^2 + \beta_s^2 (\breve{s}^2_{\mathrm{B}})^2} \tag{4.3a}$$

$$\breve{\delta} := \sqrt{\langle \delta_1 \rangle^2 + \beta_\delta^2 \delta_2^2} \tag{4.3b}$$

where β_s and β_δ are traction and displacement mode-mixity coefficients, and $(\breve{s}^1_{\mathrm{B}}, \breve{s}^2_{\mathrm{B}})$ and (δ_1, δ_2) are the normal and tangential components of bonded Riemann traction $\breve{\mathbf{s}}_B$ and displacement jump (separation) vectors in 2D, respectively. The form of the function $g(\breve{s}, \breve{\delta})$ in Eqn. (4.2c) and the mode-mixity values for a Mohr-Coulomb model are provided in [12] and [3], respectively. The reader is also referred to [6] for a general discussion on this class of interfacial damage models and their comparison with conventional cohesive models.

Bulk model

We use the same damage evolution law for the bulk model to provide a better comparison between the two models. The bulk model used in the current study is a nonlinear ordinary differential equation as,

$$\tau_c \dot{\kappa} = \kappa_{\mathrm{src}}, \tag{4.4a}$$

$$\kappa_{\mathrm{src}} = 1 - e^{-a\langle \kappa_{\mathrm{frc}} - \kappa \rangle_+}, \tag{4.4b}$$

$$\kappa_{\mathrm{frc}} = \frac{\sigma_r + \sigma_{\mathrm{ave}} \sin\phi}{c \cos\phi}, \tag{4.4c}$$

where $\dot{\kappa}$ is the time derivative of the damage variable κ, $0 \leq \kappa \leq 1$, c is the material cohesion, and ϕ is the friction angle. σ_{ave} and σ_r are the center and radius of the Mohr circle in the

stress space, respectively. We define the damage force function, *i.e.,* κ_{frc}, based on the Mohr-Coulomb failure envelope. This definition is appropriate for brittle material with dominant failure modes in shear and tensile modes.

The proposed dynamics damage formulation, which is based on the Allix's formulation in [17, 43, 19], introduces a delay behavior into the damage mechanism through the time-scale parameter. The differences of our model and the Allix's formulation, particularly in relation to the definition of damage force Eqn. (4.4c) based on the Mohr-Coulomb failure criterion are further discussed in [23]. The delay effect of our model accounts for the non-instantaneous damage mechanism which is more consistent with the physical behavior of damage response in dynamic conditions. Also, the timescale τ_c preserves the mesh-objectivity of the aforementioned damage formulation by providing a non-local behavior in spacetime domain. This (temporal) non-local behavior and existence of an intrinsic length scale is required for bulk damage models [93] and is comparable with the spatial non-local characteristics in conventional gradient-based [91, 114, 73] and integration-based non-local [97] theories where they use a length-scale parameter. However, the delay method is preferable to those spatially non-local schemes due to its much less computational and implementation efforts.

We propose a damage-deformation relation by considering the effect of damage on deviatoric and hydrostatic tensile components of the elastic stress tensor as,

$$\boldsymbol{\sigma}_{\text{eff}} = (1-\kappa)(\boldsymbol{\sigma}_d + \langle \boldsymbol{\sigma}_h \rangle) + (\boldsymbol{\sigma}_h - \langle \boldsymbol{\sigma}_h \rangle), \tag{4.5}$$

where $\boldsymbol{\sigma}_d$ and $\boldsymbol{\sigma}_h$ are deviatoric and hydrostatic parts of elastic stress tensor $\boldsymbol{\sigma}$.

Stochastic field realization

The uncertainty of a material property ξ is incorporated in the proposed damage models, bulk and interfacial, by treating a fracture strength parameter ξ as a spatially inhomogeneous random field $\xi(\mathbf{x}, \omega)$ governed by probability structure ω. The random field is developed by the imposition of a desired stationary covariance of γ-*exponential* form with a prescribed correlation length which controls the spatial variability of the field. A log-normal

Lognormal(μ, σ^2) probability structure governs the distribution of the random field. This probability space has the mean $\exp\left(\mu + \sigma^2/2\right)$ and variance $[\exp(\sigma^2) - 1]\exp(2\mu + \sigma^2)$ of the log-normal field.

There exist several methods that allow a scalar random field approximation to be generated wherein the inherent statistics are preserved. One such method is the KL method which approximates the random field ξ by an expansion of its covariance kernel as the following series,

$$\xi(\mathbf{x}, \omega) = \mu_\xi(\mathbf{x}) + \sum_{i=1}^{n} \sqrt{\lambda_i} b_i(\mathbf{x}) Y_i(\omega), \tag{4.6}$$

where the eigenvalues λ_i and eigenfunctions $b_i(\mathbf{x})$ are extracted as solutions of the Fredholm equation, *i.e.,* the generalized eigenvalue problem (EVP), which is detailed in [55]. The truncated series with an appropriately chosen n number of terms can precisely represent the statics of the underlying random field, due to the monotonically decreasing property of the eigenvalue solutions. The series converges to the exact underlying statistics when $n \to \infty$, but the computation cost will be another factor to consciously choose the number of terms.

The uncorrelated random variables Y_i must also be independent for practical use of the KL method. This is valid only if the random variables and consequently the random field $\xi(\mathbf{x}, \omega)$ are Gaussian. This Gaussian requirement does not restrict the KL method robustness, since the *inverse transform method* provides a means of transforming one probability structure to another; this transformation needs *a prior* known cumulative density function of both distributions. Therefore, the KL Gaussian random field approximation is mapped to an approximation of the originally assumed log-normal distribution. Please refer to [40] for an overview of the use of KL method in modeling rock fracture strength and [41] for further elaboration on the KL and eigen-pair solution procedures, particularly for non-Gaussian fields.

4.4 Numerical Results

We investigate several aspects of the proposed models in fracture modeling of a brittle rock sample. Uniaxial compression tests in homogeneous and inhomogeneous conditions are studied. Figure 4.1 shows the geometry and boundary conditions of the studied problem.

Table 4.1: Material properties for uniaxial sample.

Properties	Units	Values
E	GPa	65
ρ	kg/m^3	2650
τ_c	µs	30
ν	-	0.23
c	MPa	4.7
ϕ	°	17
a	-	10

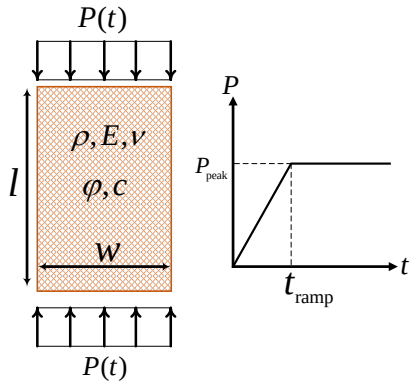

Figure 4.1: Uniaxial compression test and the load history.

This plain strain specimen has the width and length of $w = 0.08$ m and $l = 2w = 0.16$ m, respectively.

Material properties are The rock material properties, listed in Tab. 4.1, are based on rock property groups discussed in [63]. The peak load and ramp time are fixed for all the following simulations which are $P_{\text{peak}} = 13.5$ MPa and $t_{\text{ramp}} = 0.01$ ms, respectively.

The computational domain in spacetime is discretized by simplicial tetrahedral elements, and the corresponding field unknowns, damage and displacement, are approximated by third-order basis functions in spacetime. We define a convergence criterion based on the energy norm of the coupled system, and the tolerance is 10^{-8}.

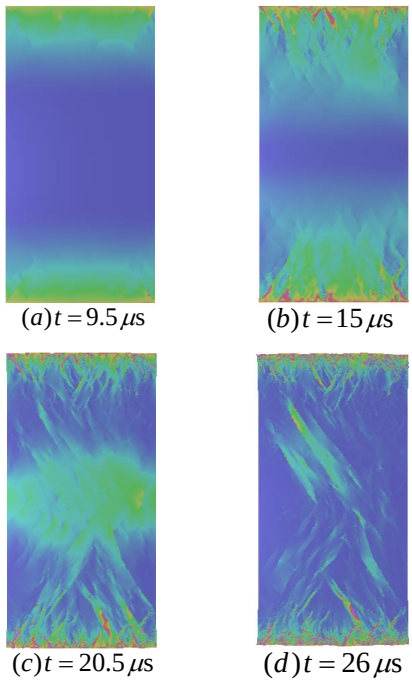

Figure 4.2: Crack distributions at various times in the interfacial model with homogenous properties. The color field shows the strain energy density on the deformed geometry.

Homogeneous material property

In this section, we study failure mechanisms of the proposed bulk and interfacial models under the same boundary conditions and almost the same model parameters as listed in Tab. 4.1. Figures 4.2 and 4.3 show failure patterns for the interfacial and bulk models at different times, respectively. Although the responses are not well matched, the models have some similarities in some aspects. First, the initial damage zones are generated at specimen corners. Second, the fractures or damage zones propagate directionally toward the specimen center. However, there is a significant difference in the estimation of failure zones.

For both models the stress field is relatively uniform along the width of the domain as the wave propagates inward. The strength values are also uniform, due to using a homogeneous material mode. However, as seen in Fig. 4.2 for the interfacial model the fractures are localized rather than populating the entire width of the domain. This is explained by the interfacial nature of this model and small discretization errors; although the stress and strength fields are rather uniform, even small numerical errors cause certain points

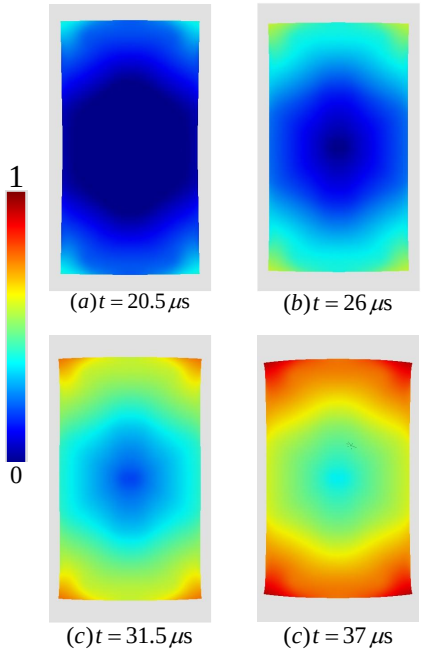

Figure 4.3: Contours of the damage evolution at different times in the non-adaptive bulk model with homogeneous properties. The deformed meshes are depicted by magnification factor of 250. Colors from blue to red correspond to bulk damage values from zero to one, respectively.

to be sites of crack nucleation. Subsequently, the stress field around these nucleation sites becomes highly nonuniform due to the stress concentration and shielded regions surrounding a propagating crack. The cracks are mostly along the angle $45^\circ - \phi/2 \approx 36.6^\circ$ with respect to the load orientation, which matches the predicted angle from the Mohr-Coulomb model [3]. On the other hand, for the bulk damage model fracture is rather uniform along the width of the domain, which does not match the localized failure zones observed experimentally.

This investigation has two outcomes: First, it shows the functionality of the adaptive method in the solution accuracy for tracking crack patterns in the interfacial model; second, it provides evidence of mesh insensitivity of the damage formulation which is a crucial problem in damage mechanics. Figure 4.4 depicts the application of the h-adaptive method in the bulk model. It is obvious there is not any improvement in the approximated failure zones, and the result is in an excellent agreement the result in Fig. 4.3 where the underlying mesh is a nonadaptive 32×64 structured grid of triangles. That is, the rather nonphysical distributed

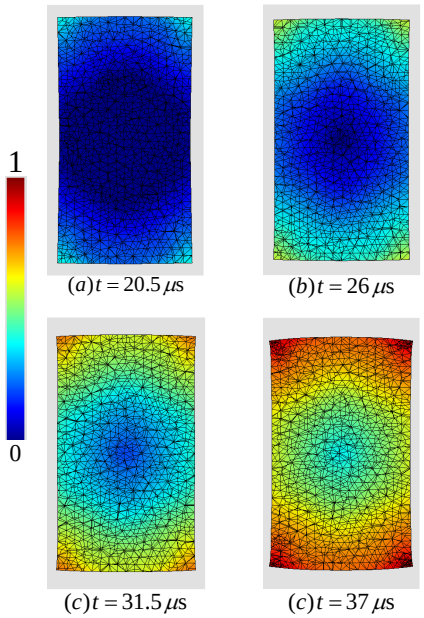

Figure 4.4: Contours of the damage evolution at different times in the adaptive bulk model with homogeneous properties. The deformed meshes are depicted by magnification factor of 250. Colors from blue to red correspond to bulk damage values from zero to one, respectively.

response of the bulk model is intrinsic; from its formulation and unlike the interfacial model, discretization errors and adaptive operations cannot induce localized failure zones.

Inhomogeneous material property

In this section, we show how the consideration of the material randomness results in more realistic responses of the bulk model. We consider random effects of the cohesion value in the bulk model and the tensile strength in the interfacial model. These material properties can significantly affect the failure response of the material as they control the initiation of the degradation process.

Figure 4.5 presents the KL realization of a random field with the correlation length of 5 mm, unitary mean value, and 25% variance for the standard normal form of the fracture strength field. This random distribution is used for the cohesion and fracture strength in the domain with the reported mean values in Tab. 4.1, *i.e.,* 4.7 MPa and 7 MPa, respectively. Other parameters are assumed homogeneous with the same previous values, and the boundary conditions are kept the same as before.

Figures 4.6 and 4.7 show the damage response and fracture propagation at different times for the interfacial and bulk models, respectively. The response of the bulk model indicates that weakest zones in the material have a dominant effect on the evolution of damage. This is concluded by the comparison of the initial damaged zones in Fig. 4.7(a) with weakest zones of the sample in Fig. 4.5. The randomness effect does not have any considerable contribution in the response of the interfacial model. This is due to two sources: First, interfacial models are localized, and so immediately they produce many stress concentration sites in the domain resulting in a localized response even for the homogeneous material strength case shown in Fig. 4.2; second, the compressive loading in the example is too high. Therefore the material does not have enough time to transfer the applied stresses to other places, and many cracks are generated immediately after the imposition of boundary loads. This statement is justifiable by the consideration of an infinite load. In such an extreme case the distribution of material property does not have any effect on the failure response, and the failure always occurs in the same regions. The other factor that may affect the interaction of randomness and the load amplitude is the confinement pressure in bi-axial compression tests which is not studied in this paper. Besides, as the employed damage model is rate-dependent, another crucial topic for further investigations is the interaction of length scales implied by the rate-dependent model and the random field for fracture strength. We leave these questions for future works.

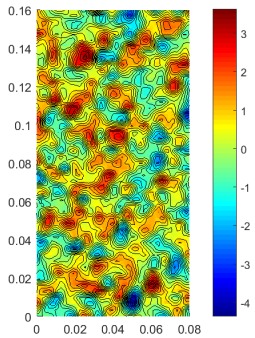

Figure 4.5: A KL realization with unitary mean and 25% variance. The correlation length for the random field is 5 mm.

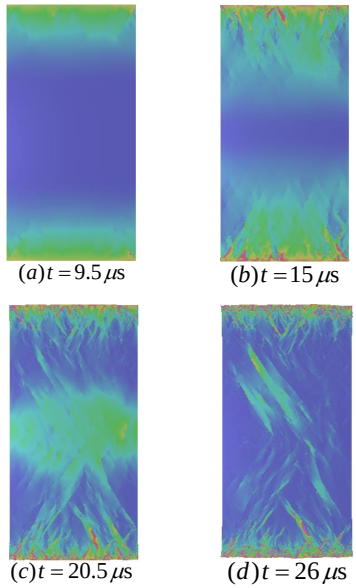

Figure 4.6: Crack distributions at various times in the interfacial model with heterogeneous fracture strength. The color field shows the strain energy density on the deformed geometry.

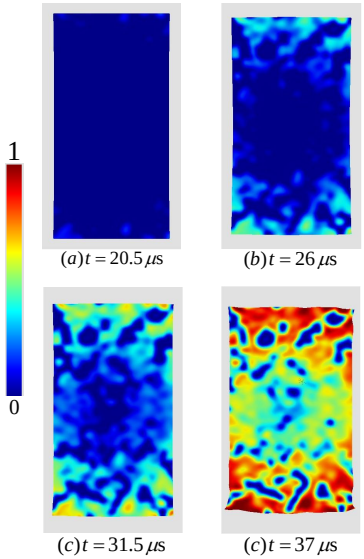

Figure 4.7: Contours of the damage evolution at different times in the bulk model with heterogeneous cohesion. The deformed meshes are depicted by magnification factor of 250. Colors from blue to red correspond to bulk damage values from zero to one, respectively.

The heterogeneity structure of the material cohesion significantly changes the bulk model response to a more realistic behavior. In Fig. 4.7, the damage initiates from the weakest points in the material instead of initiation from corners in Fig. 4.3. The most interesting outcome is the appropriate recovery of the failure zones in the bulk model results. These failure zones are more aligned with the top and bottom boundary edges which are in a good agreement with the interfacial model in Fig. 4.6(d); instead of corners in Fig. 4.3(d). Also, we see more localized behaviors in special directions after the generation of the initial damage spots which considerably modify the globally diffusive behavior in the previous homogeneous example. In compressible tests, these specific inclined failure zones are expected by the Mohr-Coulomb model, and the provided result is comparable with other numerical and experimental observations [112, 113, 76, 49, 100]. This example shows how the randomness improves the reality of the solutions and reduces computational cost with the simpler bulk model.

4.5 Conclusion

In the current study, we formulated a dynamic stochastic damage model for brittle failure. The introduced time-scale parameter in the damage model incorporates rate effects into this model and preserves the mesh objectivity. A statistical framework is formulated based on the KL expansion method to quantify material randomness in the stochastic bulk and interfacial models. We formulated an advanced numerical technology based on the aSDG method to solve the highly nonlinear coupled system of hyperbolic equations. The main advantage of this numerical method is to precisely track wave fronts in highly dynamic impact problems. The final system of nonlinear equations is solved with the Newton-Raphson method.

We showed the most critical factor to get more realistic responses from bulk models is the consideration of randomness effects. Although for this high amplitude loading problem the response of the interfacial model did not change considerably with random fracture strength, the response of the bulk model was significantly affected by a random cohesion field. Therefore, a homogeneous fracture strength field is not an appropriate alternative for

bulk models for certain problems. The mesh objectivity of the proposed damage formulation is proven by a comparison between a fixed-mesh and h-adaptive refined mesh results.

In this work, we assumed an artificial statistics for corresponding random variables in the statistical analysis. In future works, we aim to use statistical volume elements (SVEs) to homogenize random properties of brittle material at different length scales. We will characterize fracture related parameters as random variables with load angle dependence similar to [14].

Chapter 5

Conclusions

In §2, the author presented a time-delay damage formulation for elastodynamics. The weak statement and spacetime discontinuous Galerkin formulation of the damage evolution were presented. Some advantages of this damage formulation are: simplicity of the formulation without requiring any boundary conditions owing to the ODE form of its corresponding evolution equation; hyperbolicity of the coupled elastodynamic-damage equations; indirect introduction of a damage length scale from the multiplication of the model's relaxation time and the longitudinal or shear wave speed implied by the elastodynamic problem; mesh insensitivity without the use of high order spatial derivatives or nonlocal spatial averaging operators owing to the existence of the damage length scale. However, it is noted that this model is mainly applicable to dynamic fracture where wave speeds are relevant.

In §3,the coupled elastodynamic-damage problem was implemented by the aSDG method to solve a uniaxial compressive fracture problem for rock. The MC model is used to formulate a damage force model. In the process of damage accumulation, the effective stress tends from the initial elastic limit at $D = 0$ to its hydrostatic compressive value at $D = 1$. The MC model also captures rock strengthening effect as hydrostatic pressure increases. In contrast, damage models that are based on spectral positive and negative decomposition of strain (or stress) tensor, fail to model failure under compressive response.

To model the effect of material inhomogeneity, cohesion was assumed to be a random field. Two different macroscopic compressive load amplitudes were used for this study. For a homogeneous material, the higher load amplitude initiates damage as the compressive wave

enters the domain, whereas for the lower load damage initiates only in the center of the domain where stress doubling effect occurs upon the intersection of compressive waves. Four lognormal fields with different correlation lengths l_c were generated for $\underline{c}$. It was shown that inhomogeneity could significantly alter the failure response of an otherwise homogeneous rock. For example, for the higher load amplitude, unlike the homogeneous case, damage initiates in the center of the domain. This is due to the particular form of the realized random field where a large zone of low $\underline{c}$ is sampled in the center of the domain. Moreover, for the lower load amplitude damage can initiate everywhere in the domain as the waves travel toward the center of the domain. This is due to the weaker sampled $\underline{c}$ at these locations, which does not require the stress wave doubling effect to initiate damage. Moreover, even the zones that eventually accumulate the highest damage can be significantly different between models with homogeneous and inhomogeneous properties, even as the correlation length tends to zero (low load amplitude example).

Another problem of using a homogeneous material model is the inability or difficulty of bulk damage models to capture sharp localization zones. In contrast, as lower correlation lengths were used for inhomogeneous domains, the fracture pattern became more realistic and resembled the results that are obtained by more accurate sharp interface models [3]. In particular, the MC model predicts fractures at $\pm(45 + \phi/2)$ degree angles with respect to the compressive load direction. For the lowest correlation lengths, localized damage zones with angles roughly in the range ± 45 to $\pm(45 + \phi/2)$ are observed. These features are better resolved with the higher resolution finite element mesh, confirming that finer meshes are required for the solution of problems with more rapid variation of material properties.

In §4, the author showed that the most critical factor to get more realistic responses from bulk models is the consideration of randomness effects. Although for this high amplitude loading problem the response of the interfacial model did not change considerably with random fracture strength, the response of the bulk model was significantly affected by a random cohesion field. Therefore, a homogeneous fracture strength field is not an appropriate alternative for bulk models for certain problems. The mesh objectivity of the proposed damage formulation is proven by a comparison between a fixed-mesh and h-adaptive refined mesh results.

In this work, similar to §3, we assumed an artificial statistics for corresponding random variables in the statistical analysis. In future works, our group aims to use statistical volume elements (SVEs) to homogenize random properties of brittle material at different length scales. We will characterize fracture related parameters as random variables with load angle dependence similar to [14].

Bibliography

[1] Abedi, R., Chung, S.-H., Erickson, J., Fan, Y., Garland, M., Guoy, D., Haber, R., Sullivan, J. M., Thite, S., and Zhou, Y. (2004). Spacetime meshing with adaptive refinement and coarsening. In *Proceedings of the Twentieth Annual Symposium on Computational Geometry*, SCG '04, pages 300–9, Brooklyn, New York, USA. ACM. 26, 58, 61, 80

[2] Abedi, R. and Clarke, P. L. (June 17-20, 2018). Modeling of rock inhomogeneity and anisotropy by explicit and implicit representation of microcracks. In *Proceeding: 52nd US Rock Mechanics/Geomechanics Symposium*, Seattle, Washington, USA. ARMA 18-151-0228-1094. 71

[3] Abedi, R., Haber, R., and Elbanna, A. (2017a). Mixed-mode dynamic crack propagation in rocks with contact-separation mode transitions. In *Proceeding: 51th US Rock Mechanics/Geomechanics Symposium*, San Francisco, California, USA. ARMA 17-0679. 49, 70, 80, 82, 87, 94

[4] Abedi, R. and Haber, R. B. (2014). Riemann solutions and spacetime discontinuous Galerkin method for linear elastodynamic contact. *Computer Methods in Applied Mechanics and Engineering*, 270:150–77. 81

[5] Abedi, R. and Haber, R. B. (2018). Spacetime simulation of dynamic fracture with crack closure and frictional sliding. *Advanced Modeling and Simulation in Engineering Sciences*, 5(1):22. Equal contribution authorship. 20, 21, 47

[6] Abedi, R., Haber, R. B., and Clarke, P. L. (2017b). Effect of random defects on dynamic fracture in quasi-brittle materials. *International Journal of Fracture*, 208(1-2):241–268. xi, 20, 21, 26, 49, 79, 80, 82

[7] Abedi, R., Haber, R. B., and Petracovici, B. (2006a). A spacetime discontinuous Galerkin method for elastodynamics with element-level balance of linear momentum. *Computer Methods in Applied Mechanics and Engineering*, 195:3247–73. 20, 21, 25, 26, 28, 30, 48, 58, 61, 81

[8] Abedi, R., Haber, R. B., Thite, S., and Erickson, J. (2006b). An h–adaptive spacetime–discontinuous Galerkin method for linearized elastodynamics. *Revue Européenne de Mécanique Numérique (European Journal of Computational Mechanics)*, 15(6):619–42. 26, 42, 48, 71

[9] Abedi, R., Hawker, M. A., Haber, R. B., and Matouš, K. (2009). An adaptive spacetime discontinuous Galerkin method for cohesive models of elastodynamic fracture. *International Journal for Numerical Methods in Engineering*, 1:1–42. 25, 30

[10] Abedi, R. and Mudaliar, S. (2017). An asynchronous spacetime discontinuous Galerkin finite element method for time domain electromagnetics. *Journal of Computational Physics*, 351(Supplement C):121–144. 21, 28

[11] Abedi, R., Omidi, O., and Clarke, P. (2016). Numerical simulation of rock dynamic fracturing and failure including microscale material randomness. In *Proceeding: 50th US Rock Mechanics/Geomechanics Symposium*, Houston, Texas, USA. ARMA 16-0531. 49, 80

[12] Abedi, R., Omidi, O., and Clarke, P. (2017c). A numerical study on the effect of loading and randomness on fracture patterns in a tight formation. In *Proceeding: 51th US Rock Mechanics/Geomechanics Symposium*, San Francisco, California, USA. ARMA 17-0641. 80, 82

[13] Abedi, R., Omidi, O., and Enayatpour, S. (2018). A mesh adaptive method for dynamic well stimulation. *Computers and Geotechnics*, 102:12–27. xi, 7, 8, 47

[14] Acton, K. A., Baxter, S. C., Bahmani, B., Clarke, P. L., and Abedi, R. (2018). Voronoi tessellation based statistical volume element characterization for use in fracture modeling. *Computer Methods in Applied Mechanics and Engineering*, 336:135–155. 2, 15, 42, 59, 60, 92, 95

[15] Al-Ostaz, A. and Jasiuk, I. (1997). Crack initiation and propagation in materials with randomly distributed holes. *Engineering Fracture Mechanics*, 58(5-6):395–420. xi, 4, 5, 48, 80

[16] Alfano, G. (2006). On the influence of the shape of the interface law on the application of cohesive-zone models. *Composites Science and Technology*, 66(6):723–730. 47, 79

[17] Allix, O. and Corigliano, A. (1999). Modeling and simulation of crack propagation in mixed-modes interlaminar fracture specimens. *International Journal of Fracture*, 38:111–140. 83

[18] Allix, O. and Deü, J.-F. (1997). Delayed-damage modelling for fracture prediction of laminated composites under dynamic loading. *Engineering transactions*, 45(1):29–46. 19, 21, 31, 32, 48, 52

[19] Allix, O., Feissel, P., and Thevenet, P. (2003). A delay damage mesomodel of laminates under dynamic loading: basic aspects and identification issues. *Computers and Structures*, 81(12):1177–1191. xi, 2, 13, 14, 19, 21, 22, 23, 47, 52, 53, 69, 79, 83

[20] Bahmani, B. and Abedi, R. (2019). Asynchronous spacetime discontinuous galerkin formulation for a hyperbolic time-delay bulk damage model. *Journal of Engineering Mechanics*. 24 pages; Accepted. 2, 15, 48, 49, 59, 63

[21] Bahmani, B., Abedi, R., and Clarke, P. L. (2019a). A stochastic bulk damage model based on mohr-coulomb failure criterion for dynamic rock fracture. *Applied Sciences*, 9(5):830. 15

[22] Bahmani, B., Clarke, P., and Abedi, R. (2018a). Comparison of interfacial and continuum models for dynamic fragmentation analysis. In *ASME 2018 International Mechanical Engineering Congress and Exposition*, pages V009T12A015–V009T12A015. American Society of Mechanical Engineers. 15, 65

[23] Bahmani, B., Clarke, P. L., and Abedi, R. (2018b). A bulk damage model for modeling dynamic fracture in rock. In *Proceeding: 52nd US Rock Mechanics/Geomechanics Symposium*, Seattle, Washington, USA. ARMA 18-151-0228-0826 (10 pages). 20, 39, 83

[24] Bahmani, B., Yang, M., Nagarajan, A., Clarke, P. L., Soghrati, S., and Abedi, R. (2019b). Automated homogenization-based fracture analysis: Effects of SVE size and

boundary condition. *Computer Methods in Applied Mechanics and Engineering*, 345:701–727. 2, 15, 42, 60

[25] Barenblatt, G. I. (1962). The mathematical theory of equilibrium of cracks in brittle fracture. *Advanced Applied Mechanics*, 7:55–129. 47, 79

[26] Bažant, Z. and Novak, D. (2000). Probabilistic nonlocal theory for quasibrittle fracture initiation and size effect- I: Theory. *Journal of Engineering Mechanics*, 126(2):166–174. 49

[27] Bažant, Z. P. and Belytschko, T. B. (1985). Wave propagation in a strain-softening bar: exact solution. *Journal of Engineering Mechanics*, 111(3):381–89. 40, 67

[28] Bažant, Z. P., Belytschko, T. B., and Chang, T.-P. (1984). Continuum theory for strain-softening. *Journal of Engineering Mechanics*, 110(12):1666–92. 31, 67

[29] Bažant, Z. P. and Le, J.-L. (2017). *Probabilistic Mechanics of Quasibrittle Structures: Strength, Lifetime, and Size Effect*. Cambridge University Press. 49

[30] Bažant, Z. P. and Lin, F.-B. (1988). Nonlocal smeared cracking model for concrete fracture. *Journal of Structural Engineering*, 114(11):2493–510. 8, 19, 79

[31] Belytschko, T., Bažant, Z. P., Yul-Woong, H., and Ta-Peng, C. (1986). Strain-softening materials and finite-element solutions. *Computers & Structures*, 23(2):163–80. 31

[32] Belytschko, T. and Black, T. (1999). Elastic crack growth in finite elements with minimal remeshing. *International Journal for Numerical Methods in Engineering*, 45:601–620. 19, 47

[33] Bischoff, P. H. and Perry, S. H. (1995). Impact behavior of plain concrete loaded in uniaxial compression. *Journal of engineering mechanics*, 121(6):685–693. 11, 48

[34] Borden, M. J., Hughes, T. J., Landis, C. M., and Verhoosel, C. V. (2014). A higher-order phase-field model for brittle fracture: Formulation and analysis within the isogeometric analysis framework. *Computer Methods in Applied Mechanics and Engineering*, 273:100–118. 79

[35] Bourdin, B., Francfort, G., and Marigo, J.-J. (2000). Numerical experiments in revisited brittle fracture. *Journal of the Mechanics and Physics of Solids*, 48(4):797 – 826. 79

[36] Brekelmans, W. and De Vree, J. (1995). Reduction of mesh sensitivity in continuum damage mechanics. *Acta Mechanica*, 110(1):49–56. xi, 10

[37] Camacho, G. T. and Ortiz, M. (1996). Computational modelling of impact damage in brittle materials. *International Journal of solids and structures*, 33(20-22):2899–938. 19, 82

[38] Carmeliet, J. and Hens, H. (1994). Probabilistic nonlocal damage model for continua with random field properties. *Journal of Engineering Mechanics*, 120(10):2013–2027. 59

[39] Chiarelli, L., Fumes, F., de Moraes, E. B., Haveroth, G., Boldrini, J. L., and Bittencourt, M. L. (2017). Comparison of high order finite element and discontinuous Galerkin methods for phase field equations: Application to structural damage. *Computers & Mathematics with Applications*, 74(7):1542–64. 20

[40] Clarke, P. and Abedi, R. (2017). Fracture modeling of rocks based on random field generation and simulation of inhomogeneous domains. In *Proceeding: 51th US Rock Mechanics/Geomechanics Symposium*, San Francisco, California, USA. ARMA 17-0643. 61, 84

[41] Clarke, P., Abedi, R., Bahmani, B., Acton, K., and Baxter, S. (2017). Effect of the spatial inhomogeneity of fracture strength on fracture pattern for quasi-brittle materials. In *Proceedings of ASME 2017 International Mechanical Engineering Congress & Exposition IMECE 2017*, page V009T12A045 (9 pages), Tampa, Florida, USA. IMECE2017-71515. 42, 49, 80, 84

[42] Comi, C. (1999). Computational modelling of gradient-enhanced damage in quasi-brittle materials. *Mechanics of Cohesive-frictional Materials: An International Journal on Experiments, Modelling and Computation of Materials and Structures*, 4(1):17–36. 19, 48, 58

[43] Corigliano, A. and Ricci, M. (1999). Rate-dependent interface models: formulation and numerical applications. *International Journal of Solids and Structures*, 38:547–576. 83

[44] Daphalapurkar, N., Ramesh, K., Graham-Brady, L., and Molinari, J. (2011). Predicting variability in the dynamic failure strength of brittle materials considering pre-existing flaws. *Journal of the Mechanics and Physics of Solids*, 59(2):297–319. 59

[45] Daux, C., Moës, N., Dolbow, J., Sukumar, N., and Belytschko, T. (2000). Arbitrary branched and intersecting cracks with the extended finite element method. *International journal for numerical methods in engineering*, 48(12):1741–60. 19

[46] de Borst, R. and Verhoosel, C. V. (2016). Gradient damage vs phase-field approaches for fracture: Similarities and differences. *Computer Methods in Applied Mechanics and Engineering*, 312:78–94. 48

[47] De Vree, J., Brekelmans, W., and Van Gils, M. (1995). Comparison of nonlocal approaches in continuum damage mechanics. *Computers and Structures*, 55:581–88. 19

[48] Dimas, L., Giesa, T., and Buehler, M. (2014). Coupled continuum and discrete analysis of random heterogeneous materials: Elasticity and fracture. *Journal of the Mechanics and Physics of Solids*, 63(1):481–490. 59, 60

[49] Dinç, Ö. and Scholtès, L. (2017). Discrete analysis of damage and shear banding in argillaceous rocks. *Rock Mechanics and Rock Engineering*, pages 1–18. 68, 91

[50] Duarte, C. A., Babuška, I., and Oden, J. T. (2000). Generalized finite element methods for three-dimensional structural mechanics problems. *Computers & Structures*, 77(2):215–232. 19, 47

[51] Dugdale, D. S. (1960). Yielding of steel sheets containing slits. *Journal of the Mechanics and Physics of Solids*, 8:100–104. 47, 79

[52] Fleming, W. H. (1964). *Functions of Several Variables*. Addison-Wesley, Reading, Massachusetts. 28

[53] Francfort, G. and Marigo, J.-J. (1998). Revisiting brittle fracture as an energy minimization problem. *Journal of the Mechanics and Physics of Solids*, 46(8):1319 – 1342. 79

[54] Genet, M., Couegnat, G., Tomsia, A., and Ritchie, R. (2014). Scaling strength distributions in quasi-brittle materials from micro- to macro-scales: A computational approach to modeling nature-inspired structural ceramics. *Journal of the Mechanics and Physics of Solids*, 68(1):93–106. 80

[55] Ghanem, R. and Spanos, P. (1991). *Stochastic finite elements: a spectral approach*. Springer-Verlag. 60, 84

[56] Gitman, I., Askes, H., and Sluys, L. (2008). Coupled-volume multi-scale modelling of quasi-brittle material. *European Journal of Mechanics-A/Solids*, 27(3):302–327. 12

[57] Ha, Y. D. and Bobaru, F. (2010). Studies of dynamic crack propagation and crack branching with peridynamics. *International Journal of Fracture*, 162(1-2):229–244. 10, 47

[58] Hamdi, E., Romdhane, N. B., and Le Cléach, J.-M. (2011). A tensile damage model for rocks: application to blast induced damage assessment. *Computers and Geotechnics*, 38(2):133–41. 30

[59] Häussler-Combe, U. and Kühn, T. (2012). Modeling of strain rate effects for concrete with viscoelasticity and retarded damage. *International Journal of Impact Engineering*, 50:17–28. xi, 13, 14, 15, 20, 42, 63

[60] Häussler-Combe, U. and Panteki, E. (2016). Modeling of concrete spallation with damaged viscoelasticity and retarded damage. *International Journal of Solids and Structures*, 90:153–66. 19, 42, 48

[61] Hesthaven, J. S. and Warburton, T. (2007). *Nodal discontinuous Galerkin methods: algorithms, analysis, and applications*. Springer Science & Business Media. 20

[62] Hoek, E. (1983). Strength of jointed rock masses. *Geotechnique*, 33(3):187–223. 71

[63] Hoek, E. (2000). Practical rock engineering. 85

[64] Hoek, E. and Brown, T. (1980). *Underground Excavations in Rock*. Geotechnics and foundations. Taylor & Francis. 50

[65] Jirásek, M. (2004). Nonlocal theories in continuum mechanics. *Acta Polytechnica*, 44(5-6). 19

[66] Jirásek, M. and Patzák, B. (2002). Consistent tangent stiffness for nonlocal damage models. *Computers & structures*, 80(14-15):1279–1293. 22, 55

[67] Junker, P., Schwarz, S., Makowski, J., and Hackl, K. (2017). A relaxation-based approach to damage modeling. *Continuum Mechanics and Thermodynamics*, 29(1):291–310. 19, 48

[68] Kamensky, D., Moutsanidis, G., and Bazilevs, Y. (2018). Hyperbolic phase field modeling of brittle fracture: Part I–theory and simulations. *Journal of the Mechanics and Physics of Solids*, 121:81–98. 14, 42

[69] Karhunen, K. and Selin, I. (1960). *On linear methods in probability theory*. Rand Corporation. 60, 80

[70] Khoei, A., Vahab, M., and Hirmand, M. (2018). An enriched–FEM technique for numerical simulation of interacting discontinuities in naturally fractured porous media. *Computer Methods in Applied Mechanics and Engineering*, 331:197–231. 47

[71] Klinsmann, M., Rosato, D., Kamlah, M., and McMeeking, R. M. (2015). An assessment of the phase field formulation for crack growth. *Computer Methods in Applied Mechanics and Engineering*, 294:313–330. 79

[72] Kozicki, J. and Tejchman, J. (2007). Effect of aggregate structure on fracture process in concrete using 2D lattice model. *Archives of Mechanics*, 59(4-5):365–84. xi, 5, 48, 80

[73] Lasry, D. and Belytschko, T. (1988). Localization limiters in transient problems. *International Journal of Solids and Structures*, 24(6):581–97. 19, 48, 83

[74] Lee, Y.-K. and Pietruszczak, S. (2017). Analytical representation of mohr failure envelope approximating the generalized Hoek-Brown failure criterion. *International Journal of Rock Mechanics and Mining Sciences*, 100:90–99. 71

[75] Levy, S. and Molinari, J. (2010). Dynamic fragmentation of ceramics, signature of defects and scaling of fragment sizes. *Journal of the Mechanics and Physics of Solids*, 58(1):12–26. 59

[76] Li, G. and Tang, C.-A. (2015). A statistical meso-damage mechanical method for modeling trans-scale progressive failure process of rock. *International Journal of Rock Mechanics and Mining Sciences*, 74:133–150. 68, 91

[77] Loéve, M. (1977). *Probability theory*. Springer, New York. 60, 80

[78] Londono, J. G., Berger-Vergiat, L., and Waisman, H. (2017). An equivalent stress-gradient regularization model for coupled damage-viscoelasticity. *Computer Methods in Applied Mechanics and Engineering*, 322:137–66. 24, 58

[79] Loret, B. and Prevost, J. H. (1990). Dynamic strain localization in elasto-(visco-) plastic solids, part 1. general formulation and one-dimensional examples. *Computer Methods in Applied Mechanics and Engineering*, 83(3):247–73. 19, 48

[80] Lyakhovsky, V., Hamiel, Y., and Ben-Zion, Y. (2011). A non-local visco-elastic damage model and dynamic fracturing. *Journal of the Mechanics and Physics of Solids*, 59(9):1752–1776. 19, 48

[81] Mandal, T. K., Nguyen, V. P., and Heidarpour, A. (2019). Phase field and gradient enhanced damage models for quasi-brittle failure: A numerical comparative study. *Engineering Fracture Mechanics*, 207:48–67. 48

[82] Mazars, J. (1984). Application de la mécanique de l'endommagement au comportement non linéaire et à la rupture du béton de structure. *THESE DE DOCTEUR ES SCIENCES PRESENTEE A L'UNIVERSITE PIERRE ET MARIE CURIE-PARIS 6*. 22, 55

[83] Miehe, C., Hofacker, M., and Welschinger, F. (2010a). A phase field model for rate-independent crack propagation: Robust algorithmic implementation based on operator splits. *Computer Methods in Applied Mechanics and Engineering*, 199(45-48):2765–78. 19

[84] Miehe, C., Welschinger, F., and Hofacker, M. (2010b). Thermodynamically consistent phase-field models of fracture: Variational principles and multi-field fe implementations. *International Journal for Numerical Methods in Engineering*, 83(10):1273–1311. xi, 9, 11, 79

[85] Moës, N., Dolbow, J., and Belytschko, T. (1999). A finite element method for crack growth without remeshing. *International journal for numerical methods in engineering*, 46(1):131–50. 19, 47

[86] Molnár, G. and Gravouil, A. (2017). 2d and 3d abaqus implementation of a robust staggered phase-field solution for modeling brittle fracture. *Finite Elements in Analysis and Design*, 130:27–38. 13

[87] Moreau, K., Moës, N., Picart, D., and Stainier, L. (2015). Explicit dynamics with a non-local damage model using the thick level set approach. *International Journal for Numerical Methods in Engineering*, 102(3-4):808–38. 22, 55

[88] Murakami, S. (2012). *Continuum damage mechanics: a continuum mechanics approach to the analysis of damage and fracture*. Springer Science & Business Media. 24, 54

[89] Nguyen, V. P. (2014). Discontinuous galerkin/extrinsic cohesive zone modeling: Implementation caveats and applications in computational fracture mechanics. *Engineering Fracture Mechanics*, 128:37–68. 47, 79

[90] Parrinello, F., Failla, B., and Borino, G. (2009). Cohesive-frictional interface constitutive model. *International Journal of Solids and Structures*, 46(13):2680 – 2692. 47, 79

[91] Peerlings, R., De Borst, R., Brekelmans, W., and De Vree, J. (1996). Gradient enhanced damage for quasi-brittle materials. *International Journal for Numerical Methods in Engineering*, 39(19):3391–403. 83

[92] Peerlings, R., De Borst, R., Brekelmans, W., and Geers, M. (1998). Gradient-enhanced damage modelling of concrete fracture. *Mechanics of Cohesive-frictional Materials*, 3(4):323–42. 19, 22, 24, 48, 54, 55, 58

[93] Peerlings, R., De Borst, R., Brekelmans, W., and Geers, M. (2002). Localisation issues in local and nonlocal continuum approaches to fracture. *European Journal of Mechanics, A/Solids*, 21(2):175–89. 83

[94] Peerlings, R., Geers, M., De Borst, R., and Brekelmans, W. (2001). A critical comparison of nonlocal and gradient-enhanced softening continua. *International Journal of solids and Structures*, 38(44-45):7723–46. 19, 31, 48

[95] Pereira, L., Weerheijm, J., and Sluys, L. (2017). A new effective rate dependent damage model for dynamic tensile failure of concrete. *Engineering Fracture Mechanics*, 176:281–99. xi, 11, 12, 19, 48

[96] Pietruszczak, S. and Mroz, Z. (2001). On failure criteria for anisotropic cohesive-frictional materials. *International Journal for Numerical and Analytical Methods in Geomechanics*, 25(5):509–524. 71

[97] Pijaudier-Cabot, G. and Bažant, Z. P. (1987). Nonlocal damage theory. *Journal of engineering mechanics*, 113(10):1512–1533. 83

[98] Rabczuk, T. and Ren, H. (2017). A peridynamics formulation for quasi-static fracture and contact in rock. *Engineering Geology*, 225:42–48. 10, 47

[99] Rangarajan, R. and Lew, A. J. (2014). Universal meshes: A method for triangulating planar curved domains immersed in nonconforming meshes. *International Journal for Numerical Methods in Engineering*, 98(4):236–264. 47

[100] Rangari, S., Murali, K., and Deb, A. (2018). Effect of meso-structure on strength and size effect in concrete under compression. *Engineering Fracture Mechanics*. 68, 91

[101] Ren, X., Chen, J.-S., Li, J., Slawson, T., and Roth, M. (2011). Micro-cracks informed damage models for brittle solids. *International journal of solids and structures*, 48(10):1560–1571. 23

[102] Rinaldi, A., Krajcinovic, D., and Mastilovic, S. (2007). Statistical damage mechanics and extreme value theory. *Int. J. Damage Mech. (USA)*, 16(1):57 – 76. 49, 80

[103] Rossi, P. (1991). A physical phenomenon which can explain the mechanical behaviour of concrete under high strain rates. *Materials and Structures*, 24(6):422–424. 11

[104] Schicker, J. and Pfuff, M. (2006). Statistical modelling of fracture in quasi-brittle materials. *Advanced Engineering Materials*, 8(5):406–410. 59

[105] Silling, S. A. and Lehoucq, R. (2010). Peridynamic theory of solid mechanics. In *Advances in applied mechanics*, volume 44, pages 73–168. Elsevier. 10, 47

[106] Sluys, L., De Borst, R., and Mühlhaus, H.-B. (1993). Wave propagation, localization and dispersion in a gradient-dependent medium. *International Journal of Solids and Structures*, 30(9):1153–71. 19, 31

[107] Spivak, M. (1965). *Calculus on Manifolds*. W. A. Benjamin, New York. 28

[108] Spring, D. W., Leon, S. E., and Paulino, G. H. (2014). Unstructured polygonal meshes with adaptive refinement for the numerical simulation of dynamic cohesive fracture. *International Journal of Fracture*, 189(1):33–57. 47

[109] Strouboulis, T., Babuška, I., and Copps, K. (2000). The design and analysis of the generalized finite element method. *Computer Methods in Applied Mechanics and Engineering*, 181:43–69. 19, 47

[110] Stumpf, H. and Hackl, K. (2003). Micromechanical concept for the analysis of damage evolution in thermo-viscoelastic and quasi-brittle materials. *International Journal of Solids and Structures*, 40(6):1567–84. 42

[111] Suffis, A., Lubrecht, T. A., and Combescure, A. (2003). Damage model with delay effect: Analytical and numerical studies of the evolution of the characteristic damage length. *International Journal of Solids and Structures*, 40(13-14):3463–76. 19, 23, 31, 53

[112] Tang, C., Tham, L., Lee, P., Tsui, Y., and Liu, H. (2000). Numerical studies of the influence of microstructure on rock failure in uniaxial compression - part II: constraint,

slenderness, and size effect. *International Journal of Rock Mechanics and Mining Sciences*, 37(4):571–583. 68, 91

[113] Teng, J., Zhu, W., and Tang, C. (2004). Mesomechanical model for concrete. part II: applications. *Magazine of Concrete Research*, 56(6):331–345. 68, 91

[114] Thai, T. Q., Rabczuk, T., Bazilevs, Y., and Meschke, G. (2016). A higher-order stress-based gradient-enhanced damage model based on isogeometric analysis. *Computer Methods in Applied Mechanics and Engineering*, 304:584–604. 13, 83

[115] Truster, T. J. and Masud, A. (2013). A discontinuous/continuous Galerkin method for modeling of interphase damage in fibrous composite systems. *Computational Mechanics*, 52(3):499–514. 20

[116] Vignjevic, R., Djordjevic, N., De Vuyst, T., and Gemkow, S. (2018). Modelling of strain softening materials based on equivalent damage force. *Computer Methods in Applied Mechanics and Engineering*, 335:52–68. 31

[117] Wang, Z.-l., Li, Y.-c., and Wang, J. (2007). A damage-softening statistical constitutive model considering rock residual strength. *Computers & Geosciences*, 33(1):1–9. 30

[118] Weibull, W. (1939). A statistical theory of the strength of materials. *R. Swed. Inst. Eng. Res.*, page Res. 151. 49, 80

[119] Weibull, W. (1951). A statistical distribution function of wide applicability. *Journal of Applied Mechanics*, 18:293–297. 49, 80

[120] Wells, G. N., Garikipati, K., and Molari, L. (2004). A discontinuous Galerkin formulation for a strain gradient-dependent damage model. *Computer Methods in Applied Mechanics and Engineering*, 193(33-35):3633–45. 20

[121] Xu, T., Yang, S., Chen, C., Yang, T., Zhang, P., and Liu, H. (2017). Numerical investigation of damage evolution and localized fracturing of brittle rock in compression. *Journal of Performance of Constructed Facilities*, 31(5):04017065. 67

[122] Zhao, H., Zhang, C., Cao, W.-g., and Zhao, M.-h. (2016). Statistical meso-damage model for quasi-brittle rocks to account for damage tolerance principle. *Environmental Earth Sciences*, 75(10):862. 30

[123] Zhou, F. and Molinari, J. (2004). Stochastic fracture of ceramics under dynamic tensile loading. *International Journal of Solids and Structures*, 41(22-23):6573–6596. 59

Appendix

A List of Publications

I am the author of following papers as a Research Assistant under supervision of Dr. Reza Abedi. The content of the present thesis, except the introduction chapter, is previously published in some of these papers:

1. **B. Bahmani**, R. Abedi, "Asynchronous Spacetime Discontinuous Galerkin formulation for a hyperbolic time-delay bulk damage model", *Journal of Engineering Mechanics*, **Accepted**.

2. **B. Bahmani**, R. Abedi, P.L. Clarke, "A stochastic bulk damage model based on Mohr-Coulomb failure criterion for dynamic rock fracture", *Applied Sciences*, 9(5):830, 2019.

3. **B. Bahmani**, M. Yang, A. Nagarajan, S. Soghrati, R. Abedi, "Automated homogenization-based fracture analysis: effects of SVE size and boundary condition", *Computer Methods in Applied Mechanics and Engineering*, 345, 701-727, 2019.

4. K.A. Acton, S.C Baxter, **B. Bahmani**, P.L. Clarke, R. Abedi, "Voronoi tessellation based Statistical Volume Element characterization for use in fracture modeling", *Computer Methods in Applied Mechanics and Engineering*, 336, 135-155, 2018.

5. K.A. Acton, C. Sherod, **B. Bahmani**, R. Abedi, "Mesoscale Material Strength Characterization for Use in Fracture Modeling", *ASCE-ASME Journal of Risk and Uncertainty in Engineering Systems Part B: Mechanical Engineering*, **Submitted**.

6. **B. Bahmani**, R. Abedi, P.L. Clarke, "A bulk damage model for modeling dynamic fracture in rock", *Proceeding* 52^{th} *U.S. Rock Mechanics/Geomechanics Symposium* (ARMA), Seattle, WA (2018).

7. **B. Bahmani**, R. Abedi, P.L. Clarke, "Comparison of interfacial and continuum models for dynamic fragmentation analysis", *ASME 2018 International Mechanical Engineering Congress and Exposition* (IMECE), Pittsburgh, PA (2018).

8. **B. Bahmani**, M. Yang, A. Nagarajan, P.L. Clarke, S. Soghrati, R. Abedi, "An integrated approach microscale homogenization to macroscopic dynamic fracture analysis", *ASME 2018 International Mechanical Engineering Congress and Exposition* (IMECE), Pittsburgh, PA (2018).

9. K.A. Acton, **B. Bahmani**, R. Abedi, "Mesoscale material strength characterization for use in fracture modeling", *ASME 2018 International Mechanical Engineering Congress and Exposition* (IMECE), Pittsburgh, PA (2018).

10. P.L. Clarke, R. Abedi, **B. Bahmani**, K.A. Acton, S.C. Baxter, "Effect of the spatial inhomogeneity of fracture strength on fracture pattern for quasi-brittle materials", *ASME 2017 International Mechanical Engineering Congress and Exposition* (IMECE), Tampa, FL (2017).

11. K.A. Acton, S.C. Baxter, **B. Bahmani**, P.L. Clarke, R. Abedi, "Mesoscale models characterizing material property fields used as a basis for predicting fracture patterns in quasi-brittle materials", *ASME 2017 International Mechanical Engineering Congress and Exposition* (IMECE), Tampa, FL (2017).

Vita

Before joining Dr. Abedi's group in Feb. 2017, Bahador held an MS degree in Structural Mechanics with the focus on computational mechanics at Sharif University of Technology, Tehran, Iran under supervision of Prof. A.R. Khoei in Jan. 2016. His thesis title was "Numerical Modeling of Heat Transfer and Thermo-Mechanical Contact in Fractured Medium Using eXtended Finite Element Method (X-FEM)." As a Research Assistant in Prof. Khoei's group, Bahador developed a novel interface formulation based on the X-FEM for modeling nonlinear-multiphysics mechanisms at fracture surface. He showed its application for thermo-mechanical contact problems and non-iso thermal fluid injection inside hydraulically driven fractures. Bahador also developed a novel staggered framework for solving a local hyperbolic transport equation coupled with a global parabolic transport. This framework integrates Bubnov-Galerkin X-FEM with Least Square Finite Element Method (LSFEM) for parabolic and hyperbolic solvers, respectively.